Neuronal and Hemodynamic Functional Connectivity in the Awake Mouse

David Thibodeaux

Submitted in partial fulfillment of the
requirements for the degree of
Doctor of Philosophy
under the Executive Committee
of the Graduate School of Arts and Sciences

COLUMBIA UNIVERSITY

2023

Dedication

This dissertation is dedicated to my wife Naomi, and my daughter Alexandria.

Abstract

Neuronal and Hemodynamic Functional Connectivity in the Awake Mouse

David Thibodeaux

Resting State functional Magnetic Resonance Imaging (rs-fMRI) has revealed brain-wide correlation patterns throughout the human brain, interpreted as Functional Connectivity. Dynamic Functional Connectivity (DFC) has recently expanded on this technique via sliding window correlation analysis, revealing moment-to-moment changes in functional connectivity across an imaging session. However, the meaning of these transitions in terms of neural activity and behavior are not well understood.

In this work, I utilized Dynamic Functional Connectivity analytical techniques in conjunction with Wide Field Optical Mapping (WFOM) in the awake, freely behaving mouse. I hypothesized that neural and hemodynamic activity observed with WFOM would exhibit similar transitions between functional connectivity states as reported by fMRI DFC studies. I also explored whether changes in functional connectivity would correspond to changes in behavior.

Simultaneous neural and hemodynamic activity was collected using WFOM from five freely behaving head-fixed Thy1-jRGECO1a mice. Behavioral metrics of movement, whisking and pupillometry were acquired simultaneously. Raw neuroimaging data were dimensionally reduced to representative time courses across the dorsal surface of the cortex for each subject utilizing a semi-supervised clustering technique. Functional Connectivity analysis revealed rich spatiotemporal structures within neural and hemodynamic activity, which were consistent across imaging sessions and subjects.

I observed broad changes in Functional Connectivity metrics during rest, locomotion, and transitional epochs between the two by directly comparing windows captured during these

epochs. It was also observed that Functional Connectivity metrics immediately following locomotion offset could be distinguished from periods of sustained rest. Similar to human fMRI studies, a distinct increase in bilateral connectivity of anterior lateral prefrontal cortex was observed, which became significantly less synchronized with posterior brain regions during sustained periods of rest.

I next used an unsupervised clustering technique on the same data to test if these properties could be observed in an indirect manner. This approach has been previously used in numerous human fMRI studies, and contextualized this work to human fMRI studies. A sliding window was used to calculate moment-to-moment Functional Connectivity maps across each imaging session. These dynamic correlation maps were clustered into multiple states, which could then be used to calculate the most representative state for any given epoch. Unsupervised clustering revealed strikingly similar dynamic states to our previous observations. These dynamic states also exhibited independent distributions of behavioral activity both in neural and hemodynamic models, leading us to conclude that there is not only a meaningful link between Functional Connectivity in neural and hemodynamic activity, but that behavioral shifts largely drive these changes.

My findings provide strong evidence that Dynamic Functional Connectivity has neural origins, and hemodynamic responses are able to depict correlation patterns that tracks rapid changes in behavior and internal brain states such as the level of arousal or alertness. Future studies are necessary to further investigate this speculation, but this offers an excellent framework to better understand the rich, dynamic properties of brain activity.

Table of Contents

List of Figures

Acknowledgments

I'd like to thank the many colleagues and collaborators who have worked alongside me for these many years for providing invaluable knowledge, advice and great memories. I'd also like to thank my thesis committee – Dr. Elizabeth Hillman, Dr. Joshua Jacobs, Dr. Tian Zheng, Dr. Elizabeth Olson, and Dr. Charles Schroeder for taking the time to listen, read, and provide meaningful feedback and critique.

I'm grateful to Dr. Somayeh Shahsavarani and Fatema Lodgher for significant contributions and support to the underlying work related to this thesis, especially in the later analytical stages. The mentorship and expertise of Dr. Mohammad Shaik and Dr. Joszef Meszaros were also incredibly valuable in my earlier graduate school years, and made me a better scientist and researcher.

Finally, I'd like to thank my family and friends who have been a continual support system during these years. I'd like to especially thank my wife Naomi, my mother Lesa, and my Father and Mother-in-law Frank and Leslee Jacobs.

Dissertation Committee

Elizabeth M.C. Hillman, PhD

Professor of Biomedical Engineering and Radiology

Columbia University

Elizabeth Olson, PhD

Professor of Biomedical Engineering and Auditory Biophysics

Columbia University

Joshua Jacobs, PhD

Assistant Professor of Biomedical Engineering

Columbia University

Tian Zheng, PhD

Professor of Statistics

Columbia University

Charles Schroeder, PhD

Professor of Neuroscience and Neurology

Columbia University

1 Chapter 1: Introduction

Functional Magnetic Resonance Imaging (fMRI), a commonly utilized neuroimaging modality in both clinical and research settings, measures changes in deoxygenated hemoglobin to infer fluctuations in brain activity. Recent advancements in fMRI analysis techniques have revealed dynamic changes in the functional structure of resting state fMRI measurements. This phenomenon, referred to as Dynamic Functional Connectivity (DFC), is still a topic of great interest with many open questions. In this thesis, I aimed to expand our knowledge of Dynamic Functional Connectivity using simultaneous measurements of neural activity and blood flow in the awake, behaving mouse.

Chapter 1 provides an overview of the history of neuroimaging, particularly focusing on resting state fMRI, Functional Connectivity, and Intrinsic Signal Imaging. I highlight the current findings, approaches and challenges, which motivate the body of my work.

Chapter 2 details the design and use of Wide Field Optical Mapping (WFOM) for the simultaneous investigation of neural and hemodynamic activity in small animals. I summarize the key components of the optical and behavioral apparatus design, as well as the methods developed to analyze and interpret both neurological and behavioral metrics.

Chapter 3 presents the methodologies I developed to decompose and visualize raw neuroimaging datasets collected using WFOM. These techniques were initially used in the context of exploratory data analysis, and evolved over time into a rigorous methodology that can be used to analyze the functional connectivity changes across imaging sessions and subjects.

Chapter 4 summarizes key findings when evaluating Functional Connectivity in the context of movement and rest. I first show that movement and rest are characterized by strong dynamic fluctuations, which can be clearly delineated by using both direct comparison and

clustering methodologies used in Dynamic Functional Connectivity analysis. Next, I summarize key findings of five behavioral states that were then identified, and show that certain brain regions systematically alter their Functional Connectivity measures in these states, which agrees with previous studies of Functional Connectivity.

In **Chapter 5**, I evaluate Dynamic Functional Connectivity from the perspective of fMRI analytical methods. Using a technique popularized in human fMRI experiments, I cluster neuronal and hemodynamic activity into 5 distinct states, and show that Functional Connectivity in both measures are inherently linked to spontaneous changes in behavior. I then show that not only do these states exhibit distinct behavioral dynamics, but that the observations made in the previous chapter are consistent with these findings.

1.1 Functional Connectivity in the Human Brain

Functional Connectivity represents a measurement of the degree that physically separate brain regions share similarities in their activity over time. Functional Connectivity can be measured using a variety of techniques, but the most common approach uses the Pearson's correlation coefficient to infer the degree of functional connectivity between two brain regions. Here, x and y represent two independent time courses, and *r* represents the correlation coefficient:

$$r = \frac{\sum_{i=1}^{n}(x_i - \bar{x})(y_i - \bar{y})}{\sqrt{\sum_{i=1}^{n}(x_i - \bar{x})^2}\sqrt{\sum_{i=1}^{n}(y_i - \bar{y})^2}} \quad (1.1)$$

Early applications of Functional Connectivity measures were used to implicate Functional Connectivity during rest, and were first observed in 1995 by Bharat Biswal. By measuring changes in the Blood Oxygenation Level Dependent (BOLD) signal, Biswal and colleagues extracted timecourses from human fMRI imaging sequences, and observed correlative structures in the timeseries during periods of rest that overlapped with response regions from a finger tapping task (Figure 1) (Biswal et al., 1995). Until then, correlation patterns in resting state BOLD timecourses were considered to be largely unstructured and insignificant as an area of study.

This discovery was the cornerstone of the field of Resting State Functional Connectivity (Heuvel and Pol, 2010). The concept of functional connectivity contrasted against the study of structural connectivity, the traditional interpretation of brain structure and function at the time. Structural and functional connectivity are now studied as two separate but valid interpretations of

brain architecture (Uddin, 2013), and while they share broad similarities, many studies have found notable divergences between the regions involved in each (Fukushima et al., 2018).

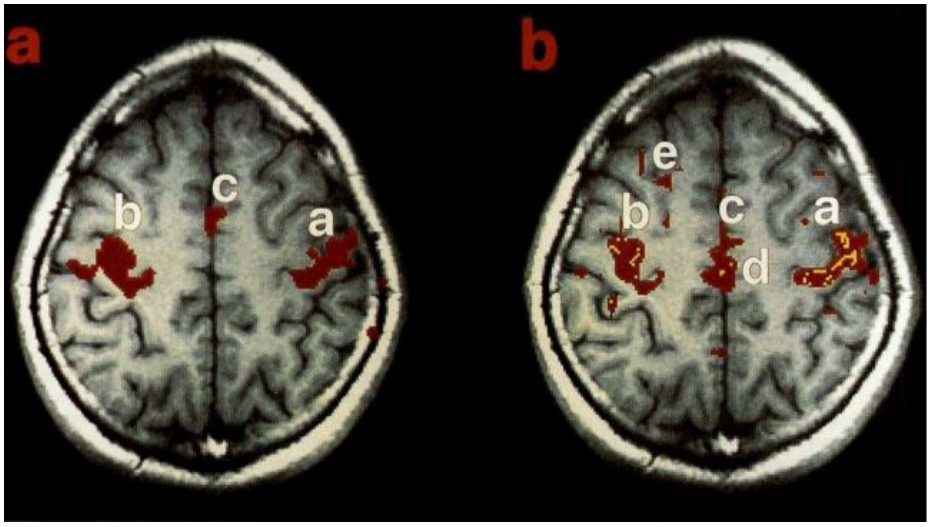

Figure 1 – (a) fMRI task-activation response to bilateral left and right finger movement, superimposed on a GRASS anatomic image. (b) Resting state activity. Red is positive correlation, and yellow is negative. Adapted from (Biswal et al., 1995).

Resting State Functional Connectivity measurements are traditionally collected in human studies using fMRI and/or Electroencephalography (EEG), but advancements in both MRI technology and other imaging techniques have expanded the field beyond the original BOLD signal acquisition and correlation analysis. Since then, similar connectivity patterns have been observed across a variety of animal models and experimental contexts (Hsu et al., 2016; Stafford et al., 2014). This has led to a massive expansion in the field of Resting State Functional Connectivity, as researchers study it in a multitude of species, experimental and clinical contexts.

1.1.1 Critiques of Resting State Functional Connectivity measurements

While Resting State Functional Connectivity can be a powerful noninvasive neuroimaging tool, it is not without concerns. Interpretation of Resting State Functional Connectivity measurements is complicated by subject variability, physiological artifacts such as head motion and breathing, and replication of results. While many tools have been developed to

combat all of these concerns, they come with their own drawbacks. One particular example of this is the use of Global Signal Regression (GSR) for the removal of widespread correlations across the brain, which are typically assumed to be a nuisance signal. While this approach does remove these global correlations effectively, it has been shown to negatively bias correlation signals (Saad et al., 2012), skewing those same results which were intended to be free of global artifacts. (Beckmann et al., 2005; Buckner et al., 2013). At the same time, some have argued that these supposed "nuisance signals" carry some valuable information (Liu et al., 2017), and so the use of GSR may be hurting more than helping in our pursuit to better understand Resting State Functional Connectivity.

1.1.2 The network architecture of brain activity

A decade after the discovery of RSFC, Mark Raichle and colleagues found that certain brain regions modulated their activity levels during tasks. While some regions increased activity during task performance, others decreased. These task-negative regions also showed increased connectivity during rest, leading these researchers to name them what is commonly known as the Default Mode Network (Fox et al., 2005). In humans, the Default Mode Network has been described as a functionally connected brain network that integrates spatially and functionally vast regions, and is shown to be active during self-reference, memory recall, episodic memory and future planning (Andrews-Hanna, 2012, p.). The Default Mode Network has also been implicated in other animal models (Hsu et al., 2016; Stafford et al., 2014), implying that the Default Mode Network has foundations in the neural architecture of the brain, and is not simply relegated to human anatomy. Since then, many other brain networks have been observed in various contexts (Raichle, 2015). Some examples of these networks include the language, visual, and sensorimotor networks (Figure 2).

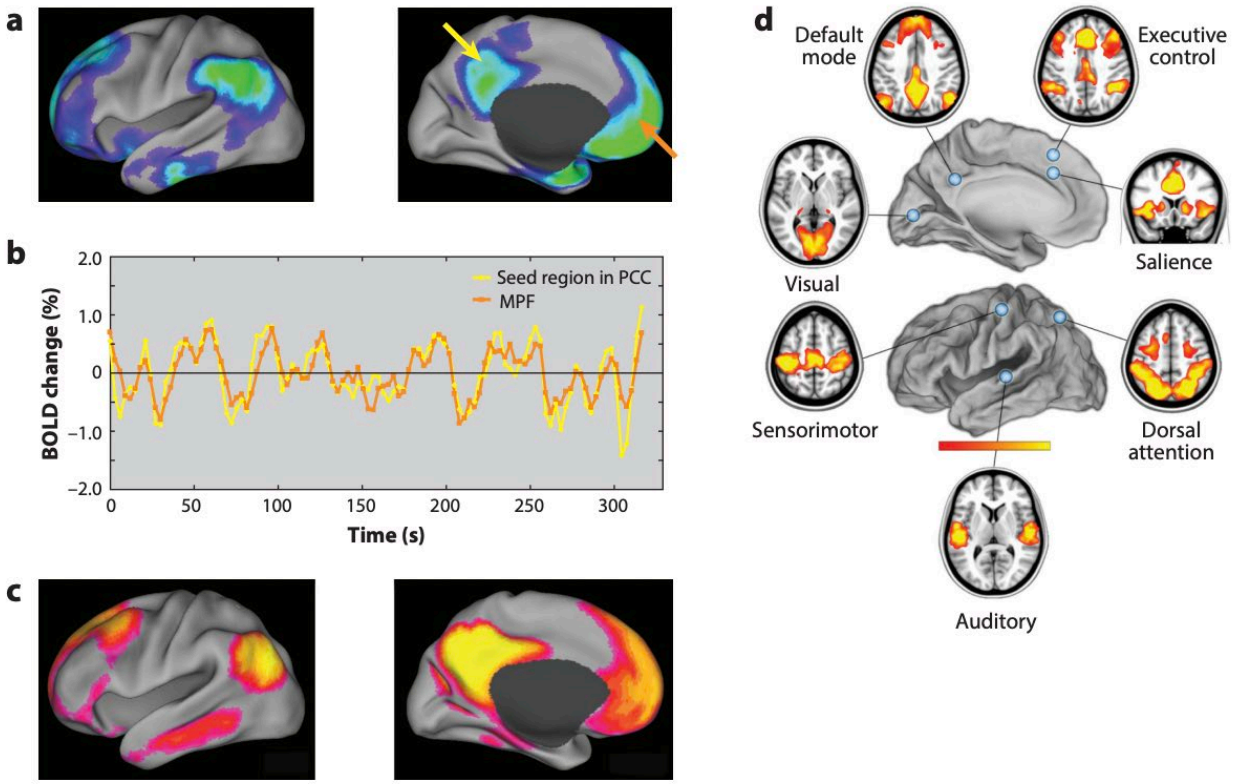

Figure 2 – Intrinsic brain networks detected using fMRI in humans. (a-c) topographical maps of correlation seed networks, with the seed region and region of interest plotted in yellow and orange, respectively. (d) Proposed brain networks dsicovered using seed-based correlation. Adapted from (Raichle, 2015).

RSFC has been used to expand our collective understanding of brain architecture, function and organization. While many applications of RSFC have been proposed and attempted, clinical applications of RSFC remains a significant challenge.

1.2 Dynamic Functional Connectivity

Further building on RSFC, Dynamic Functional Connectivity (DFC) expanded on the concepts of brain networks by focusing on the temporal dimension. The underlying theory that Dynamic Functional Connectivity research was borne out of posited that not only does the brain integrate a variety of intrinsic networks for a multitude of purposes, but that the connectivity patterns themselves are in a constant state of dynamic change. Dynamic Functional Connectivity

made use of the shorter FC windows (~30-60 seconds) for calculation of Functional Connectivity, calculating moment-to-moment changes by sliding the window to add a temporal dimension to Functional Connectivity changes (Figure 3). The resulting temporal collection of changing FC patterns is then clustered into discrete states, and shown to persist across subjects, as well as exhibit a degree of consistency regardless of the clustering metrics, held out datasets, or amount of preprocessing performed on the raw image sequences (Allen et al., 2014).

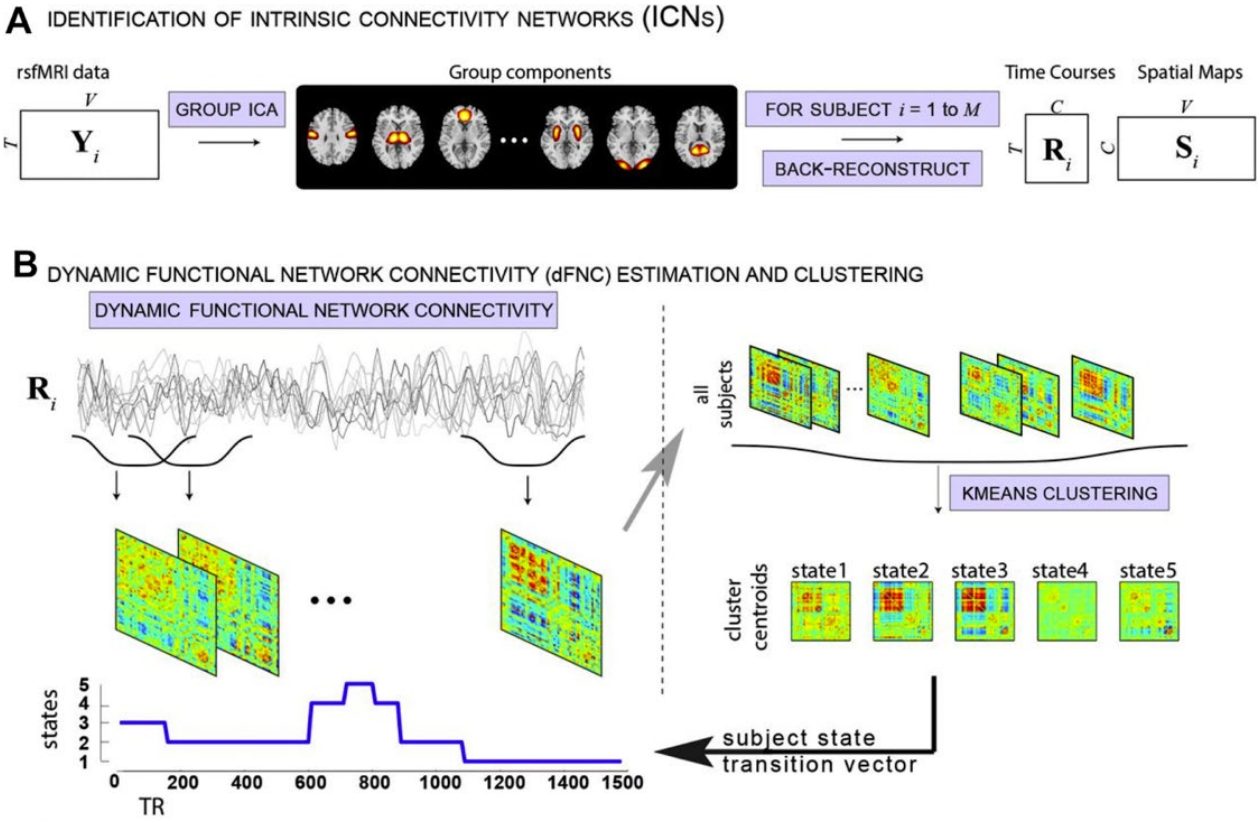

Figure 3 – Calculation of Dynamic Functional Connectivity in human fMRI. Adapted from (Allen et al., 2014). (A) Prepreocessing pipeline for identifying ICNs for further analysis. Data (Y) is decomposed into Group components, which consist of a TxC matrix of C timecourses with temporal length T, and matched Spatial maps. (B) Method flowchart for calculation of Dynamic Functional Connectivity measures. FC windows are calculated with a tapered sliding window, merged and clustered into 5 states. These stataes are then used to calculate the subject state transition vector. Adapted from (Allen et al., 2014).

Allen theorized that these time-varying aspects of Functional Connectivity "…may improve our understanding of behavioral shifts and adaptive processes." Continued work in the

field of Dynamic Functional Connectivity has shown some promise in the identification of neurological disorders including Autism Spectrum Disorder and Schizophrenia (Rabany et al., 2019), characterized by a state of restricted temporal patterns in patients suffering from these conditions. Additionally, it was observed that Schizophrenia patients exhibited a persistent weakening of connectivity patterns in a broad number of regions, along with a small subset of regions displaying increased connectivity. These findings support the idea that connectivity plays an important role in brain health, and could be used in the future as a biomarker of a variety of diseases and ailments.

There still remains a great degree of mystery and uncertainty in the meaningfulness of Dynamic Functional Connectivity measures. One question of note is the degree to which the underlying neural activity and/or behavior changes play a role in these dynamic shifts in Functional Connectivity. These are key questions that I aim to address in this work.

1.3 Intrinsic Signal Imaging (ISI)

As noninvasive human imaging modalities such as fMRI and EEG have seen rapid advancements over the last decade, advancements in more direct, invasive technologies such as Intrinsic Signal Imaging (ISI) grow in their use cases and applications in small animal, primate research, and even clinical uses (Hadjipanayis et al., 2011). ISI dates back to as early as 1977, when Frans Jöbsis demonstrated that blood oxygenation changes in the brain and heart could be measured in vivo using infrared light (Jöbsis, 1977). This discovery was the foundation of ISI, a diverse field of imaging modalities that encompasses techniques that can provide insight into how the brain functions both on the micro- and meso-scale (Grinvald et al., 1986; Orbach et al., 1985; Ts'o et al., 1990).

As hemoglobin contributes significantly to light absorption in blood, differences in the properties of oxygenated and deoxygenated blood can be exploited to not only measure overall oxygenation changes, but the dynamic changes in both oxygenated (ΔHbO) and deoxygenated (ΔHbR) hemoglobin concentrations (Bouchard et al., 2009). This improved upon earlier methods, which imaged at single wavelength, where the properties of oxygenated and deoxygenated hemodynamics cannot be unmixed. Modern ISI can utilize multiple wavelengths using a strobed light simultaneously measuring multiple signal sources in parallel. This allows for the simultaneous measurement of oxygenated and deoxygenated hemoglobin, which enables a more holistic view of oxygen consumption and supply changes in real time (Bouchard et al., 2009; Dunn et al., 2003). Figure 4 illustrates an example of ISI measurements in the rat cortex, which was used to better understand the spatiotemporal properties of hemodynamic responses to external stimuli. This work was carried out previously in the Hillman Lab.

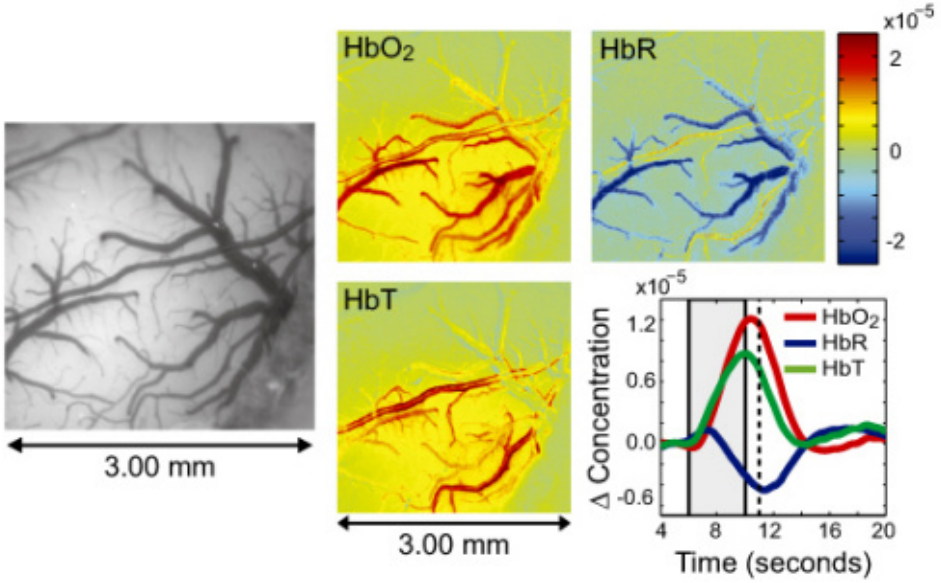

Figure 4 – Gray scale image of exposed rat somatosensory cortex during hindpaw stimulus. Images showing concentrations of HbO2, HbR, and HbT at t = 11 seconds (corresponds to dotted line on time course). Time courses showing the average change in HbO2, HbR, and HbT concentration across the entire field of view. Timing of hindpaw stimulus is shown in grey region. Adapted from (Bouchard et al., 2009).

1.4 Fluorescent Indicators of Neural Activity

Direct recordings of neural activity have been a fundamental part of neuroimaging, and originated as early as 1928, when Edgar Adrian recorded electrical impulses in nerve fibers using an electrometer (Adrian, 1954). Modern advances in engineering have produced a wide array of neural recording techniques, from direct recordings via electrode arrays to mesoscale recordings using voltage indicators (Peterka et al., 2011). Meanwhile, advancements in genetic tools have enabled the creation of Genetically Encoded Calcium Indicators (GECIs) (Akerboom et al., 2013; Chen et al., 2012; Miyawaki et al., 1997), which allow for observation of neural activity via fluorescence changes as a function of calcium influx in neural cell bodies.

Various GECIs have been developed over the years, which express fluorescence at varying wavelengths and for different cell populations. One GECI of note, GCaMP (Figure 5), fuses Green Fluorescent Protein (GFP) with Calmodulin and the M13 peptide sequence, which enables a fluorescent "trigger" upon calcium influx into neuronal cell bodies. This enables direct, real time in-vivo measurements of neural activity on a global scale, with minimal intervention due to transgenic mouse line development of GCaMP mice. This is just one example of a GECI in one species out of the multitudes that have been developed and used over the past few decades (Oh et al., 2019).

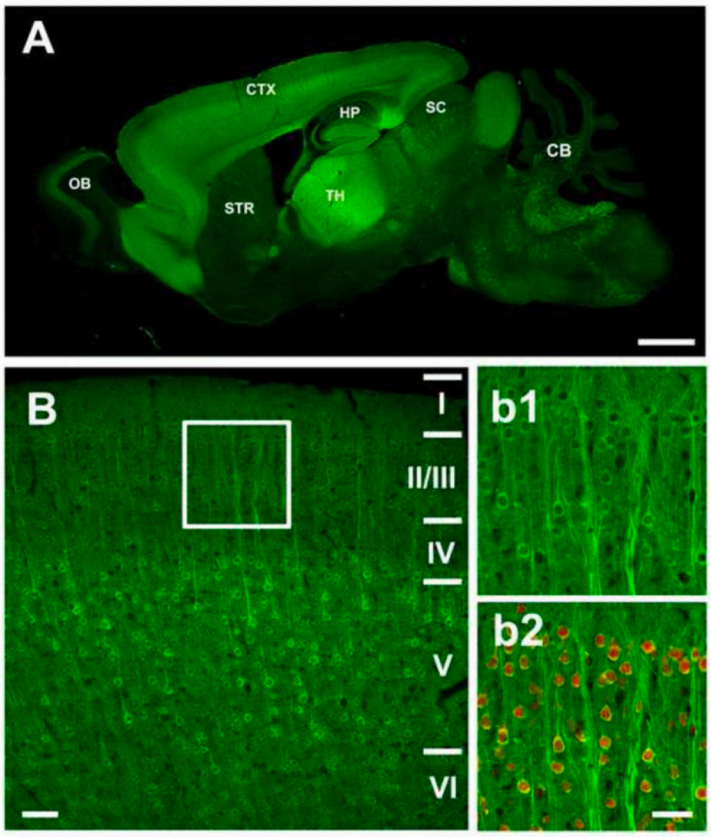

Figure 5 - Expression patterns of Thy1-GCaMP3 transgenic mice. (A) Section of brain from Thy-1 GCaMP3 mouse. Increased brightness represents degree of expression. Here, GCaMP3 is highly expressed in the cortex, hippocampus, thalamus, and other brain structures. (B) Confocal image of expression in motor cortex (M1), wigth cortical layers labeled on the right. Expression in layers II/III is shown in b1 and b2, respectively. Adapted from (Chen et al., 2012).

GECIs are valuable for a few reasons. First, they are less invasive than many other indicators such as viral or voltage type as the properties of transgenic labeling do not require loading, and are rather expressed in offspring. This not only improves surgical and experimental outcomes, but allows for high throughput experiments, as repeated imaging sessions do not require re-loading of dyes. Additionally, GCaMP expression levels remain consistently high throughout the mouse life cycle (2-12 months), allowing for ample opportunity to surgically prepare and chronically image mice. Proper management of mouse colonies allows for a large throughput of new subjects, as expression is passed down to offspring. Advanced genetic tools

allow for cell type specific labeling, which increases both specificity of labeling and image quality. For multiple population imaging, GECIs can be used in a wide variety of spectral ranges, allowing for versatile applications (Akerboom et al., 2013) such as dual-labeling or simultaneous imaging of intrinsic signals, which I take advantage of in this work. This allows for targeted expression of neuronal sub-populations, and is one key area of research in the Hillman lab to explore the interplay of excitatory and inhibitory neural activity.

1.5 Wide Field Optical Mapping

Wide Field Optical Mapping (WFOM) (Bouchard et al., 2009; Y. Ma et al., 2016) combines multispectral ISI with transgenic-enabled fluorescent neural recordings to measure hemodynamic and neural activity simultaneously in the brain. By performing a thinned-skull craniotomy and installing a chronic headplate with a transparent window, I can access and probe nearly the entire dorsal surface of the cortex of the mouse brain, all while the subject is awake and freely moving. WFOM has enabled investigation of a wide variety of scientific questions - from the effects of disease (Montgomery et al., 2019), to neonatal development (Kozberg et al., 2013), to the underpinnings of neurovascular coupling (Chen et al., 2017).

The ability to measure hemodynamic changes using ISI and neural activity using transgenic mouse lines provides a unique opportunity to study both signals simultaneously. By utilizing a strobed LED combined with optical tools to focus, collimate and align each light source, ISI and fluorescent imaging can be observed simultaneously in real-time. The development of improvements and new techniques in Wide Field Optical Mapping has been a major area of focus in the Hillman lab for over a decade.

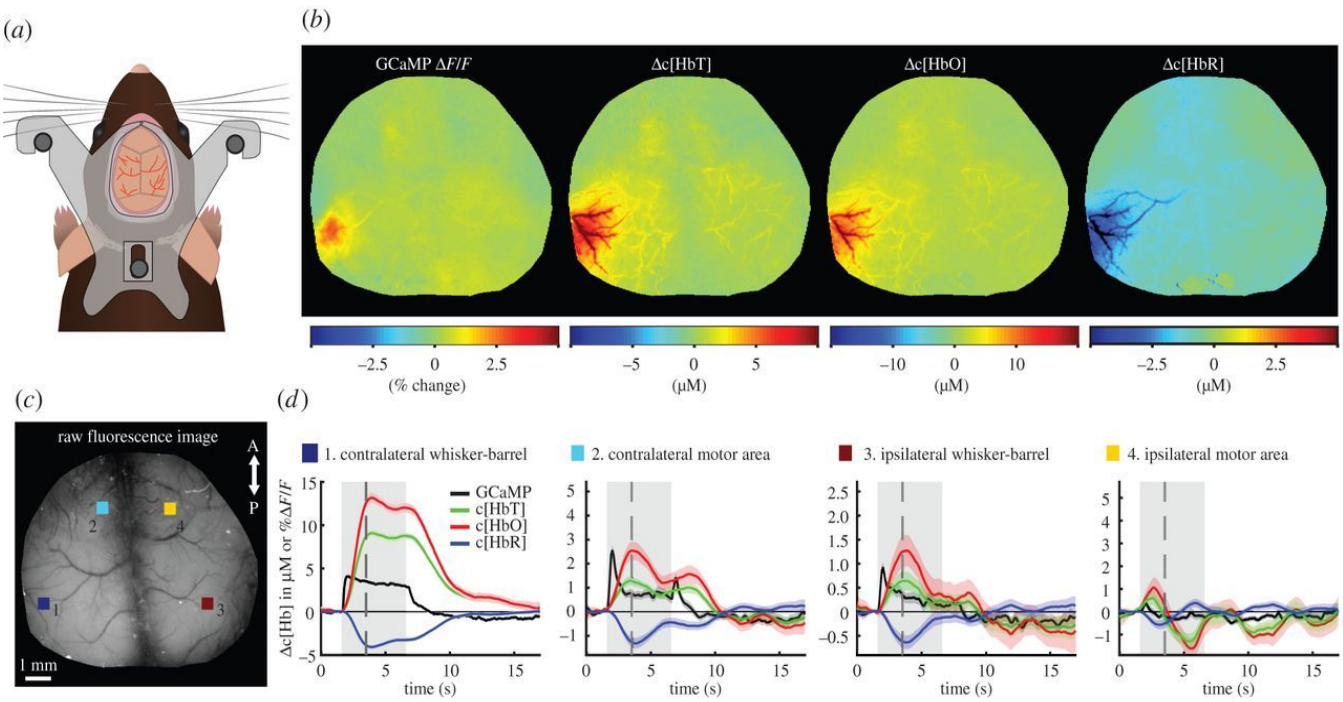

Figure 6 – Simultaneous imaging of neural and hemodynamic activity using Wide Field Optical Mapping. (a) Dorsal view of chronic headplate and cranial window. (b) Average stimulus response of GCaMP fluorescence activity, Total hemoglobin (HbT), Oxygenated Hemoglobin (HbO), and Deoxygenated Hemoglobin (HbR) (c) raw fluorescence image, with four ROIs (colored boxes). (d) Timecourses of average response to whisker stimulus. Each plot represents the average response to the representative ROI in (c). Adapted from (Y. Ma et al., 2016)

A majority of earlier experiments utilizing WFOM measured simultaneous changes in oxygenated and deoxygenated hemoglobin in transgenic Thy1-GCaMP mice, which expressed fluorescence in excitatory neurons in layers 2, 3, and 5 of the cortex. One of the primary discoveries that WFOM has enabled as of late is the validation of the link between cortical neural activity and the resulting change in hemodynamic activity, which has been theorized to support the metabolic demand of the aforementioned neural activity changes. This explanation for the fluctuations in hemodynamic activity is the foundation of modern human brain imaging, in particular the use of fMRI.

By harnessing the multispectral, multi-signal use case of WFOM, Ma and colleagues (Ying Ma et al., 2016) were able to validate this theory in Thy1-GCaMP mice, establishing a

non-linear predictive model that meaningfully linked resting state hemodynamics to the underlying neural activity (Figure 7). This work not only validated fMRI as a proxy for real time changes in neural activity, but also found similarities in the RSFC networks observed in human fMRI experiments.

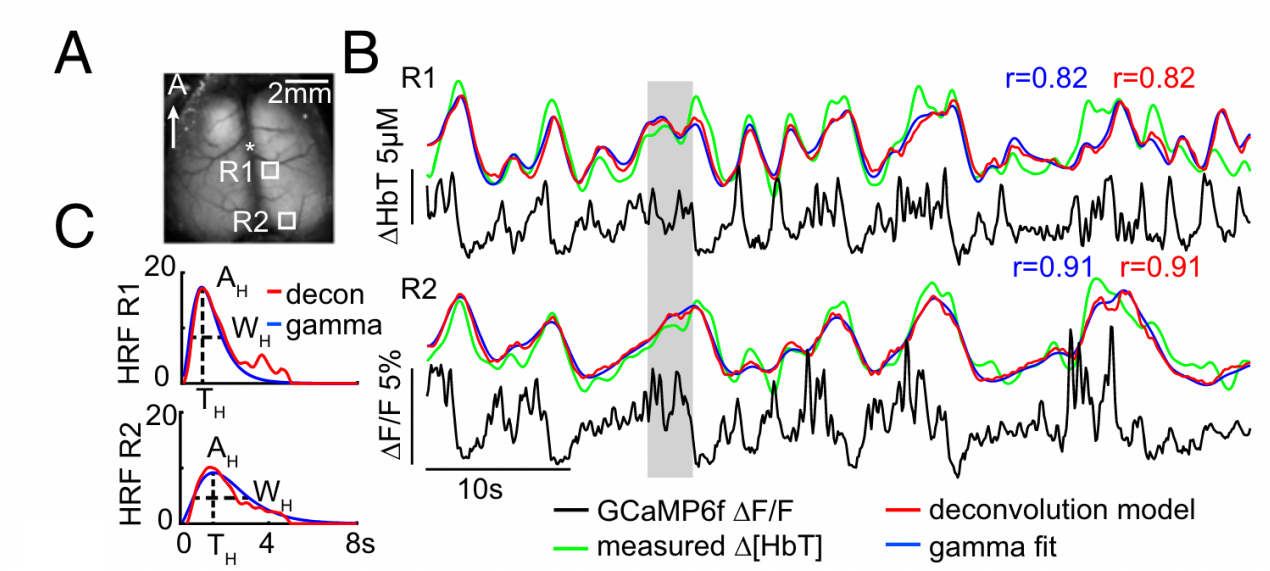

Figure 7 - Spatiotemporal modeling of hemodynamics from wide-field Thy1GCaMP6f recordings in the awake, resting brain. (A) Raw fluorescence image of neural activity from the mouse cortex. (B) Sixty-second examples of awake, resting-state GCaMP6f ΔF/F time courses (after hemodynamic correction) with simultaneously recorded ΔHbT from the two regions indicated in A (same trial). Red and blue traces show the results of convolving corrected GCaMP fluorescence with hemodynamic response functions (HRFs) derived via deconvolution or gamma-variate fitting, respectively. (C) Deconvolved Hemodynamic Response Functions for the time series shown in B. Adapted from (Ying Ma et al., 2016).

1.6 Harnessing WFOM to investigate Dynamic Functional Connectivity in the mouse

The recent discovery of Dynamic Functional Connectivity in the human brain continues to be a field of research with open questions concerning the sources and confounds of fluctuating correlation signals. At the same time, our research into the spatiotemporal link between neural activity and blood flow may provide insights into how these dynamic fluctuations map onto the same underlying neural activity.

The primary source of DFC signals is theorized to be changes in brain activity, which drives fluctuations in the BOLD response. However, linking brain activity to the corresponding changes in blood flow is still an active area of discussion and investigation. Previous work has validated the link between BOLD fluctuations and electrical brain activity (Britz et al., 2010; Brookes et al., 2011b, 2011a), while others have laid the foundation for dynamic changes in brain activity alone using techniques such as Magnetoencephalography (de Pasquale et al., 2010). Electroencephalography measurements have also validated these measures (Brookes et al., 2011a; Laufs, 2010), while some have found "microstates" in brain activity alone (Pascual-Marqui et al., 1995).

Based on the current open questions in Dynamic Functional Connectivity research, as well as the unique analytical perspective that WFOM provides, I concluded that WFOM is a good candidate imaging platform to explore the neural and behavioral underpinnings of Dynamic Functional Connectivity in the mouse. These findings can evaluate the link between neural and hemodynamic activity from the perspective of Functional Connectivity, while also providing a window into the behavioral markers of these widespread changes that were observed.

2 Chapter 2: Wide Field Optical Mapping: Experimental and Analytical Techniques

Modern neuroimaging techniques in humans are usually non-invasive, and typically utilize electromagnetic fields, radiation, and/or surface electrodes to quantify changes in brain activity. This reduces the risk of harm and injury in subjects compared to invasive techniques, but carries with it limitations in temporal and spatial resolution. Conversely, invasive imaging techniques used in animal subjects such as two-photon imaging or electrophysiology via electrode implantation produce datasets with higher temporal and/or spatial resolution. Great care is taken to reduce tissue damage during surgical preparation, and newer, less invasive techniques are constantly being developed and improved upon to further reduce these risks. A prominent example of this is the advancement in electrode design, as electrodes have rapidly improved through increased sensitivity, decreased size, and higher biocompatibility through material design improvements (Bhaskara et al., 2022).

However, these techniques are often limited to smaller areas of the brain, which reduces the spatial availability of data from each subject. Bridging the gap between these two techniques are wide field imaging techniques such as Wide Field Optical Mapping (WFOM), where a large portion of the surface of the cortex is imaged using a EMCCD camera combined with a strobed LED rig for simultaneous measurement of multiple intrinsic and/or fluorescent signals. WFOM allows for imaging vast areas of the brain's cortical surface, accessing a significant population of cortical brain activity while still maintaining a high spatial and temporal throughput. WFOM builds on previous advancements in imaging, such as Intrinsic Signal Imaging (ISI).

2.1 Animal Preparation

Recent trends in imaging in the awake, behavioral brain require the development of more sophisticated methods for implanting cranial windows. Awakening and imaging animals immediately after cranial window surgery may result in data that are strongly affected by animal discomfort and distress. Therefore, it is more common practice to implant a window under anesthesia, carefully retrieve the animal with analgesia and rest, and then image over the next few days, which has the advantage of being able to image the same animal multiple times longitudinally, such as in in studies of learning, development or disease progression. It is also worth considering how the animal's head is fixed relative to the camera during imaging. To this end, various designs have been developed for "head plates" that surround the exposed area, and are often attached to the skull during initial cranial window surgery (Hillman, 2007).

In all cases, the surgical preparation must be completely sterile and performed while the mouse is under anesthesia, usually preoperatively (and subsequently) with analgesics such as buprenorphine to relieve postoperative pain. Small cranial windows with skull and sometimes dura mater removed are common in in vivo two-photon imaging experiments. However, larger imaging windows (as required for WFOM) longitudinally are much more difficult to maintain on a craniotomy.

The techniques used for animal preparation with WFOM have been improved on over the years, and now allow for reliable chronic imaging over multiple imaging sessions in a single animal. Our approach builds upon skull-thinning approaches developed by Drew and colleagues (Drew et al., 2010), but utilizes this technique to expose the entire dorsal surface of the skull. To improve signal clarity and allow for awake head fixation during imaging sessions, I performed a

thinned skull craniotomy, followed by a headplate installation for each mouse used in WFOM experiments.

2.1.1 Thinned skull craniotomy

Surgical preparation of optical windows is performed under isoflurane anesthesia. For all surgical preps, animals are first placed into a sealed plexiglass container, and 2.5% isoflurane gas is administered until no righting response is observed. Animals are then transferred to a surgical area, with a homeothermic heating pad and heading controller (CWE TC-1000 Mouse Temperature Control System) set to maintain an internal body temperature of 37°C, while maintaining appropriate anesthetic depth. Throughout the surgery, mice are checked for anesthetic depth using a toe pinch and observation of a slow but consistent breathing rate.

To prepare the surface of the skull for thinning, the skin is sanitized using alcohol and iodine wipes, then shaved. Next, the skin surrounding the dorsal surface of the skull is removed, and the whole surface of the skull is cleaned and dried in preparation for skull thinning. Next, skull thinning is carried out using a set of progressively smaller burr drills, beginning with large burrs and progressively decreasing in size as the skull is thinned to an approximate thickness of 50 microns. This minimizes light scattering while imaging through the skull, while maintaining appropriate intracranial pressure by preserving a thin layer of skull. While previous experiments avoided drilling over the skull sutures due to concerns of damaging larger blood vessels, I found that careful, methodical drilling can smooth out the entire surface while preventing any skull punctures or significant brain bleeds. After thinning, the skin is retracted and secured in place with cyanoacrylate glue.

2.1.2 Chronically implanted headplate for immobilization

For immobilization during imaging sessions, a custom laser cut acrylic headplate was designed (Figure 8). This method allows for custom, rapid fabrication of headplates for any mouse, which are lightweight and unobtrusive. The design encloses the exposed cortex on both sides and is glued to the skull with cyanoacrylate (gel super glue). To protect the thinned skull during recovery, a layer of Kwik-Sil, a two-part fast-curing silicone rubber, is placed over the window, which can be peeled off for imaging. Post-operative care ensures that the animal receives adequate hydration, pain relief, and is in an environment where it cannot catch or damage its head plate. Training animals to perform behavioral tasks can be done before surgery (head immobilization) and after surgical recovery.

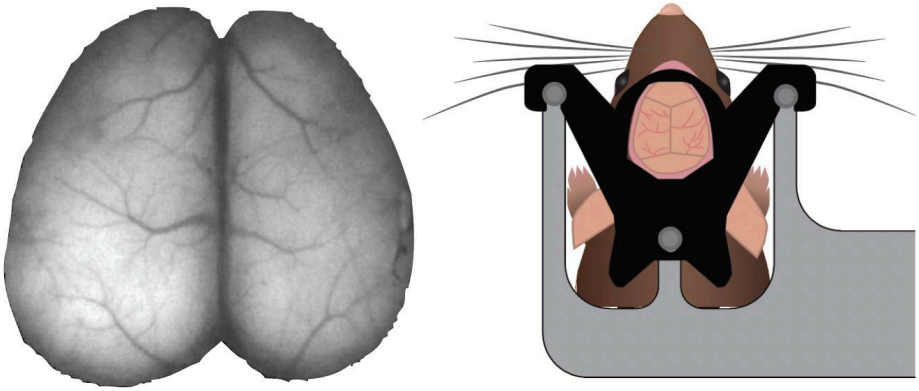

Figure 8 – (Left) Raw fluorescence image of neural activity in chronically implanted window. (Right) Illustration of head fixation. The head restraint (black) is attached to the headplate holder (grey) using three screws.

Similar methods have been used to map the cortex of cats and primates. In the latter case, the chronic window involves surgical removal of the dura within the window, and the cranial window can be disassembled and cleaned to ensure long-term optical clarity (Sirotin and Das, 2009).

2.2 WFOM Instrumentation

2.2.1 Optical system design

The WFOM imaging is composed of three fundamental elements:

1) High powered, collimated LEDs. These illuminate the dorsal surface of the mouse cortex, and are used at different wavelengths to measure either intrinsic or fluorescent signals.

2) Optical path - collimating/focusing lenses and band-pass filters guide and filter the light into narrow specifications to provide consistent results with an optimal signal-to-noise ratio.

3) A high-throughput, high sensitivity EMCCD camera, which measures the resulting intrinsic and fluorescence signals for analysis.

These elements make up the core components of the WFOM system used in this work. The LEDs are strobed at a high frequency, illuminating the brain briefly in each target wavelength, which is synchronized to the camera's exposure signal. This guarantees that each sequential image captured by WFOM was only illuminated by one target wavelength. The LED sources are collimated and merged into a single optical path using a custom-built LED assembly, which is mounted above the imaging plane and focused uniformly on the surface of the brain. The returning light (either via intrinsic signal or fluorescence) is then focused onto the camera's sensor using a camera lens, which allows for fine adjustments to focal length and aperture for a high-quality image that maximizes dynamic range during imaging. Before the image meets the camera sensor, it passes through an emission filter, which removes extraneous sources of unwanted light as well as the excitation light of the fluorescent LED (if one is used), as this would interfere with the fluorescence image.

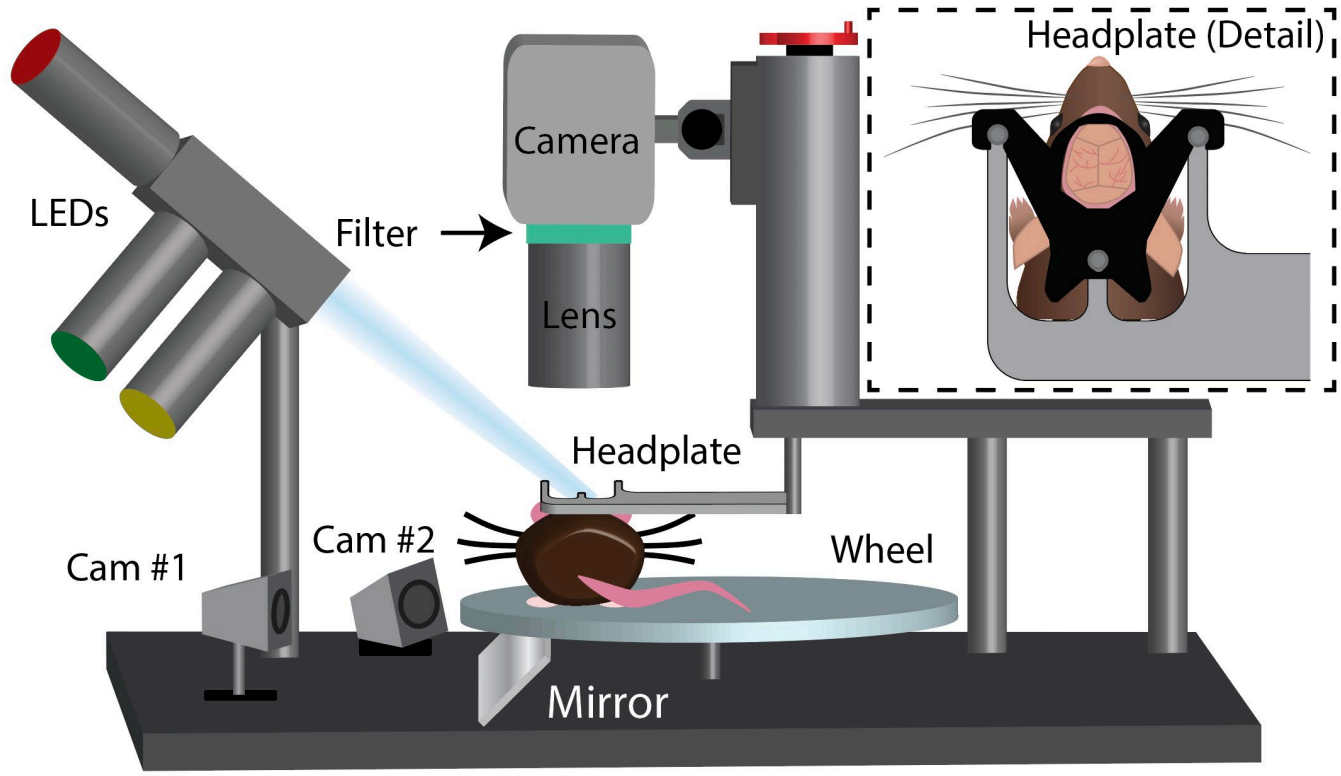

Figure 9 – Experimental setup diagram for Wide Field Optical Mapping (WFOM) system. The mouse is head-fixed to a free spinning acrylic and silicone wheel. The LED array is composed of three LEDs: Red (650nm), Green (560nm), and Blue (490nm) or Lime (535nm). The LED beam path is placed so that the spot fully and uniformly illuminates the brain surface (shown in the detail cutout top right). The camera is positioned so that the cortical surface occupies most of the FOV. A vertical stage allows for adjustments in the camera height, and positional adjustments are made by moving the head plate holder and wheel assembly on a separate breadboard.

2.2.2 Behavioral apparatus design

The behavior apparatus was designed to facilitate freedom of movement during imaging sessions, with the constraint of rigid head fixation to stabilize the temporal image sequences. Additionally, these components had to allow for unobstructed views of mouse behavior throughout imaging for behavior analysis.

A freely moving wheel was built using laser-cut acrylic and fastened to a central post, with added fastening points to allow for fine adjustments in the wheel position. To the same central post, an extension rod and headplate mount was added over the left side of the wheel,

where the mouse is head fixed for imaging sessions. This headplate mount is a custom machined aluminum piece, with three tapped screw holes for fastening the mouse to the head fixation stage. Finally, a mirrored piece of acrylic was secured at a 45-degree angle beneath the wheel, allowing for an additional view of the mouse from below.

In preliminary testing, it was observed that while mice would often position themselves on the wheel properly, there were occasions where they would grip the edge of the wheel and contort their bodies, resulting in poor behavioral monitoring and little to no wheel movement. Additionally, the mouse would often move its tail directly over its head, obscuring the camera and interfering with data collection. To address this, an L shaped piece of clear acrylic was fashioned, which served as a ceiling and wall, preventing both of these events from occurring. Finally, I also noticed that mice struggled to grip the smooth surface of the acrylic, so a thin piece of translucent silicone was cut to the same size as a wheel and placed on the surface, providing improved grip and comfort during experiments.

2.2.3 Isolation Apparatus

Two isolation techniques were used to facilitate robust data collection. First, the entire WFOM rig was placed on an air table, preventing environmental vibrations from impacting image stability. Second, the entire rig was enclosed in a black box for environmental light and noise isolation. This box was built using a rectangular aluminum frame, black cardboard walls, and a heavy cloth curtain on the front for ease of access to the imaging rig between experiments.

2.2.4 Input/Output Hardware

All image and behavior acquisition, as well as experimental control was controlled using a HP Z Series workstation desktop, using Windows 8. For neuroimaging acquisition, The Andor Zyla EMCCD camera was supplied with a proprietary PCID card for high throughput image

acquisition. Both FLIR behavior cameras were also connected using a dual port USB 3.0 PCID card. To synchronize the LED strobing to the camera acquisition, the exposure signal of the primary camera was routed to an Arduino Uno. The Arduino Uno was responsible for togging each LED in a cyclical sequence each time the camera exposure signal cycled. This results in three interlaced acquisition sequences - one for Red, Green and Lime LEDs respectfully.

2.2.5 Software

Image acquisition was operated using a combination of manufacture supplied and custom-built tools. Andor's supplied software was interfaced with a custom application (Sun et al., 2010), which allowed for the additional control of LED sequencing, as well as simplified controls for parameters such as image resolution, exposure time, file naming and diagnostics. For behavior cameras, alignment as setup was accomplished using the FLIR Blackfly image acquisition software. A custom python software package (Thibodeaux, 2020) was designed to drastically increase disk write times, allowing for dual behavior cameras acquiring at 60 frames per second and at a resolution of 1440 x 1080 pixels per camera. This software package also allowed for auxiliary recording of behavioral measurements and Preliminary data analysis was performed in real time to verify the overall quality of the collected data using a custom MATLAB GUI.

2.2.6 Behavior Acquisition

In order to simultaneously track behavioral dynamics in tandem with neural and hemodynamic activity, the WFOM system was integrated with a custom-built dual camera behavior monitoring system. This system was designed to track a multitude of behavioral metrics, including (but not limited to) paw position, nose position, whisker deflection, pupil size,

and tail movements. To enable as much behavioral information capture as possible, two cameras were positioned to maximize capturing all body movements.

Camera #1 was positioned at a wide angle, capturing the full left side of the mouse body. A mirror was positioned beneath the clear behavior wheel at a 45-degree angle, providing an underside view of the mouse. This angle allowed for observation of paw and tail movements. Camera #2 was positioned closer and with a tighter FOV to capture all facial and eye movements on the left side of the mouse, allowing for measurement of pupil size, nose movements and whisker deflection.

For this system, I used two FLIR Blackfly S monochrome USB cameras (BFS-U3-16S2M-CS), based on previous behavioral research in mice (Pereira et al., 2019). To synchronize webcam images with WFOM, both cameras were triggered using the hardware exposure signal of the Andor Zyla EMCCD camera. This produced a single frame from each camera for every frame captured using WFOM.

2.2.7 Automated behavior tracking using DeepLabCut

Image analysis of complex behavioral metrics is itself a challenging task, and has been the subject of numerous computer vision solutions by a variety of research groups. To simplify the analytical pipeline, I sought to utilize an image analysis pipeline that was simple to use, and relatively automated so that any new data could be efficiently and accurately labeled without requiring excessive busy work for each new dataset collected. DeepLabCut, a markerless pose estimation software developed by the Mathis group (Mathis et al., 2018), was one solution found to be the best approach to fit these goals.

DeepLabCut utilizes deep learning in combination with a small training set of labeled images to automatically track the position of any number of markers in a set of video frames.

This is accomplished using the freely available software, along with pretrained models and GPU accelerated optimization in a Google Colab GPU virtual environment. DeepLabCut was used to create automated tracking models of pupil, whisker and paw movements for all behavioral analysis shown in this work. Figure 10 illustrates a single labeled frame, and Supplemental Movie 8 shows a video example of labeled data.

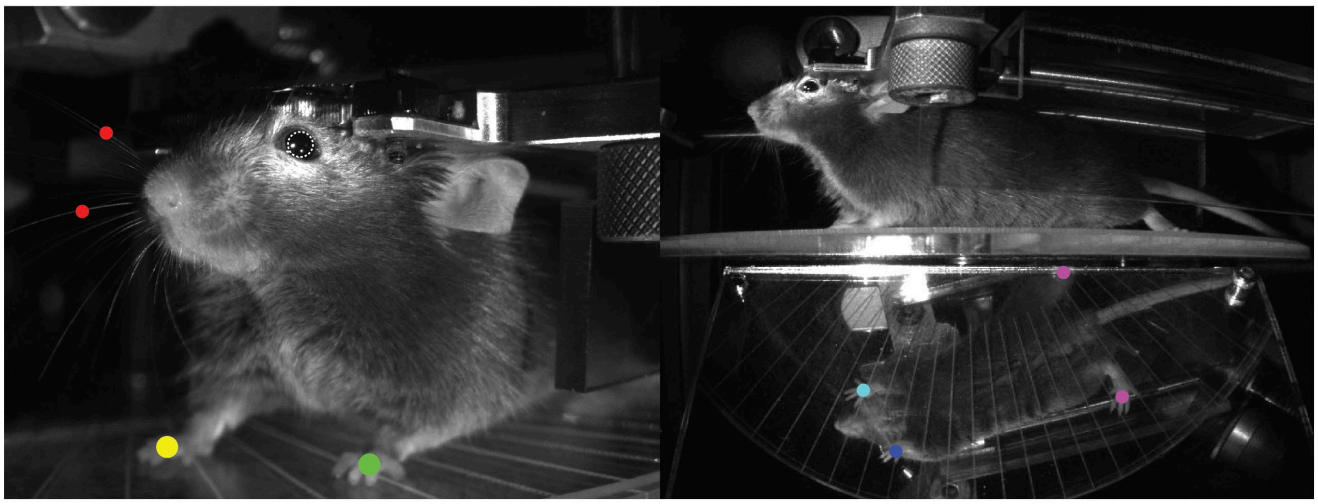

Figure 10 – Example webcam images of freely behaving mouse, with example DeepLabCut annonations as colored points. Images were captured in real time, using two FLIR Blackfly S USB webcams, along with angled mirrored acrylic to capture paw movements from below. The mouse is moving on a clear acryic wheel, and is head fixed for simultaneous imaging of brain activity. The white dotted ellipse is an estimated pupil tracking using behavioral markers obtained from the pupil outline.

2.3 Estimation of Hemodynamic Activity from Intrinsic Signals

Note: This section is adapted from the peer reviewed publication (Y. Ma et al., 2016), of which I am a contributing author.

As already discussed, the basic method for performing WFOM is to illuminate the brain with multiple wavelengths of strobed light in sequence to acquire measurements of changes in various neurological measures. This produces a sequence of 2D images that are acquired while the animal is being stimulated, performing a task, or being observed at rest. Raw images usually show the brain's surface vasculature with good contrast, as well as signals from more diffuse,

deeper light. When a discrete region of the cortex is activated, the intensity of diffuse light changes within that localized region. This change can be captured with a camera and used to map hemodynamic changes in the cortex. Early research found that the main factor responsible for changes in diffuse reflectance is hemoglobin absorption (Malonek and Grinvald, 1996). Moreover, hemoglobin is known to have an oxygenation-dependent absorption spectrum in the visible and near infrared range, corresponding to the bright red color of arterial blood and the darker brown color of venous blood (Figure 11). It was, therefore, recognized that measurements of diffuse-reflectance changes at specific wavelengths across the hemoglobin absorption bands would differently represent contributions from changes in the local concentration of oxy- and deoxy-hemoglobin (ΔHbO and ΔHbR) as well as their total (ΔHbT = ΔHbO + ΔHbR), which represents a change in local blood volume.

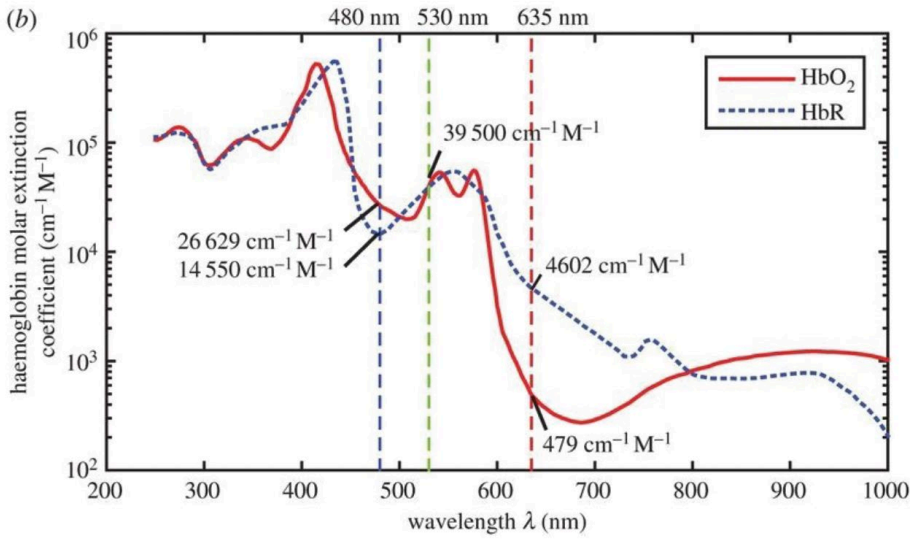

Figure 11 - Spectra of oxygenated and deoxygenated hemoglobin, with target wavelengths for ISI and the excitation wavelength for GCaMP, a target GECI used in WFOM experiments. The red continuous line represents the extinction coefficient of light passing through oxygenated hemoglobin, while the dotted blue continuous line represents the extinction coefficient of light passing through deoxygenated hemoglobin. Dotted vertical lines represent common intrinsic illumination targets for ΔHbO (Red, 635nm), ΔHbR (Blue, 480nm) and ΔHbT (Green, 530nm).

The raw images acquired at different wavelengths carry clear information about the concentrations of ΔHbO and ΔHbR within the cortex. However, to convert reflectance data into estimates of changes in the concentration of hemoglobin, the physical principles of light propagation in scattering brain tissue must be examined. In a simple, absorbing but non-scattering medium the transmission of light will follow Beer's law:

$$I = I_0 e^{-\mu_a x} \tag{2.1}$$

where I_0 is the incident intensity, and I is the resulting intensity after the light has travelled a pathlength x through the medium with absorption coefficient μ_a. However, the brain is highly scattering at visible wavelengths. In fact, scattering is what permits light entering the brain's surface to be diffusely reflected and detected by a camera focused on the brain's surface. As scattering turns the incident light around, each scattering event adds to the photon's pathlength through the absorbing medium. This redirection also introduces spatial uncertainty in terms of where a photon detected at a particular point on the brain originally entered the brain, and where it visited within the brain. Finally, the light emerging from the brain will exit in a range of directions, based on its last scattering event, such that every photon entering will not necessarily be detected by the aperture of the camera lens. In practical implementations, it is impossible to know precisely how scattering has affected each detected photon across the field of view. However, the overall effects of scattering on Equation 2.1 can be approximated by the 'modified Beer Lambert law':

$$I = I_0 e^{-\mu_a x + G} \tag{2.2}$$

2.3.1 Hemodynamic Contamination of Fluorescence Signals: Correction Methodology

In-vivo wide-field imaging of fluorescent markers comes with the challenge of hemodynamic cross-talk throughout the imaging session. Dynamic changes in blood flow lead to changes in light propagation that are not linearly coupled to neural activity. This property was highlighted in previous work (Y. Ma et al., 2016) where uncorrected fluorescence signals fluctuated in a manner that was both uncorrelated with direct recordings of neural activity (via EEG), and showed a high correlation with changes in blood flow. Thus, a technique was developed to approximate hemodynamic contamination by utilizing the already known reflectance measures collected in the Green and Red LED channel.

In previous experiments with an earlier GECI (GCaMP6f), the spectral properties of hemoglobin were used in a multispectral imaging system to calculate the various wavelength-dependent Differential Pathlength Factors (DPFs), allowing for a hemodynamic correction to model the true fluorescence intensity changes. However, the near-green excitation wavelength of jRGECO1a fluorophore at 565nm provides an opportunity to simplify the correction methodology, as the lime excitation channel can be approximated using the green excitation image.

Figure 12 illustrates a model of light propagation in the cortex after accessing jRGECO1a fluorophores. Incident light with intensity I_1 penetrates the cortex, and strikes a fluorophore with intensity I_2. The ratio of I_2 to I_1 is governed by the Beer-Lambert Law, where the absorptive coefficient of the medium and the pathlength of the incident light through the medium (X) affect the intensity as follows:

$$I_2(t,\lambda_{ex}) = I_1(t,\lambda_{ex})e^{-\mu_a(t,\lambda_{ex})X(\lambda_{ex})} \quad (2.3)$$

The emission intensity $I_2(t,\lambda_{ex})$ produced by the fluorophore excitation intensity $I_1(t,\lambda)$

is modulated by signal F(t), a proxy for neural activity of the cell, and is represented as:

$$I_1(t,\lambda_{em}) = I_2(t,\lambda_{ex})F(t) \quad (2.4)$$

The emitted light that reaches the surface of the cortex $I_2(t,\lambda_{em})$ is calculated in a similar manner:

$$I_2(t,\lambda_{em}) = I_1(t,\lambda_{em})e^{-\mu_a(t,\lambda_{em})X(\lambda_{em})} \quad (2.5)$$

We can then approximate F(t) by rearranging equation 2.4, then substituting terms from equations 2.3 and 2.6 (Note the rearrangement of terms into one exponent):

$$F(t) = \frac{I_1(t,\lambda_{em})}{I_2(t,\lambda_{ex})} \rightarrow \frac{I_2(t,\lambda_{em})}{I_1(t,\lambda_{ex})} e^{\mu_a(t,\lambda_{em})X(\lambda_{em})+\mu_a(t,\lambda_{ex})X(\lambda_{ex})} \quad (2.6)$$

Returning to the Beer-Lambert law in its general form, I can approximate any reflectance light as follows:

$$I_R(t,\lambda_R) = e^{-\mu_a(t,\lambda_R)X(\lambda_R)} \quad (2.7)$$

By substituting and rearranging the reflectance data collected at the green and red wavelengths, I can approximate the raw fluorescence signal:

$$F(t)I_1(t,\lambda_{ex}) = \frac{I_1(t,\lambda_{ex})}{I_R\left(t,\lambda_{green}\right)^{X_g} I_R(t,\lambda_{red})^{X_r}} \quad (2.8)$$

X_g and X_r are approximations of the DPF for excitation vs. green, and emission vs. red respectively:

$$X_g = X(\lambda_{ex})/X(\lambda_{green}), X_r = X(\lambda_{em})/X(\lambda_{red}) \quad (2.9)$$

These correction factors X_g and X_r can be used to eliminate the hemodynamic contamination present in a raw lime reflectance image sequence, with the assumption that all images are taken simultaneously.

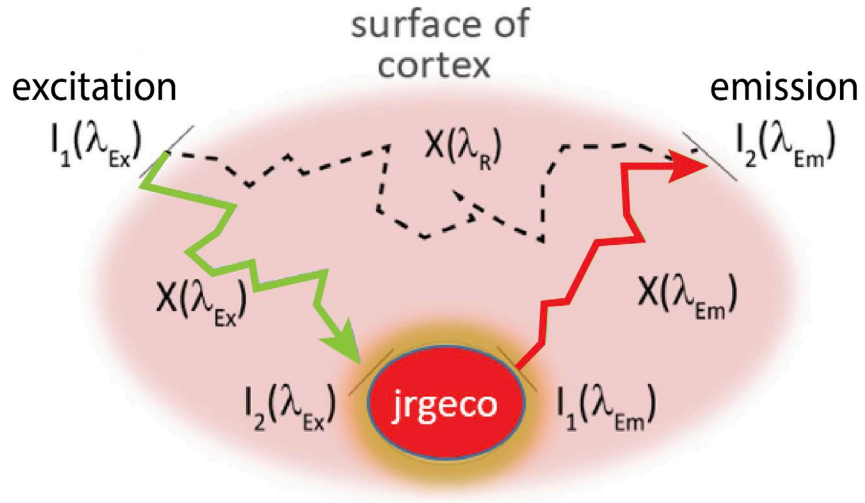

Figure 12 – Illustration of excitation and emission light from a jRGECO1a fluorophore in a cortical neuron. Excitation light (I_1, lime) from an LED enters the tissue and is scattered before reaching the jRGECO1a fluorophore (red oval). Fluorescence emits green light (I_2, red), which is also scattered by the tissue before exiting the sample and passing to the imaging sensor (not shown).

2.3.2 Estimating hemodynamic cross-talk correction factors

The challenge for hemodynamic correction then lies in deciding upon appropriate correction factors X_g and X_r. In order to develop a process for estimating these correction factors, I had to first determine how to detect and subsequently define sufficient and deficient correction. Ideally, a well-corrected neural dataset contains no blood vessel artifacts, and returns to baseline after a response (either spontaneous or due to external stimuli). A dataset with insufficient correction will contain one or both of these confounds. Since the data collected in these experiments was free of stimuli, the best approach for approximating the optimal correction

factors is to minimize the occurrence of blood vessel artifacts. This problem can be reduced to a two-dimensional optimization.

2.3.3 Detection and quantification of vessel artifacts

Figure 13 illustrates an example of a sufficiently and insufficiently corrected dataset. In order to detect the presence of the vessel artifacts shown, the image gradient G(F) is calculated on both the raw fluorescence and baseline divided fluorescence image, keeping the maximum value. It is important to assess both raw fluorescence and baseline divided fluorescence images, since correction errors may propagate to both images, and baseline division may inadvertently remove the artifact, while failing to properly correct for hemodynamic artifacts. Thus, the conversion quality factor Q for a single frame is calculated as follows:

$$Q(X_r, X_g, t) = max\left(G(F(t)|X_r, X_g), G\left(\frac{F(t)|X_r, X_g}{F_0(t)|X_r, X_g}\right)\right) \tag{2.10}$$

Since I aimed to approximate the ideal correction factors for a functional dataset, I generalized this process by measuring Q across an epoch of data, and measuring the pixel-wise maximum value across that epoch. Finally, a threshold is applied to the result, and the fractional value of pixels above the threshold is assessed for a final conversion quality metric $Q_t(X_r, X_g)$ is calculated, which has bounds [0,1].

Estimation of ideal correction factors can be approached in two ways – using a brute force search, or by generalizing the process using an optimization function.

2.3.4 Estimation of ideal correction factors using brute force search

Brute force searching offers the distinct advantage of understanding the impact that correction factors have on the resulting neural dataset. Figure 13 shows a brute force search in the domain $X_r = [0,2]$ and $X_g = [0,.3]$, and the resulting quality metric $Q_t(X_r, X_g)$. A clear

minimum can be observed at $X_r = 1.1$, $X_g = 0.2$. In addition to a clear understanding of the objective function minimum, I also observed the shape and tolerance of the minimum, illustrating a potential range of acceptable values for X_r and X_g, where the quality metric is only marginally worse.

However, brute force searching comes at the cost of computation time. The domain of evaluation is somewhat arbitrary, so a minimum may not exist in the domain given, requiring a second evaluation. Additionally, the resolution of the domain is a trade-off of computation time for accuracy, so an exact optimum must be interpolated from the results.

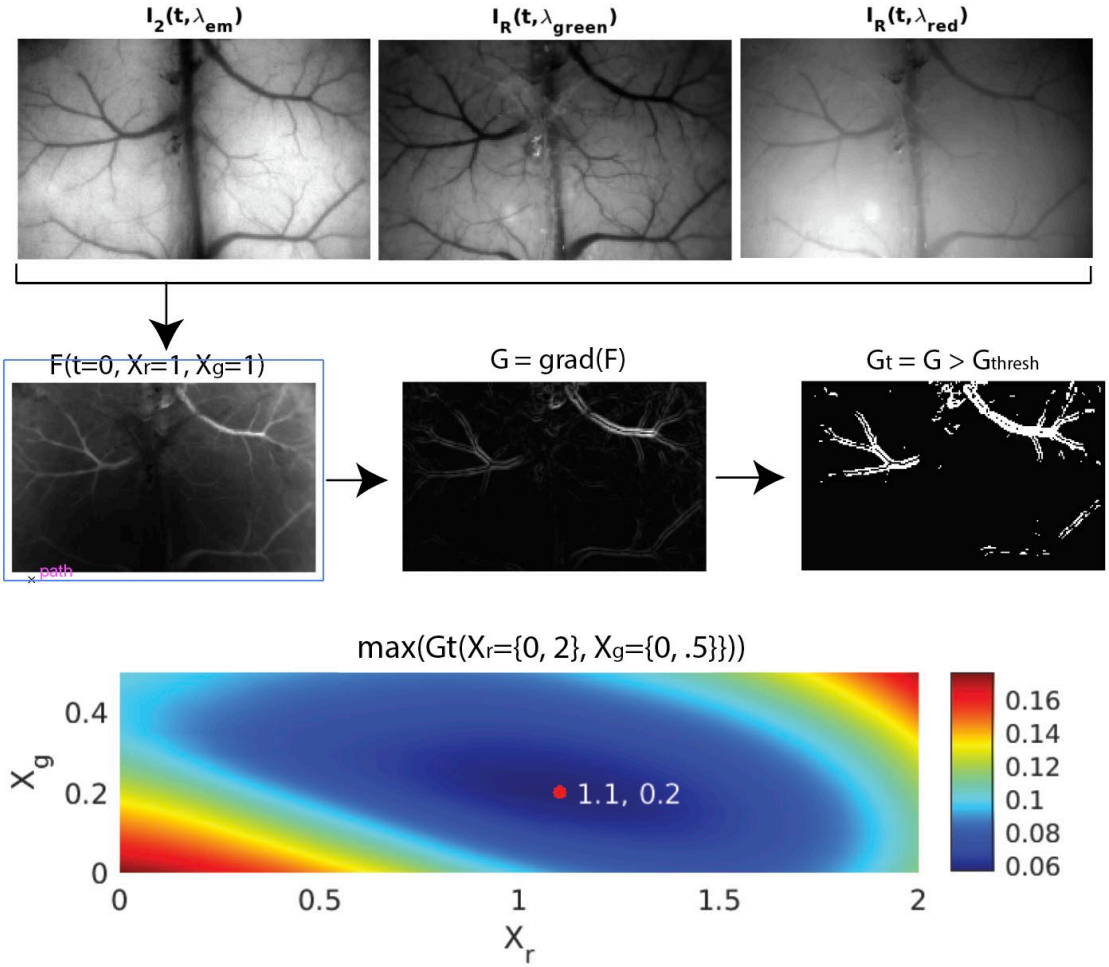

Figure 13 – Estimation of ideal hemodynamic correction factors for jRGECO1a conversion. (Top) raw images of fluorescent, green reflectance, and red reflectance images, respectively. (Middle, left) example of a single frame of converted data, using Xr = 1 and Xg = 1. (Middle, middle) gradient of previous image, highlighting blood vessel artifacts. (Middle, right) thresholded image of previous, used to calculate overall conversion quality. (Bottom) evaluation of various correction factors, showing minimal error ar Xr = 1.1, Xg = 0.2.

2.3.5 Estimation of ideal correction factors using an optimization function

A second approach I attempted utilizes an optimization function to reduce computation time, as well as automate correction estimation. A variety of optimization approaches could be used, but for this analysis the built-in MATLAB function optimfsearch was used. While this approach did save computation time, improper initial conditions could sometimes result in no minima being found, or impossible values being reached (such as negative correction factors). Thus, it is important to understand the general range that correction factors lie in to avoid rapid divergence from an acceptable domain. Alternatively, a bounded optimization function could be used to prevent physically improper DPF estimations. Based on these results, I decided to use the brute force search approach, which is computationally expensive but more reliable.

2.3.6 Baseline drift in reflectance imaging datasets

Both hemodynamic and neural activity are not represented as an absolute measure, but rather as a relative change according to a baseline, which must be measured at rest. These approximations of hemodynamic and neural activity assume that a given baseline is representative of a baseline measurement at all given timepoints. This approach was assumed to be reliable in previous experiments (Y. Ma et al., 2016; Montgomery et al., 2019), which used a block design, where each trial was separated into ~60 second intervals, and the baseline was measured prior to simulation in each epoch. The experimental design in this work consisted of ten-minute imaging sessions, with no stimulus periods throughout.

During preliminary analysis, it was discovered that certain LED signals would occasionally exhibit a global linear drift, indicative of some extraneous noise source (Figure 14A). I hypothesized that these could be due to environmental changes such as slow drift of the LED position/angle or LED power fluctuations due to overheating, as the drift was typically constant and had no correlation with behavioral or experimental changes. This drift was a confound in analysis, as this caused the baseline used for hemodynamic and neural activity to shift, leading to erroneous negative/positive values (Figure 14 illustrates this in the bottom left plot in red).

We considered two approaches to correcting slow signal drifts in these experiments. The first approach was to apply a temporal high-pass filter to the affected timecourses. This is a common method of removing global signal drifts that are either not due to physiological changes or are not a signal of interest for analysis. However, it is computationally complex, and carries a risk of removing actual physiological information as low frequency changes in blood flow have been observed in both humans and animals.

A second approach was to periodically measure the baseline throughout the imaging session, as this would eliminate any slow drifts entirely. This technique consists of three steps, and is illustrated in Figure 14. First, qualifying epochs are detected, which must contain no movement signals both within the epoch and outside of a buffer defined as 50 percent of the epoch length both before and after the epoch tails. Thus, the epoch "test area" is defined as two times the length of the epoch itself. Each epoch's baseline values and location are then compiled in order to calculate the dynamic baseline. The dynamic baseline is calculated as a temporal linear interpolation between the two nearest baselines at each time point across the imaging session. This removes sudden discontinuities between baseline epochs.

This approach is less computationally demanding than applying a temporal filter to all data. Figure 14 illustrates an example of a red LED time course with a signal drift, as well as the signal drift removed using the technique described above.

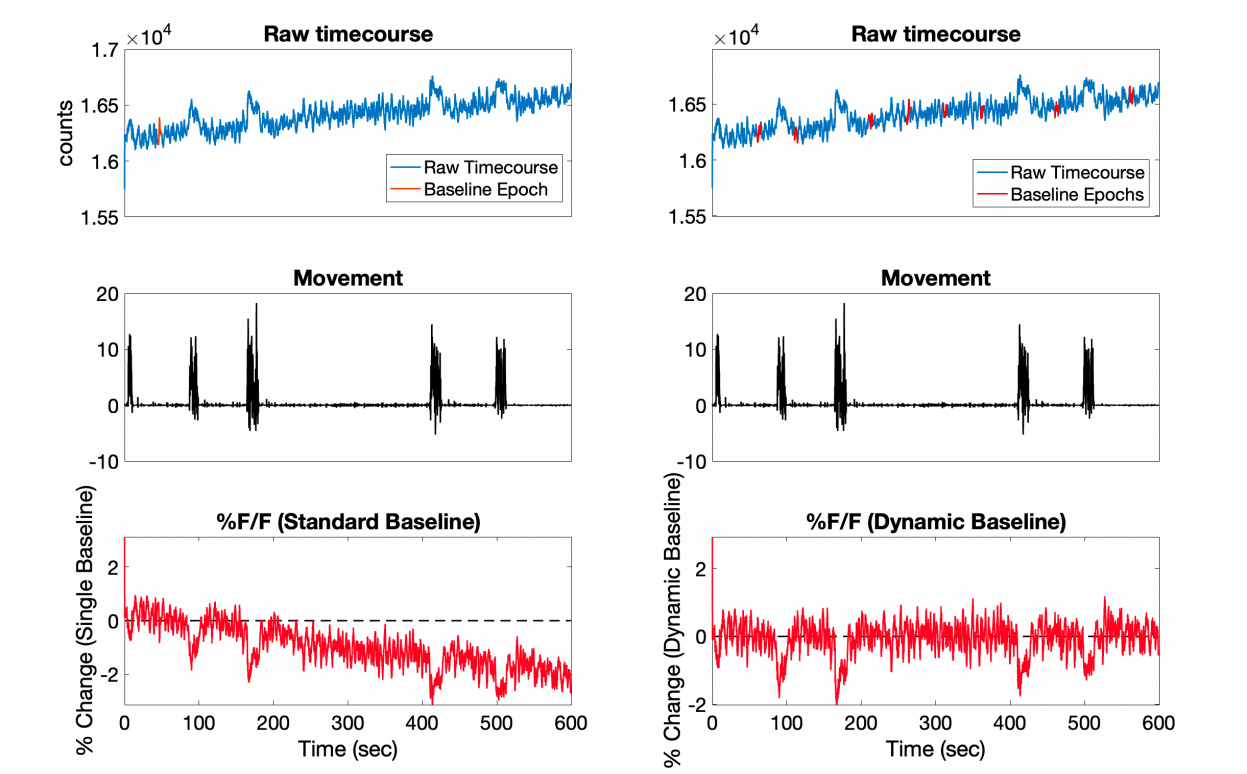

Figure 14 – Illustration of signal drift in raw LED timecourses. The Left plots show the standard baseline approach, while the right plots show the dynamic baseline approach. (Top) Raw timecourse, with signal drift shown as an increasing linear trend from beginning to end of epoch. Red segments are used as epochs for baseline calculation. (Middle) Mouse movement signal used to detect periods of rest for baseline measurement. (Bottom) Original signal from top converted to percent signal change with respect to baseline (bottom left, standard baseline, bottom right, dynamic baseline).

2.3.7 Filtering emission and extraneous signals

After striking the cortical surface and either scattering or fluorescing the target brain tissue, the returning light must enter the camera lens and focus onto the imaging sensor. However, extraneous light sources not intended for acquisition must still must be dealt with. For this experimental setup, two target passband wavelength ranges were identified to contain the valuable intrinsic and fluorescent light. First, the green (500-550nm) light range is necessary to

capture the intrinsic signals from the green LED. Second, a broad red (575-650nm) passband is necessary to capture both the intrinsic signals from the red LED, as well as the emission light from the jRGECO1a fluorophore, which has a peak emission intensity at 590nm. All other wavelengths either contain information that is not needed, or is a nuisance signal, which includes the intrinsic signal from the lime excitation LED, as well as the infrared light source for behavioral webcam illumination.

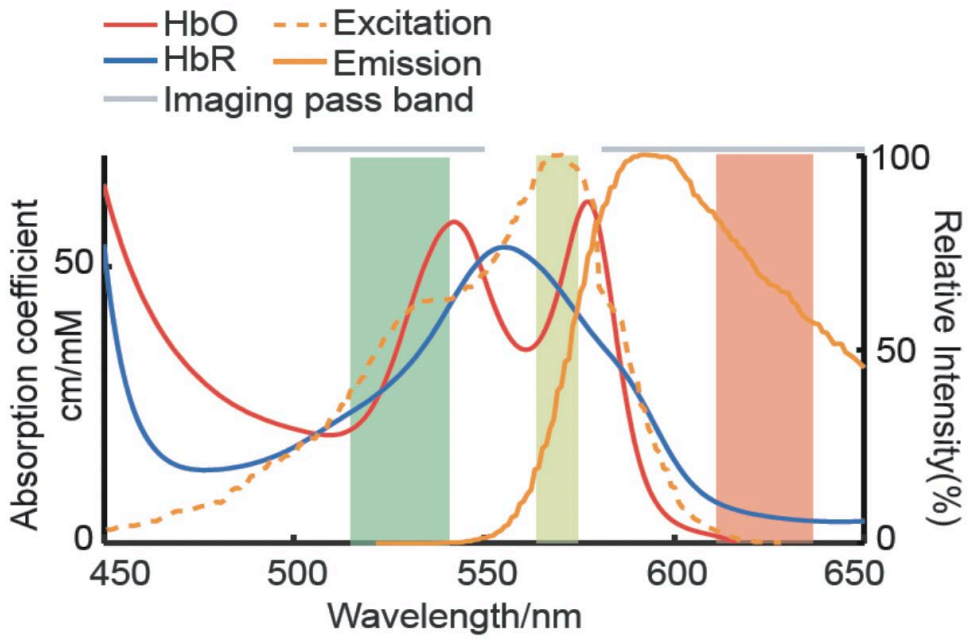

Figure 15 – Absorption coefficients of Oxygenated (HbO, red) and deoxygenated (HbR, blue) hemoglobin, along with relative intensities of excitation (orange, dotted) and emission (orange, solid) light for jRGECO1a fluorescent protein. Colored bars represent bandpass filters used for each LED. The gray line (top) indicates the imaging pass band filter used before light enters the camera imaging lens.

2.4 Summary

In this chapter, I outlined the methodologies used to simultaneously measure hemodynamic and neural activity in the mouse cortex. I also documented the techniques used to observe and measure behavioral measures in parallel, utilizing high speed cameras in combination with DeepLabCut for markerless estimation of whisking, pupil and locomotion

changes throughout each imaging session. These techniques summarize the key components of the operation of WFOM for imaging neural and hemodynamic activity in the mouse.

3 Chapter 3: Clustering and Audiovisualization of Real-Time Neuroimaging Data

Current techniques for in vivo brain imaging provide large amounts of multi-dimensional, dynamic data. Recent improvements to these techniques allow real-time recordings, enabling observation of spontaneous events, as well as compelling 'resting state' activity (Bouchard et al., 2015; Y. Ma et al., 2016; Xiao et al., 2017). This inundation of data to analyze and understand brings with it a challenging task: to take large datasets and distill them into concise representations that preserve the information content of the data and offer insights into the mechanisms generating the spatiotemporal patterns observed (Friedman, 1997; Mwangi et al., 2014).

Dimensionality reduction is becoming mainstream in the analysis of in-vivo microscopy data to extract the shapes and time-courses of firing neurons (Pnevmatikakis et al., 2016) and is similarly the basis of resting state fMRI analysis, which extracts spatial 'functional connectivity networks' based on the temporal correlations of different regions of the brain (Di and Biswal, 2015). However, the outputs of these spatiotemporal unmixing methods are rarely re-combined into meaningful representations from which real-time interactions and inter-component spatiotemporal patterns and dynamics can be easily appreciated.

Modern neuroscience experiments also include recordings of behavior, such as whisking, and spontaneous running, stimulus presentations, tasks such as lever pushing, and parameters such as task performance speed and correctness. These recordings often begin as video streams. Feature extraction from these behavioral recordings is achievable (Kabra et al., 2013; Tort et al., 2006), and can provide an input for machine learning algorithms. However, it can be challenging to determine which of the many features in the video are relevant, and spatial tracking

parameters extracted from videos will not necessarily be linearly related to neural representations (e.g. breathing rate, or the speed of a movement). Conversely, the human brain is very good at such feature extraction from video streams. The problem is that interrogating two or more video representations (brain imaging data and behavioral recordings) at the same time is almost impossible for the human visual system to achieve.

To overcome these issues, I demonstrate here methods for representation of brain imaging data in both the visible and audible space, providing an intuitive representation of high-dimensional data that can be listened to in parallel with viewing videos of behaviors, and spatial representations of the data. Audible representations of electrophysiology signals have long been used to guide electrode placement and distinguish signal from noise, while enabling simultaneous use of the eyes and hands. The idea of representing EEG and fMRI data from awake humans as audio streams has also been demonstrated previously (Wu et al., 2013, 2009), in addition to data from mouse brain slices (Ikegaya et al., 2004). Our approach improves upon these demonstrations by providing a toolkit for routine encoding of a wide variety of parameters by leveraging sound's ability to simultaneously depict multiple dimensions of dynamic information in parallel. Pitch, volume, note velocity, attack speed, stereo sound and even musical instrument type are all parameters that can all be leveraged for auditory stream encoding. Since all of these aspects are easily recognized and unmixed by the human auditory system (Pauletto and Hunt, 2005), a great deal of information can be compressed into a single audio stream for real-time evaluation of brain imaging data and associated behavior, providing a unique way to recognize patterns, motifs, co-activations, delays, rhythms and repetitions not easily noticed by eye alone. As a further dimension for encoding, our approach also provides visual representations of spatiotemporal dynamics of the data using colors, further expanding our

ability to utilize our sensory system to integrate and interpret the properties of each dynamic system.

We demonstrate our approach on three different types of experimental neuroimaging data with audiovisualization of gradually increasing complexity: Wide-field optical mapping (WFOM) of neural activity to compare the mouse brain under awake and anesthetized conditions (ketamine/xylazine), cellular-level resolution recordings of apical dendrite intracellular calcium activity in the awake mouse brain using swept confocally aligned planar excitation (SCAPE) microscopy (Bouchard et al., 2015), and wide-field simultaneous neural and hemodynamic recordings of the awake mouse cortex, along with behavioral recordings. I also developed a python-based graphical user interface pyanthem (Automated Neuroimaging Timecourse Heuristic Methodology) that is capable of reproducing these audiovisualizations and extending the use of this method to wider ranges of dynamic spatiotemporal data. See the Appendix for full details of this open-source toolkit.

3.1 Materials and Methods

For all wide field experiments in this chapter, transgenic CB57BL/6 Thy1-GCaMP6f mice were used. Surgical preparation was performed as described in Chapter 2, with the same recovery and post-monitoring protocol. For all awake WFOM experiments, Mice were head-fixed on a freely moving custom-made horizontal wheel and imaged for up to 90 minutes per session. Three high powered LEDs (Thorlabs, M490L2, M535L2 and M625L3) at wavelengths of 490 nm (Blue), 535 nm (Green), 625 nm (Red), were strobed to capture hemodynamic (red and green) and neural (blue) fluctuations simultaneously. In addition, a long-pass filter was mounted in front of the camera to block excitation light (FF01-496/LP-25, Semrock), and band-pass filters were placed in front of each LED (FF01-475/28 for blue, FF01-530/43 for green, and

FF01-623/24 for red). Images were captured using an Andor Zyla sCMOS camera, running at 31.22 Hz and an exposure time of 23.4 ms. Raw images were captured at a resolution of 512x512 pixels, and an approximate FOV size of 15x15mm. For hemodynamic correction, hemodynamic contributions to detected GCaMP fluorescence signals were calculated using a method previously described (Chapter 2), where red and green reflectance measurements were used to derive estimated values of hemodynamic absorption contributions to (blue) excitation and (green) fluorescence emission light. Behavioral measures were only captured in the final experiment (summarized in Figure 23), and utilized an earlier camera setup of only one camera capturing gross behavioral movements.

3.2 Analytical Methods for decomposition of neural activity

Here, I will summarize key algorithms for decomposing and reducing high dimensional datasets to low dimensional representations. These techniques are a core aspect of my thesis work, and are utilized throughout this and future chapters.

3.2.1 Nonnegative Matrix Factorization

Non-Negative Matrix Factorization (NMF)(Lee and Seung, 1999) seeks to approximate a dataset V as a product of two lower dimensional matrixes:

$$V = W \times H \tag{3.1}$$

Given a dataset V with dimensions $m \times n \times t$, where M and N are spatial dimensions and t is the time dimension, NMF decomposes the dataset into k spatial (W) and temporal (H) components, where W has dimensions $[m \times n, k]$ and H has dimensions $[k, t]$. NMF can be initialized randomly, or operate from some initial conditions, operates until H and W no longer change. There are a few different NMF algorithms, but one popular and simple technique uses the multiplicative update method:

Algorithm 1 NMF via multiplicative update

1: Initialize: $\boldsymbol{W}$ and $\boldsymbol{H}$ non negative.

2: Update values in $\boldsymbol{W}$ and $\boldsymbol{H}$ by computing the following:

3: **repeat for** $\boldsymbol{n}$

4: $$H_{[i,j]}^{n+1} \leftarrow H_{[i,j]}^{n} \frac{((W^n)^T V)_{[i,j]}}{((W^n)^T W^n H^n)_{[i,j]}}$$

5: $$W_{[i,j]}^{n+1} \leftarrow W_{[i,j]}^{n} \frac{(V(H^{n+1})^T)_{[i,j]}}{(W^n H^{n+1}(H^{n+1})^T)_{[i,j]}}$$

6: **until** $\boldsymbol{W}$ and $\boldsymbol{H}$ do not change.

Using this algorithm, it can be shown that the distance $V' - V \rightarrow V - W \times H$ is non-increasing when utilizing this algorithm (Lee and Seung, 1999). Figure 16 illustrates a decomposition of raw neural data into 12 components.

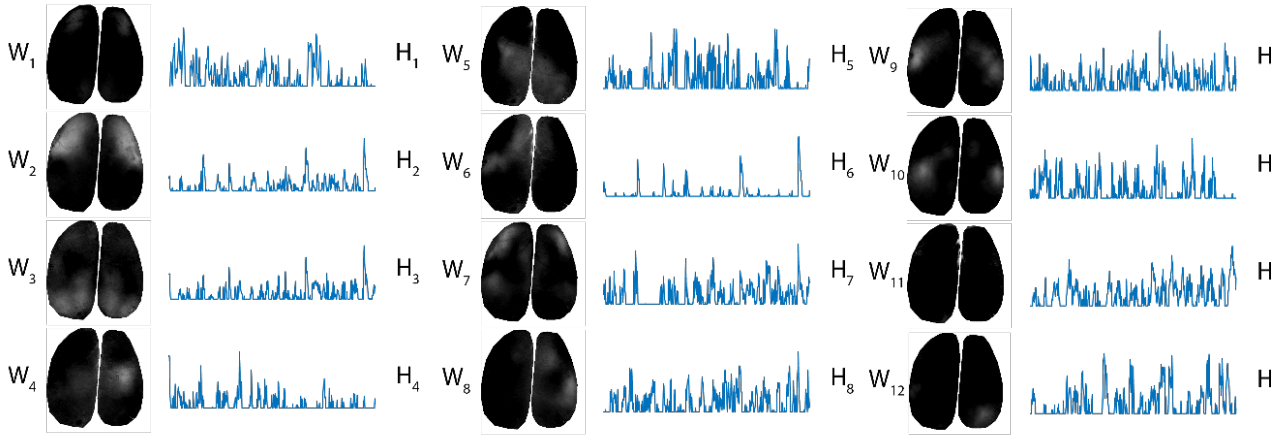

Figure 16 – Nonnegative Matrix Factorization decomposition of raw neural activity. Each image represents one of 12 spatial components W_n, while each timecourse represents the corresponding temporal component H_n. These 12 components approximate the raw dataset V via the product V′ = W x H.

3.2.2 Concerns when using NMF

It was observed that the temporal components H were not an exact representation of the raw fluorescence changes, but was rather an average of the representative weights in its corresponding W component. This is intrinsic to how NMF operates, as the optimization function implements a form of "fuzzy clustering" i.e. each pixel in the input image can be assigned to multiple components. This aspect of nonnegative least squares decomposition must

be taken into consideration, as unsupervised nonnegative least squares produces an altered output that does not recapitulate the original signal in single components, abstracting the decomposition in a way that may mislead during further analysis.

A second concern of nonnegative least squares as a decomposition tool is the non-negative constraint. All negative values are ignored when calculating the decomposition, and fitting the model to the constraints. This leads to a non-optimal solution, as negative fluorescence changes are valuable and should be considered and used when decomposing these datasets. Thus, it was decided to explore other methods that decomposed the data, but did not misrepresent or incompletely summarize it.

3.2.3 K-means Clustering Decomposition

K-means clustering is a mixture model that seeks to partition a dataset into K components by minimizing the distances between the cluster centroids and the labeled data points. K-means operates using the following algorithm (Hartigan and Wong, 1979):

Algorithm 2 k-means clustering

1: Specify the number of clusters to assign
2: Randomly initialize k centroids
3: **repeat**
4: **expectation**: Assign each point to its closest centroid
5: **maximization**: Compute the new centroid (mean) of each cluster
6: **until** The centroid positions do not change.

Typically, centroids are initialized randomly, which leads to variance in output assignment. However, new algorithm improvements such as kmeans++ have improved the consistency of outputs, and significantly reduced solutions at local minima.

Since this dataset is temporal in nature, distance is used to calculate centroids along the time dimension. Figure 17 shows an example of k-means decomposed data, where a period of resting state neural activity was decomposed into 18 clusters, producing a topographical map

across the cortex that is largely symmetric, and has well partitioned regions with clear, unambiguous borders.

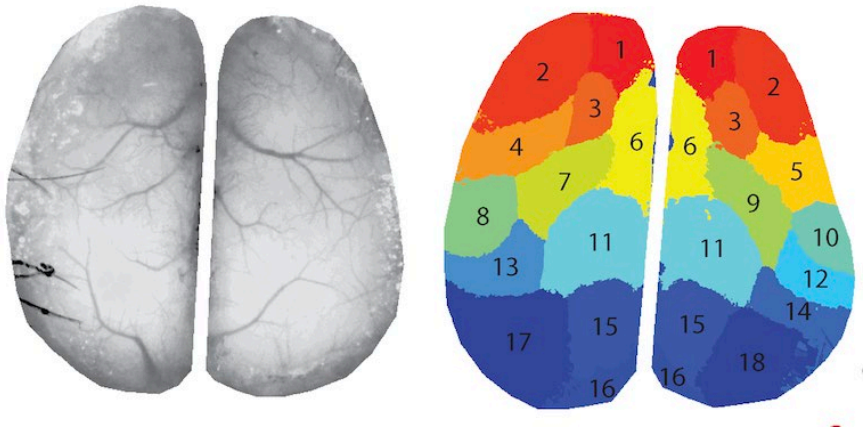

Figure 17 – Kmeans clustering of neuronal activity. (Left) Raw image of fluorescence channel in the Thy1-GCaMP6f mouse. (Right) Kmeans output from a 60 second epoch of resting state neural activity.

With these clusters, I can now use them as ROIs for a low dimensional representation of a raw dataset. This radically compresses our raw data stream, and allows for the design of an automated time course extraction process, whereby a set of ROIs can be defined, and then extracted from a multitude of imaging sessions.

3.2.4 Non-negative least squares decomposition

We next sought to better represent the raw data visually by utilizing a least-squares approximation of input timecourses. This is advantageous for visualization and analysis purposes, since I want to create a spatial model of the input data, while preserving the timecourses. It can also serve as a goodness of fit test for k-means clustering or any other decomposition techniques, as a reconstruction of the raw data should preserve a majority of the variance in the raw dataset. I utilized the nonnegative least squares algorithm to reconstruct the raw data as a summation of temporal components H and calculated spatial components W. Here, the raw dataset is referred to using V, while the reconstructed approximation is referred to as V'.

It is important to note that nonnegative least squares does not modify the input timecourses, but rather fits the spatial components to best approximate the original dataset. I then took the k-means clusters from the raw data as ROIs to form a basis time course matrix H, and then utilized non-negative least squares to approximate the spatial components W:

Algorithm 3 Nonnegative least squares approximation

1: Input: Data matrix $V \in \mathbb{R}^{F \times N}$, latent dimension K, regularization weights $\lambda_1, \lambda_1 \geq 0$ *and* $\lambda_2, \lambda_2 \geq 0$, maximum number of iterations t_{max}
2: **Initialize** $\boldsymbol{W}^0 \in \mathbb{R}^{F \times K}, \boldsymbol{H}^0 \in \mathbb{R}^{K \times N}$
3: **For** $\boldsymbol{t = 0, 1, \ldots, t_{max} - 1}$
4: $\quad \boldsymbol{W}^{t+1} := \underset{W \in \mathbb{R}^{F \times K}}{\arg\min}\, G_1(W | W^t, H^t)$
5: $\quad \boldsymbol{H}^{t+1} := \underset{H \in \mathbb{R}^{K \times N}}{\arg\min}\, G_2(H | W^{t+1}, H^t)$
6: **End**
7: **Output**: Basis matrix $W^{t_{max}}$ and coefficient matrix $H^{t_{max}}$ which approximate Input matrix V.

This procedure is iterated until W no longer changes after an update. Applying nonnegative least squares to a resting state GCaMP dataset using 12 components, I obtained the basis and coefficient matrixes shown in Figure 18. Supplemental Movie 2 shows a comparison of a raw dataset with the decomposed NNMF reconstruction and the residual. nonnegative least squares not only reproduce a majority of resting state activity using only 12 components, but effectively denoises the dataset.

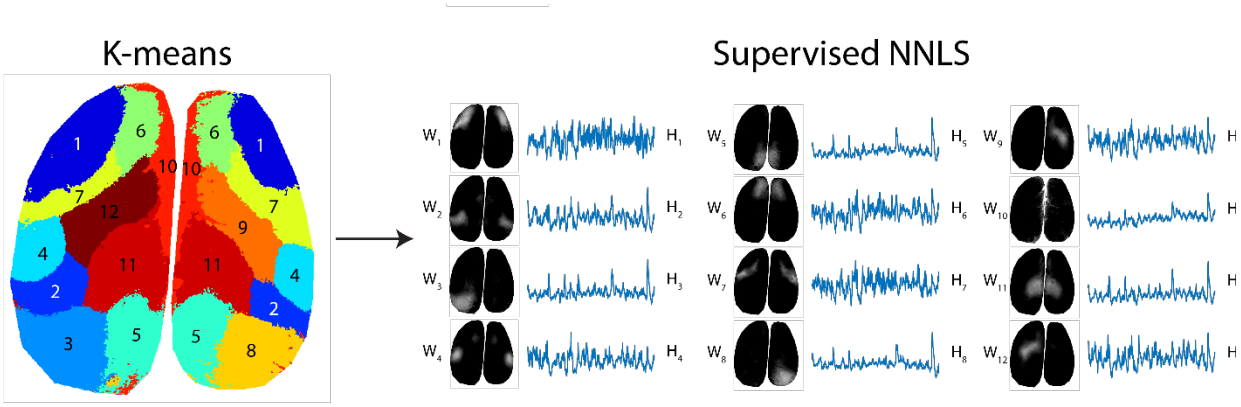

Figure 18 - Nonnegative least squares approximation of resting state neural activity, carried out by first decomposing the dataset via K-means clustering (left), then by

representing the decomposition via nonnegative least squares (right). Timecourses on the right are extracted from the ROIs on the left, and Spatial maps are calculated using a nonnegative least squares approximation.

This technique preserves the original extracted timecourses, while also providing a clear reconstruction of the original data.

3.2.5 Methods: Audiovisualization process

The 4 steps of data processing for audiovisualization are shown in Figure 19. Note that this process is generalized i.e. can be used for a variety of neuroimaging datasets. First, data is spatiotemporally unmixed into a dimensionally-reduced representation. This step is best achieved via the analysis method most common to the imaging modality being used, but could include principal component analysis (PCA), non-negative matrix factorization, k-means clustering, seed-based non-negative least squares fitting or other specialized blind source separation methods (Berry et al., 2007; Giovannucci et al., 2018; Wold et al., n.d.).

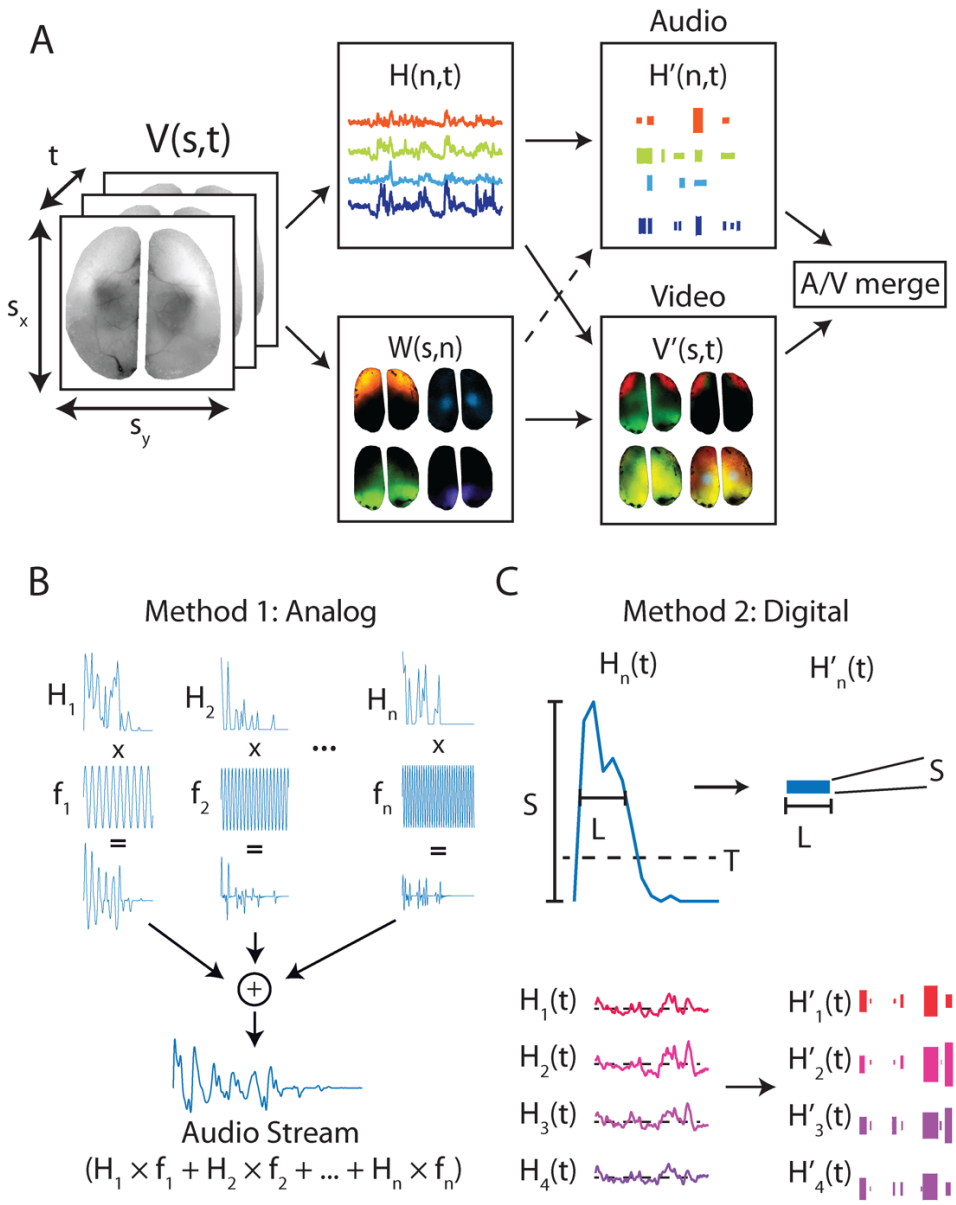

Figure 19 - The audiovisualization process for a generalized dataset. A) The dataset V(s,t) is represented as n temporal (H(n,t)) and spatial (W(s,n)) components, which are then used to create both an audible representation and a color-based remixed visualization of the dataset respectively. Datasets can be 3D or 4D, but a 3D WFOM dataset is used for this illustration. B) Audio generation method 1 (analog). Basis timecourses modulate static tones (either sinusoids or software instrument sounds), and are played simultaneously, producing an audio stream. C) Audio generation method 2 (digital). Basis timecourses are converted to MIDI note events that can be rendered as musical instruments. Here, each event is defined as a portion of the timecourses that exceeds threshold T, with length L. The strength of the note S is the peak amplitude of the note within the window L.

As explained previously, the goal is to represent the data as a linear combination of N temporal H(n,*t*) and spatial W(s,n) components assuming that the data can be represented as:

$$V(s,t) \approx W(s,n) \times H(n,t) \tag{3.1}$$

Videos are then generated by combining W(s,n) and H(n,t) using color-based remixing based on an n x 3 color map C. At each time-point T, the image corresponds to:

$$V'(s,t) \approx W(s,n) \times diag\big(H(n,t)\big) \times C_n \tag{3.2}$$

Here, V' is a color-coded representation of V, and C_n is a three-element vector corresponding to an RGB color.

Audio-streams are generated from the temporal components H(n,t) either by directly modulating pure waveforms based on signal amplitude ('analog' method, Figure 19B), or by converting time-courses to MIDI messages for increased control over note parametrization ('digital' method, Figure 12C). The pitch of the note assigned to each component n can be chosen based on some property of the data, such as the spatial position of each component in W(s,n).

The final step is to merge synchronized audio and video streams into a combined movie. This can be done using an open-source tool such as ffmpeg ("FFmpeg README," 2022), or various free and paid video editors such as iMovie (Mac) or Vegas (Windows). However, all of these basic functions can be performed within our open-source Pyanthem software package as described further in Appendix 1. A summary of the analysis and preprocessing techniques for each example shown below is detailed in Table 1.

3.3 Audiovisualization of neural activity in the mouse cortex, awake vs. ketamine/xylazine anesthesia

As a simple example, I started with an audiovisualization of a dynamic 2D dataset in which raw neural activity recordings in WFOM are spatiotemporally unmixed and then represented as time-varying pitches and color-coded components. Dynamic images of neural activity over the dorsal surface of the living mouse brain were acquired using wide field optical mapping (WFOM) through thinned skull in a Thy1-GCaMP6f mouse (Chen et al., 2012). The behavioral and optical setup were similar to the one described in Chapter 2 (Figure 9). Data were pre-processed to remove hemodynamic contamination of GCaMP fluorescence using techniques described in Chapter 2.

This dataset was acquired as part of an exploratory study to assess the effects of anesthetics on resting state neural activity in the mouse brain. The mouse was initially imaged awake and head-fixed on a freely moving wheel to record awake resting state data. The animal was then removed from the imaging rig and an anesthetic dose of Ketamine/xylazine (115 mg/kg Ketamine, 11.5 mg/kg Xylazine) was injected intraperitoneally (Mulder and Mulder, 1979). After the animal was fully anesthetized, it was again head-fixed and imaging data were acquired.

3.3.1 Dimensionality reduction

To estimate the primary temporal components of the data in an unsupervised manner, bilateral GCaMP data from the awake experiment was k-means clustered into 18 components via correlation distance measure. These clusters were then ordered according to their centroid position from the front to the back of the brain, and each component was assigned colors from the jet color map (Figure 20B). I ensured that input data for this clustering corresponded to periods when the mouse was not running. Eighteen basis timecourses H[n,t] were then obtained

using the resulting k-means spatial clusters as regions of interest (ROIs). Nonnegative least squares fitting was then used to generate 18 spatial maps corresponding to the spatial weight of each time-course W(s,n) in each pixel of the raw dataset V(s,t) (Bro and De Jong, 1997; Saxena et al., 2020). Re-multiplying W and H using Equation 3.2 yields model data V'(s,t) that can be compared to the original data to observe information that was lost in the dimensionality-reduced linear approximation (See Supplemental Movie 2 for an example). The same eroded k-means ROIs were used to extract basis time-courses from the ketamine/xylazine-anesthetized dataset, and then nonnegative least squares was used to generate that dataset's corresponding spatial components and linear representation.

3.3.2 Video stream generation

Using the color assignments shown in Figure 20, spatial components W and temporal components H were multiplied and remixed to create dynamic color visualizations of neural activity. To clearly show periods of increased neural activity, all values below zero are represented as black in movies, so careful selection of this baseline is needed if significant decreases are present (here, the baseline chosen was the mean of the interval used to calculate GCaMP %ΔF/F of the k-means clusters, i.e. at rest).

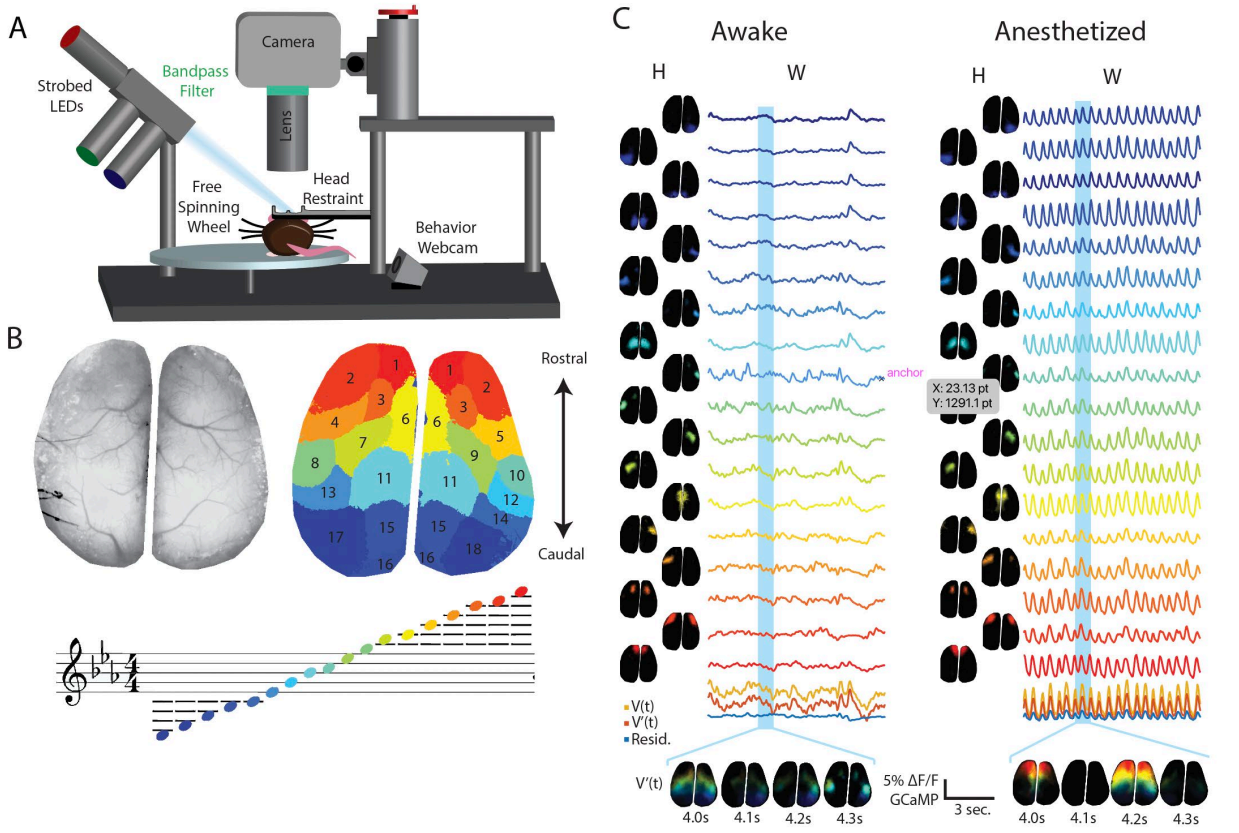

Figure 20 Simple audiovisualization of wide field neural activity in awake vs. anesthetized mouse. A) Schematic of WFOM setup. B) Wide field image showing dorsal cortex of the thinned-skull mouse (left), k-means clustering output of neural activity (right), and note assignment for each k-means cluster (bottom). This k-means output was used to obtain the basis timecourses for both awake and anesthetized datasets. C) Timecourses obtained from ROIs defined by clustering in B are used to derive spatial components using Nonnegative Least Squares (nonnegative least squares) fitting to each pixel's timecourse. The basis timecourses are then used to create an audio stream. Plots at the bottom show the average original-data timeseries (V(t), yellow) compared to the linear model (V′(t), orange), and the residual V(t)-V′(t) is plotted below it in blue. (see **Supplemental Movie 3** and **Supplemental Movie 4** for audiovisualizations).

3.3.3 Analog audio stream generation

H(n,t) was used to create an audio stream by multiplying each temporal component with a unique audio frequency sinusoid and then summing all of the components together (Figure 20B). The note pitches chosen were an ascending $C^{min}7$ chord (C, E♭, G, and B♭, spanning 5 octaves across 18 components), ordered according to the centroid position of the W components

ascending from back to front of the brain. Figure 20B shows the ordering of the 18 components and the corresponding musical note assigned to each. I note that it is important not to simply use arbitrary integer values for note frequencies, and to instead use natural note frequencies from the chromatic 12-tone scale to improve listenability. Finally, the audio stream was added as a soundtrack to the neural data spatial component video V'(s,t,c).

3.3.4 Effects of anesthesia on brain dynamics

Supplemental Movie 3 and Supplemental Movie 4 show the outputs from the above analysis on a mouse before and after induction of ketamine/xylazine anesthesia respectively. As can be appreciated from these representations, the awake brain exhibits a variety of different activation patterns, typical of resting state datasets previously reported (Ying Ma et al., 2016), whereas ketamine/xylazine anesthesia resulted in a dramatic, repetitive rostro caudal wave of neural activity. This pattern is consistent with prior reports of slow wave neural dynamics under ketamine (Pal et al., 2017; Sheroziya and Timofeev, 2014; Steriade et al., 1993). Audiovisual representations of this activity reveal a consistent rhythmic pattern from high to low notes, and yet it is also possible to perceive that each wave is not completely unidirectional, as some waves retrace forwards or originate in peripheral components.

3.4 Experiment 2 - SCAPE microscopy of apical dendrites of layer 5 neurons in awake mouse brain

Audiovisualization can also be applied to microscopy data. In the following example, I utilize real-time 3D SCAPE microscopy data capturing spontaneous calcium events in apical dendrites of neurons in the awake mouse somatosensory cortex. SCAPE microscopy is a single-objective high-speed 3D volumetric light sheet imaging technique capable of imaging cellular-level neuronal activity in awake behaving mice at both high spatial and temporal resolution

(Bouchard et al., 2015; Voleti et al., 2019) (Figure 3A-B). By converting neuronal events to a midi format, I enable use of a piano VST (Virtual Software Technology). I also used timing features of the data to choose note assignments.

3.4.1 Animal Preparation.

Layer 5 cortical neurons in the adult C57BL mouse barrel cortex were labelled with GCaMP6f via viral injection (AAV9.Syn.GCaMP6f) such that apical dendrites reaching up to cortical layers 1-3 were sparsely expressing the fluorescent calcium indicator. The mouse was implanted with a glass cranial window (dura removed) and a head plate holder was affixed to the skull to enable head-fixed, awake imaging.

3.4.2 Imaging.

SCAPE data with 488 nm (blue) excitation was acquired for a 60-second trial at 9.4 volumes per second. The size of the imaging volume was 374 x 1032 x 174 microns with a voxel size of 2.5 x 1.27 x 1.17 microns (x-y-z)[1,24]. Image acquisition and preprocessing was carried out in MATLAB using a custom acquisition GUI and customized preprocessing code.

3.4.3 4D dimensionality reduction and video stream generation

The SCAPE dataset $V(s_x,s_y,s_z,t)$ was reduced to 43 spatial (W) and temporal (H) components (Figure 21C). In this case, the unmixed spatial components W(i,j,k,n) are 3-dimensional in space. After background subtraction and detrending, each voxel's time series $V(s_x,s_y,s_z,t_{1\text{-}n})$ was checked for values that exceeded a z-score of 4. If more than 5% of the values in a voxel exceeded this threshold over the full time-series it was passed to the next clustering step, otherwise it was removed. The remaining dataset was then clustered into 85 components using K-means clustering. These basis time courses were then used to create spatial maps using nonnegative least squares. These 85 components were then manually pruned down to 43

components by removing those that did not show well-defined morphologies in their spatial maps. Finally, each 3D spatial component was median filtered (3x3x3 voxel filter) spatially to improve image quality and reduce background noise. Components were color-coded according to the component's centroid in the lateral dimension. Results are shown as 3-view maximum intensity projections (MIPs) in Supplemental Movie 5, as well as a 3D representation in Supplemental Movie 6. Additionally, each of the 43 spatial components are shown in Figure 22.

3.4.4 Digital audio stream generation using MIDI encoding

To improve both the ease of listening and clarity of the audio stream compared to experiment 1, instead of simply summing sinusoids and varying their volume, here I encoded neural activity as a piano note. The percussive nature of a piano strike (fast onset followed by slow decay) allows the listener to easily hear the complexity of multiple event onsets while still perceiving the duration of each event.

To convert extracted time-courses H(n,t) into musical notes, distinct neural events need to be identified and represented by their magnitude, time of onset and duration of activity. For microscopy data in which events clearly emerge from a dark background, event identification is possible with a simple threshold, although care should be taken not to set the threshold too low, to avoid grouping multiple events into one sustained note. All events are then represented based on their peak amplitude, onset and duration (Figure 19C), such that small, weaker events are present but audibly scaled to match their magnitude. This digitization can then easily be converted into the MIDI message format in which each note is assigned a; note on (sec), note off (sec), note strength (ranging from 0 to 127), chromatic key choice (0 to 127, with 60 as middle C, or C3), and instrument (here, I used piano). This format can be converted into music using

any VST, including Garage Band or REAPER, and is performed automatically in Pyanthem (see Appendix 1).

In this example, rather than using note pitch to encode spatial position (as in experiment 1), I chose to sort components by the timing of their first event (Figure 21D). This means that notes increase in pitch over time, but will gradually become more mixed as the same neuron fires a second, third or fourth time during the trial.

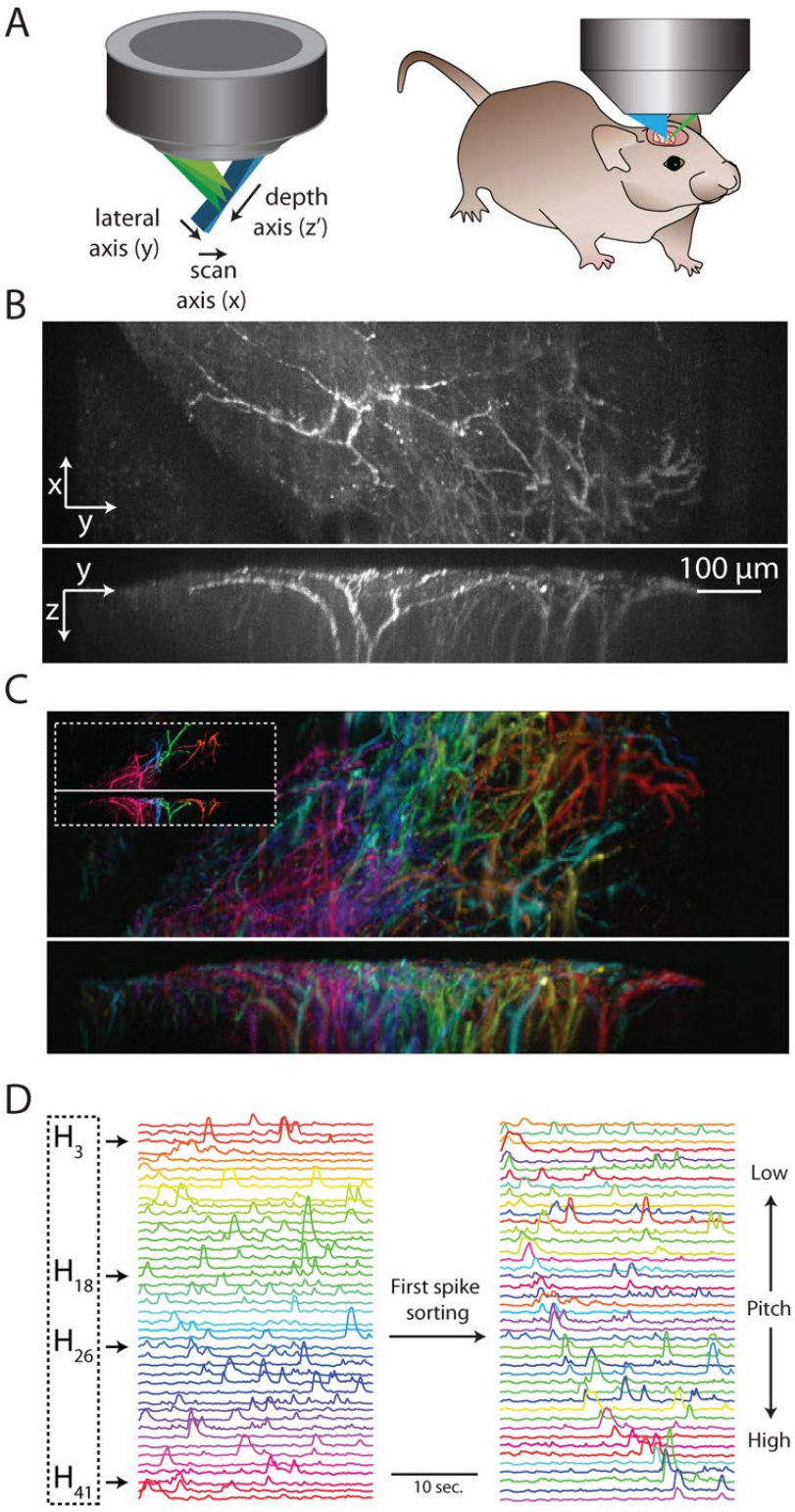

Figure 21 - Audiovisualization of a 4D SCAPE microscopy dataset. A-B) Diagrams of SCAPE objective and mouse placement. C) Maximum Intensity Projections (MIP), top and side view of one time-point in the raw dataset during a dendritic firing event. D) Basis timecourses

(H), arranged spatially on the left, and then arranged in order of first spike, with the original spatial color assignments kept. Audible note frequency follows the spike ordered components on the right, rather than the spatially arranged components on the left. E) MIP of top and side projection of all 43 spatial components after unmixing, color coded spatially from right (red) to left (pink). Inset shows four example components, which are also highlighted below in D. See Figure 22 for individual images of all spatial components. See **Supplemental Movie 5** and **Supplemental Movie 6** for audiovisualization.

3.4.5 Audiovisualization of SCAPE microscopy of mouse dendritic activity

The resulting audiovisualization is shown in Supplemental Movie 5. Ordering notes according to event timing gives a unique perspective on the relative timing and frequency of firing events of each neuron. I note that labeling of neurons in this case was sparse, and therefore does not represent the full activity of the somatosensory region. However, this representation permits assessment of the firing properties of single neurons that could be readily compared to real-time behavioral recordings, presentation of stimuli or the performance of tasks.

We also note that this analysis sought a deliberately low-dimensional representation of this data, which clustered similar time-courses together to yield groups of well-correlated pixels that belong to a dendritic tree, and differ sufficiently from other pixels over time to differentiate them from another dendritic tree. This low dimensionality removed higher order spatiotemporal noise in the dataset, but also did not seek to discover subtler differences in the timing of activity patterns along each dendrite or that may have differed within a dendritic tree from one event to the next.

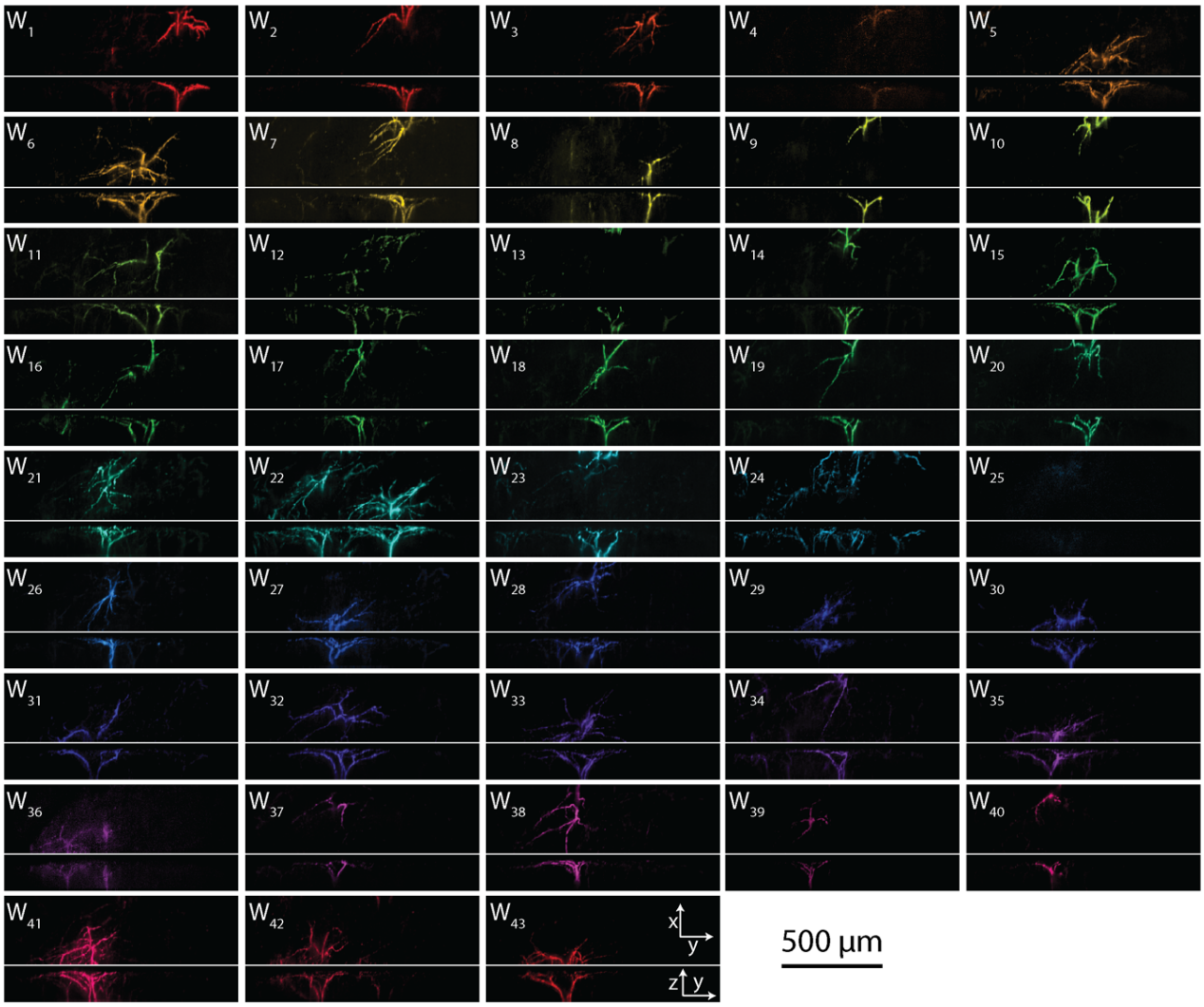

Figure 22 - All spatial components of dendrites extracted from 4D SCAPE microscopy dataset. Each panel shows top and side maximum intensity projections (MIPs) of spatial (W) components. Color was chosen from the HSV color map, and assigned based on y position.

3.5 Neural and Hemodynamic recordings in the awake, behaving mouse

Here I demonstrate a full pipeline in which WFOM data of both neural activity and hemodynamics across the dorsal surface of an awake mouse are represented simultaneously by two different musical instruments, rendered in parallel with a video stream of behavioral recordings.

3.5.1 Data acquisition

Simultaneous WFOM hemodynamic and neural data were acquired in a head-fixed awake Thy1-GCaMP6f mouse with an implanted thinned-skull cranial window (equivalent to experiment 1). During imaging, the mouse was able to run on a horizontal wheel, and behavioral videos were acquired using two PS3 Eye webcams (focused on the body and pupil), illuminated with infrared light (Figure 23A). WFOM data were acquired with GCaMP6f fluorescence images interspersed with red and green reflectance data that can be converted into hemodynamic maps that depict changes in oxy-, deoxy- and total hemoglobin concentrations as well as vessel dilation dynamics, although only Total Hemoglobin (HbT) and corrected-GCaMP data are used in the audiovisualization. GCaMP fluorescence was corrected for hemodynamic contamination as detailed in the Materials and Methods section. The imaging frame rate was 10.4 Hz for each variable.

3.5.2 Dimensionality reduction and video stream generation

The same approach as in experiment 1 was used to reduce the collected neural data into 12 components (k-means clustering, followed by nonnegative least squares to extract spatial maps W). The same eroded ROIs, defined by the neural data were then also used to obtain basis timecourses for the hemodynamic data, followed by nonnegative least squares to extract the hemodynamic W. Color remixing was used to create movies of both hemodynamic and neural datasets in the same way as experiment 1. Colors were chosen from a jet color map, and assigned from the front (red) to the back (blue) of the dorsal surface of the brain (Figure 23C) in an identical way for both neural and hemodynamic components. A composite movie was generated that includes behavioral and pupil data, after temporal synchronization between all of the video streams.

3.5.3 Combined analog and digital audio stream generation

The audio stream was generated using the analog method (Figure 19B) for hemodynamic activity and the digital method (Figure 19C) for neural activity. The neural data were encoded as piano notes, while the slower, more continuous nature of hemodynamic fluctuations were encoded as violin. These two instruments provide a clear audible difference in the two dynamic datasets, despite their simultaneity. A $C^{min}7$ chord was again used for both data streams, with notes ascending from the back (rostral) to the front (caudal) of the brain. It should be noted that all audible sounds represented positive signals, which are dependent on the chosen baseline. Thus, it was important for this audiovisualization to select a baseline that was during a relatively quiet period of activity to avoid losing sub-threshold events.

3.5.4 Audiovisualization of neurovascular dynamics during spontaneous behavior

Supplemental Movie 7 shows four simultaneous video streams – behavioral, pupil, neural and hemodynamic measures of the awake behaving mouse. First, it is easily observed that sharp increases in neural activity, represented by the piano notes, are typically followed by slower matching hemodynamic chords, consistent with the properties of neurovascular coupling in the brain acting as a delayed spatiotemporal low pass filter of neural activity (Hillman, 2014). The behavior of the mouse is also clearly depicted in the audiovisualization of brain data. Onsets of running are striking events including significant activation of hindpaw regions, with hemodynamics of the region following behind. However, differences in the sequence of neural activation for different running bouts can also be discerned. At 15 seconds, the mouse begins grooming, and these finer movements are well represented by short, quiet notes that represent activation of forepaw somatosensory and motor regions. Activation of the bilateral visual cortex

is seen at the start of the run when the WFOM illumination LEDs first turn on (see Supplemental Figure 2 for an anatomical map of functional regions of the mouse cortex).

Choosing a suitable baseline and thresholds is particularly important for audiovisualization of datasets that are more smoothly varying over time. If a chosen baseline is too high or low, important audio events may not reach threshold, or may be saturated and difficult to distinguish from one another. The baseline of basis time-courses should always be inspected, and should generally be chosen from a period of relative quiescence. Data can also be filtered or detrended (as in experiment 2) or represented on a non-linear or logarithmic scale to emphasize specific data differentials where appropriate. Where signal decreases below baseline are of particular interest, they could be represented as an additional sound or instrument, and could be represented as grayscale or an additional color in spatial representations.

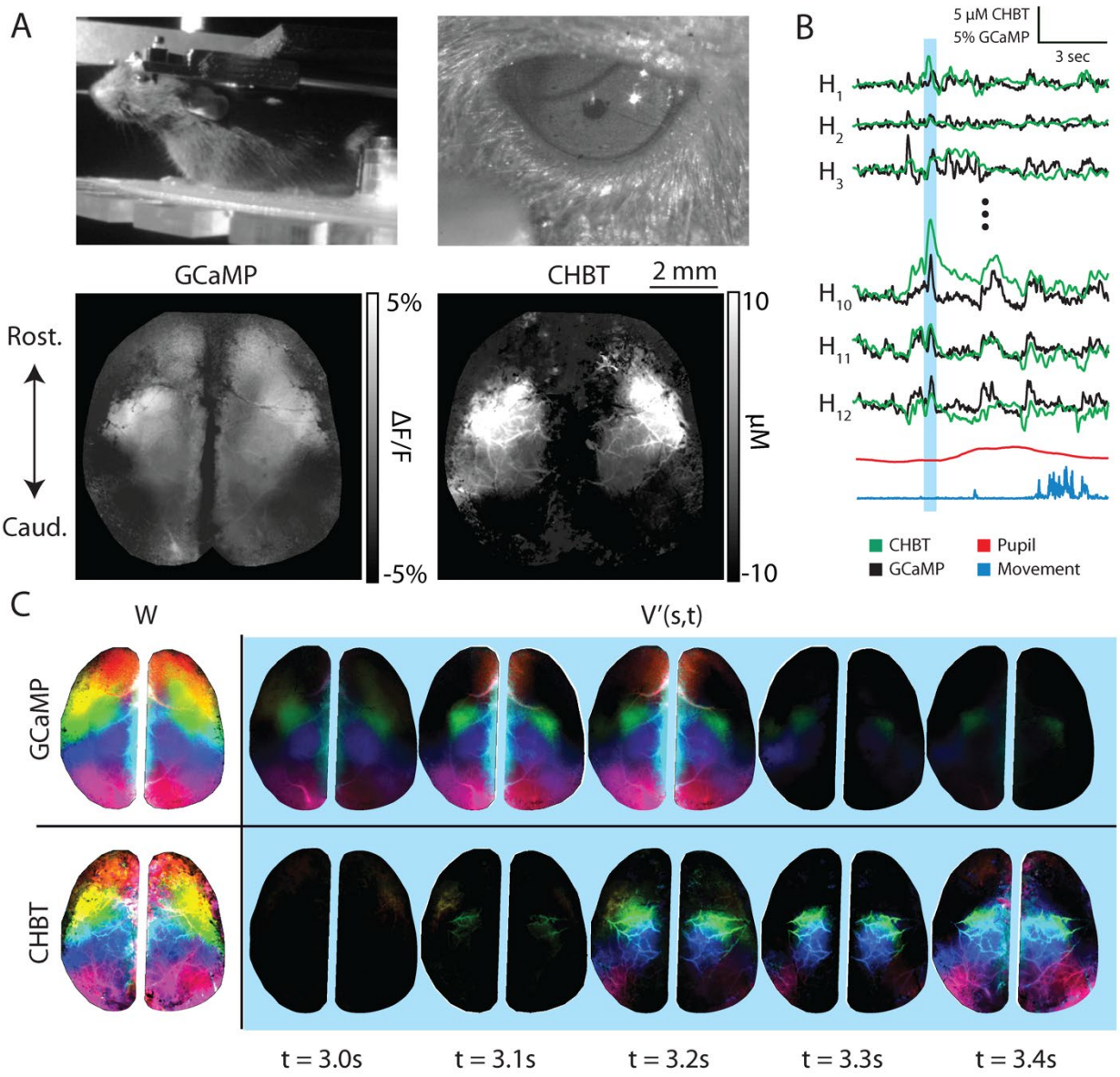

Figure 23 - Audiovisualization of both neural and hemodynamic WFOM data with simultaneous behavior in an awake mouse. A) Example frames of behavioral, pupil, GCaMP and hemodynamic data. B) Plot of temporal basis timecourses, extracted using k-means clustering. C) Color mixed representation of nonnegative least squares output W, and reconstructed color mixed dataset at example timepoints from both neural (top) and hemodynamic (bottom) datastreams. The blue bar in B represents the time period of example data shown here. See **Supplemental Movie 7** for the audiovisualization.

3.6 Discussion

Here, I demonstrated the application of audiovisualization to real-time neuroimaging data for a variety of different applications. Both mesoscale and cellular-level microscopy recordings

of brain activity can be assimilated, with a different perspective offered by reducing large and complex datasets to simple, easily accessible audio streams coupled with relevant visual representations of that activity and / or simultaneously acquired variables such as behavior.

While machine learning and AI are increasingly enabling screening of large datasets for patterns and correlates, initialization of these algorithms and interpretation of their outputs can be challenging. The human auditory and visual systems are incredibly sophisticated, and are able to hear and see patterns and features that exceed the current ability of computers. Our senses can remember, integrate over time, detect patterns, selectively amplify and focus on features independent of their amplitude, and interpret parallel streams of multisensory information. Here, one can leverage this human ability to enable assimilation of many variables in parallel by merging diverse experimental variables into interpretable representations that fill a much larger portion of our sensory space than classical observations of grayscale data.

Although I do not suggest that audiovisualization be the first step to screen through banks of large data, I have found this technique to be valuable to gain perceptions of features of data in different conditions. I used this information to guide subsequent quantitative extraction of features for hypothesis testing relating to rhythms, motifs, abnormal activity and behavioral representations in both neural and hemodynamic data.

This approach can be applied to a variety of dynamic data streams including fMRI, other functional microscopy datasets, and even far beyond analysis of just brain activity. I note that additional perception can be achieved if data is looped, sped up or slowed down to different degrees, depending on the data type. Aspects of animal behavior such as movement, pupil size, heart rate, and other vital signals can also be incorporated into audiovisualization depending on the needs of the application. For example, pupil area and movement (shown in Figure 4B) could

also be included as an audible signal, in addition to other behavioral measures, such as heart rate or fine motor movements. Percussion instruments or other discernable types of sound could also be incorporated.

One further aspect of this work is the demonstration that real-time neural and hemodynamic activity in the brain actually has similar patterns and rhythms to composed music. I intuit that this music-like nature of whole-brain activity could perhaps relate to the timing patterns of our own brain's activity and perhaps our brain's state-dependent preferences for different rhythms and patterns of music.

3.6.1 Quantifying the benefit of audiovisualization

One important question that is not addressed in this work is determining and quantifying the potential benefit that audiovisualization may provide to those interested in harnessing it. Two key user groups have been identified, and could be surveyed to assess these potential benefits. Group 1 are researchers who are visually impaired, and have a need to analyze dynamic datasets without the use of vision. Group 2 are researchers who are analyzing highly complex, real-time datasets similar to those collected and analyzed in this thesis work, and are interested in improving interpretability of their data.

For both groups, the benefit of this approach could be assessed in one yes/no question: "Do you feel that audiovisualization increases the interpretability of your dataset?". The efficacy of this approach could be quantified by the ratio of yes/no responses, or on a sliding numerical scale. Due to time and resource constraints, such an evaluation was not carried out, but would be beneficial in the future to better understand the value of audiovisualization as a tool to increase data interpretability.

3.7 Refined clustering of neural activity

So far, it has been demonstrated that k-means clustering, combined with carefully considered reconstruction techniques is a valid approach for defining key brain regions to assess Functional Connectivity. To further enhance this approach, I developed a systematic process for defining region boundaries in each subject that could be used to compare and contrast Functional Connectivity in an intuitive manner.

3.7.1 New Genetically Encoded Calcium Indicator for neural activity measurements

It was observed in preliminary experiments that a new transgenic mouse line Thy1-jRGECO1a exhibited more robust fluorescence activity, both in the dynamic range of fluorescent events and in the clarity of image sequences when viewed as a movie. In general, neural timecourses from previously imaged Thy1-GCAMP6f mice during epochs displayed a fluorescence range of ±5% ΔF/F. It was also observed that this neural activity could be reliably clustered into a dozen or so independent parcellations, which had some degree of agreement with functional maps of the cortex.

Thy1-jRGECO1a datasets exhibited a significant improvement in the dynamic range and noise properties of resting state neural activity, with fluorescence values reaching ±10% ΔF/F. Viewing movies of these datasets also showed much more punctate activity when compared to GCaMP datasets, leading us to consider Thy1-jRGECO1a as a superior transgenic mouse line for imaging of neural activity. It was also observed that resting state neural activity jRGECO1a datasets could be clustered into significantly higher component numbers with a high degree of cluster cohesiveness to Thy1-GCaMP6f component maps. For these reasons, I opted to switch transgenic lines in order to better probe the underpinnings of RSFC in the mouse.

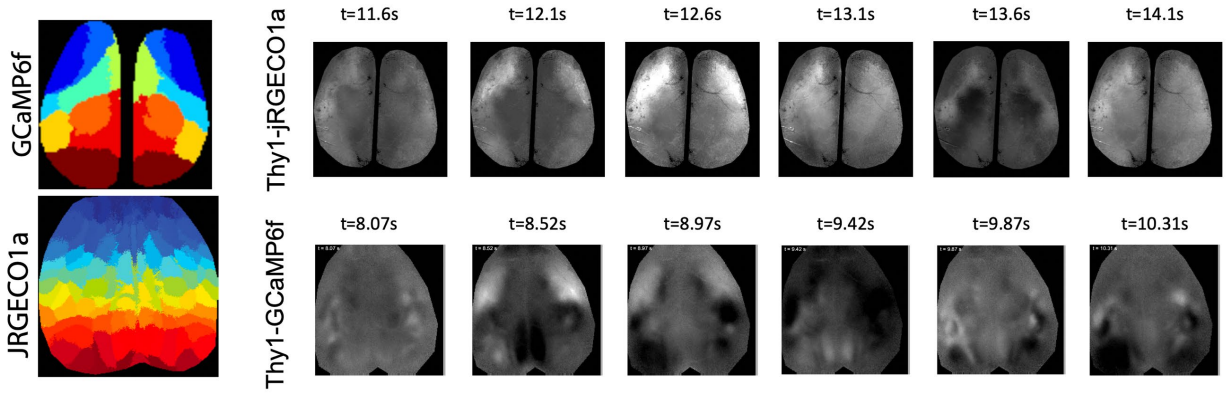

Figure 24 – Comparison of GCaMP6f and jRGECO1a imaging datasets. (Left) k-means clustered outputs for each dataset (Right) raw images of each dataset, highlighting the increased detail present in jRGECO1a datasets.

3.7.2 High order clustering in jRGECO1a transgenic mice

Based on these observations, I determined that Thy1-jRGECO1a mice were a good candidate for assessing Functional Connectivity measures, due to their enhanced signal clarity and superior detail when clustering at higher orders compared to Thy1-GCAMP6f mice. It is necessary to first establish an appropriate range of cluster order K that preserves a majority of the variance in the raw data.

Establishing an upper and lower bound on what K is appropriate is important. While a very high K may provide a detailed mapping of the cortical surface, two problems arise when clustering at high K. First, a high K inevitably leads to a curse of dimensionality, as each cluster adds to the dimensionality of analysis. It would be much more difficult to interpret and decipher traces from 500 components than to do the same for 12 components.

A second problem arises when comparing across subjects and imaging sessions. Registration of such datasets will become increasingly difficult as K is increased. A simple fiduciary registration is difficult to apply confidently, as the imaging limitations of a 2D system allow for arbitrary positioning of both the imaging window and brain surface. Based on these concerns, I opted to impose a lower and upper bound on K in order to account for these concerns.

We utilized a nonnegative least squares approximation of V to estimate the explained variance of raw neuronal datasets. First, applying nonnegative least squares to the cluster ROIs as discussed earlier allows for a reconstruction of the dataset from its decomposed H representation. By obtaining the spatial mapping W, a reconstructed dataset V can be calculated as $V = W \times H$. Then, a residual can be calculated as $V_r = V' - W \times H$. Finally, this residual (V_r) is calculated as the mean value of all residual values, and this final value can be utilized to interpret the impact of increasing K. Figure 25 illustrates an example of increasing K on a selection of 20 different datasets. As K increases, explained variance also increases asymptotically. I determined that 46 components could explain 95% of the variance, while 84 components could explain 99% of the variance when comparing 20 different epochs of neural activity. Thus, I opted to use a 46-component model, split bilaterally to compare bilateral Functional Connectivity, for a total of 92 components.

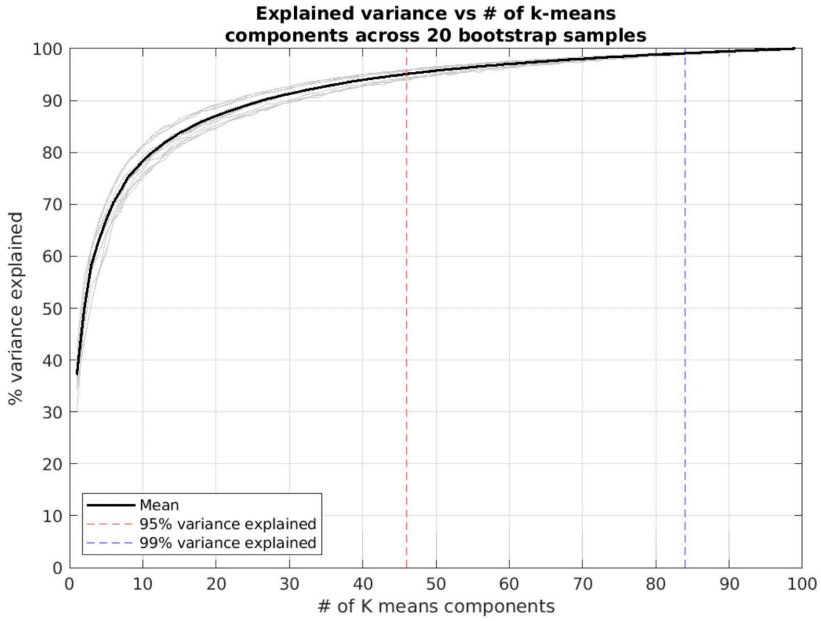

Figure 25 – Plot of explained variance (y-axis) vs. number of clusters (x-axis) in a kmeans clustering model of raw fluorescent activity from jRGECO1a dataset. Each grey line represents the trendline from a single dataset, and the black line represents the average

variance explained as the number of clusters increases. The dotted red line shows that at least 46 components can explain 95% of variance, while at least 84 components can explain 99% of variance.

3.7.3 Hierarchical clustering

Interpreting high dimensional representations of this data can be difficult, as recognizing patterns in FC maps requires a keen eye. It is advantageous then to group rows of the FC maps in a way that highlights divergences and convergences of commonly connected networks. Observing a movie of this data as well shows local organization of these smaller components, so an unordered mapping of H is not preferred.

Initially, a two-step spatial clustering was performed to accomplish this. First, the brain was clustered into K_1=6 components. Then, each component from K1 would be clustered further into K_2=10 components. Thus, the total number of components would be K_1*K_2.

After testing this approach, there were two concerns with the results. First, it was a concern that this architecture was limiting for the variable punctate nature of this data. While some regions showed broad, highly specific neuronal clusters, others exhibited much more specificity, particularly in the somatosensory regions. Since K_2 is a fixed value, it is difficult to accommodate a lower K_2 in some K_1 regions, while also providing enough components in other regions. A model like this is highly complex and susceptible to small intrasubject differences. Thus, it was elected to use a different approach for hierarchically clustering this data.

A more direct approach of hierarchical clustering is to cluster the connectivity maps after calculation. After clustering the raw dataset into k components, the temporal basis timecourses H are extracted. Then, k-means is repeated again to decompose H into 6 subgroups, so that the most similar ones are placed together. An additional step would be to apply a second ordering, where each row is ordered according to the next "nearest" row distance-wise, while keeping the

hierarchical clusters intact. This emphasizes local network connections, and highlights divergences from these default connections in a clear visual manner. Figure 26 illustrates this process, first by showing an unordered FC map (Figure 26A) then a FC map after clustering rows into 6 groups and arranging by nearness.

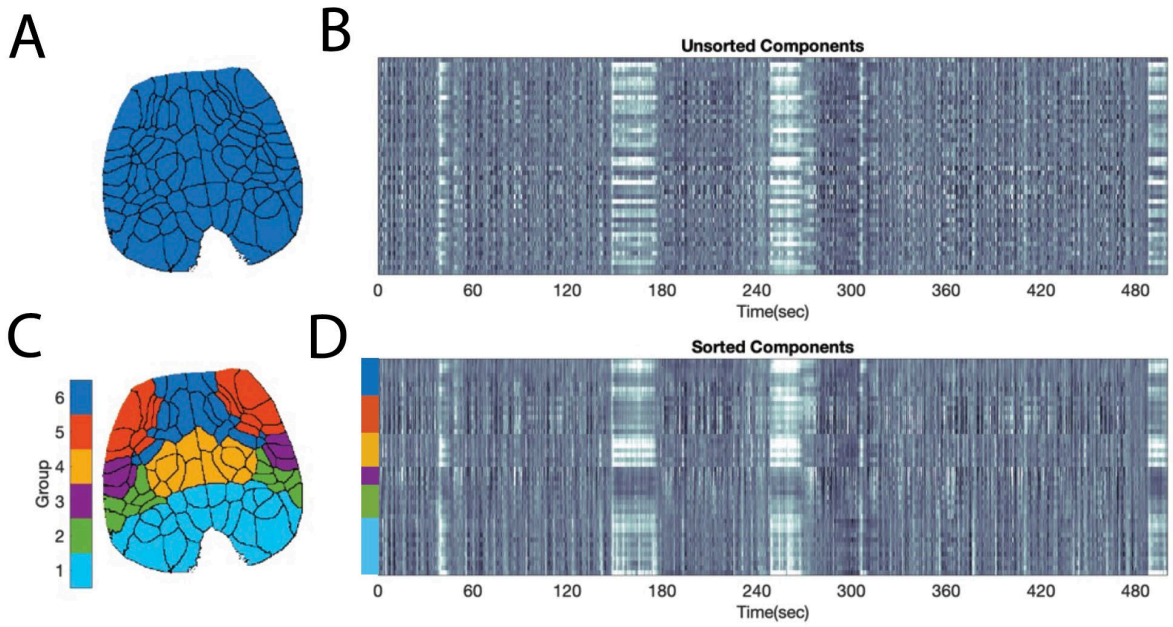

Figure 26 – Hierarchical clustering of individual ROIS into six representative groups. (A) Unordered ROI map. (B) Timecourses corresponding to unordered map in A. (C) rearranged FC components, highlighting cohesive structure of component-wise correlation values. (D) Rearranged timecourses. Colors represent each of the six component groups shown in C.

These cluster assignments are not intended to represent a "ground truth" of the FC organization, but rather one way to organize the components to enhance visual clarity and cohesiveness of Functional Connectivity mapping. However, these results reveal an anatomically recognizable topography of the cortex, indicating that the signals were coherent within local functional areas (such as whisker, hindpaw and visual sensory regions). This map was compared to an anatomical overlay from the Allen Atlas, which revealed consistent topographical similarity to previous cortical mappings (Figure 27).

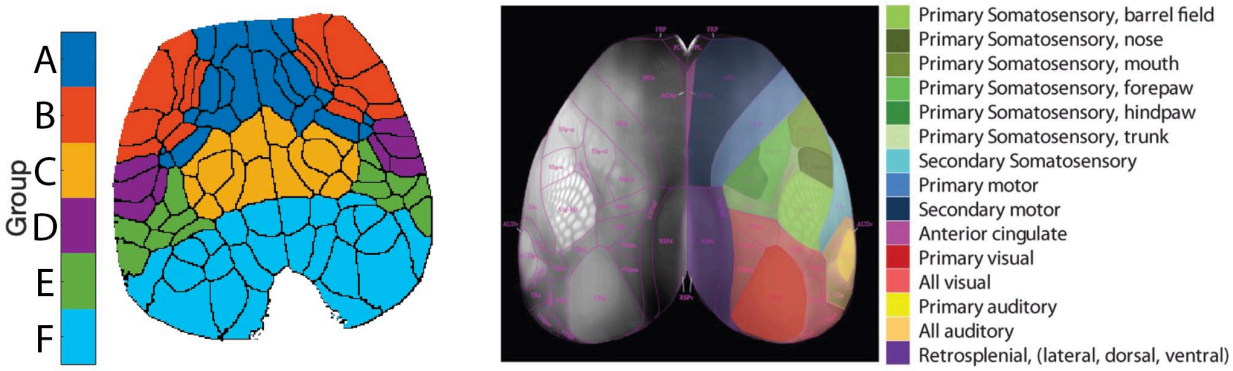

Figure 27 – Color-coded cortical functional area atlas adapted from the Allen Institute Brain Atlas. (Left) 6 Group Assignments A-F within the cortical imaging area. (Right) image of mouse cortex overlaid with Allen Atlas cortical regions.

Based on these results, one can identify each cluster group, and approximate the general anatomical region it corresponds to:

Group A (Dark blue) Is near secondary motor regions.

Group B (Orange) Overlaps secondary and primary motor regions.

Group C (Yellow) Integrates somatosensory and motor areas.

Group D (Purple) Overlaps hind paw and whisker barrel somatosensory areas.

Group E (Green) Also contains somatosensory regions, as well as auditory cortex.

Group F (Light blue) Contains a majority of the visual cortex.

3.7.4 Subject refinement through initial conditions and cluster metrics

One challenge of clustering methods such as k-means is the intrinsic property of how k-means is initialized, and how initial conditions affect the final output. While cluster assignments have generally similar structures, small inconsistencies make it difficult to assign unique identifiers to each cluster. This must be addressed to create reliable component maps for all subjects.

An additional issue lies in the bilateral cluster assignment. While some components have a bilateral morphology, others are strictly unilateral, leading to mixed assignments across hemispheres that cannot be directly compared easily without manually linking them.

To create a bilaterally matching map, I first divided along the mid-line from a user input, dividing the dataset into left and right portions D_L and D_R. Both D_L and D_R are 3D image sequences of raw neural data. D_L is then clustered into 46 regions (as determined earlier), using k-means clustering to obtain M_L. To obtain bilaterally matching components M_R from D_R, time-courses H_L are extracted from M_L. Then, k-means clustering is performed using D_R, initialized using H_L. This is done to bias assignments to be bilaterally matched between D_L and D_R. By initializing using already obtained information from the first cluster assignment, a meaningful assignment order was created for the second clustering. The resulting maps M_L and M_R are combined, producing a bilateral map M_{LR} with 46 x 2 = 92 clusters, which can be used as a representative ROI map for FC analysis.

To account for subject level differences, A refinement step is performed on a per-mouse basis, by taking M_{LR} as an initialization for each individual mouse, and performing k-means on raw neural activity obtained from that mouse. Each final map is a subject specific, bilaterally symmetric map, refined to the subject in a data driven manner, with meaningful regions that can be interpreted systematically. After acquiring maps for each of the 5 mice, a simple fiduciary registration was performed between sessions, as each session is subject to small changes in image positioning.

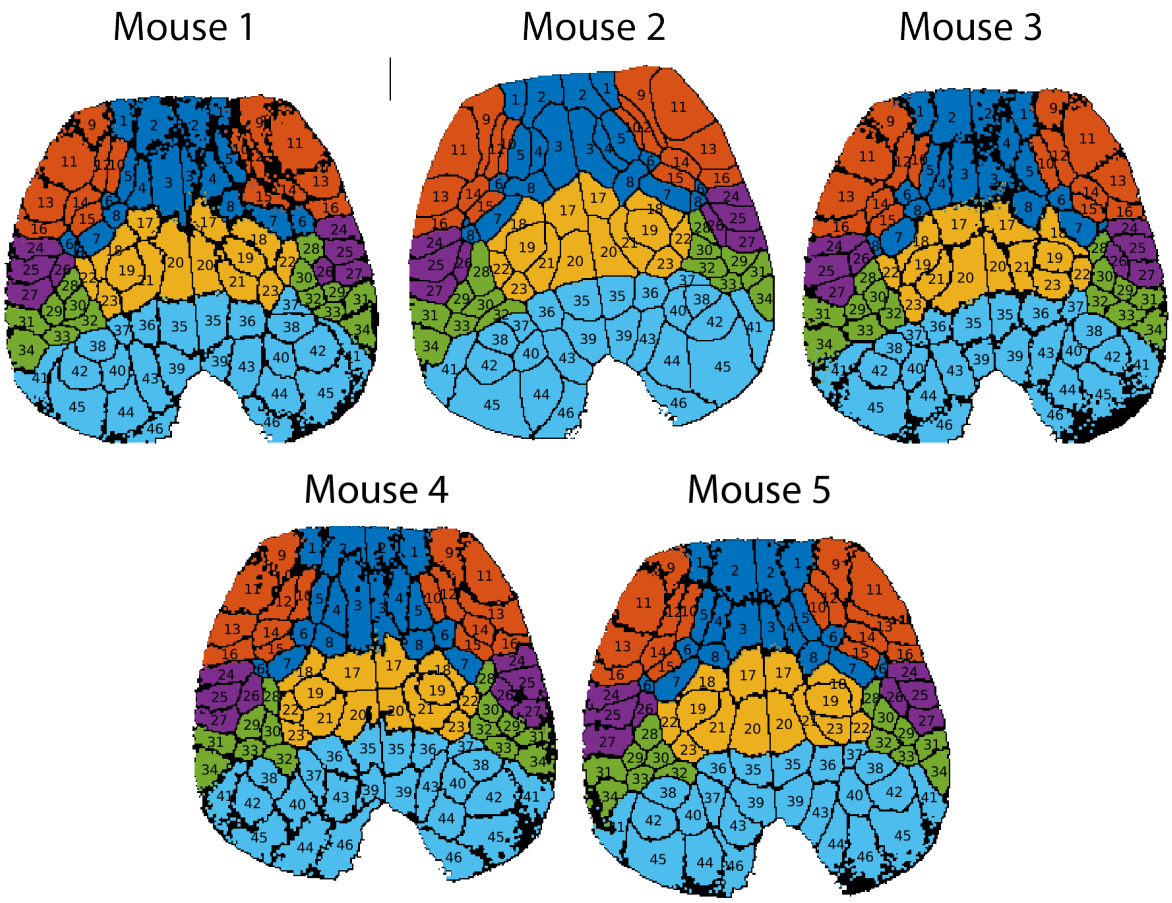

Figure 28 – Comparison of functional parcellation map in five subjects. Each map shows the 92 bilaterally matched components in each of 5 subjects. Color coded regions represent each of the six hierarchical groupings.

Figure 28 Shows the ROI maps for all five mice used in the core work of this thesis. These maps exhibit a high amount of agreement in cluster shape, size, position and arrangement when comparing across subjects. Additionally, each component has an associated contralateral pair, which provides a framework for assessing bilateral connectivity patterns in the context of Functional Connectivity analysis.

3.8 Conclusion

This chapter provided an overview for various approaches used to cluster and spatially decompose raw neural and hemodynamic recordings into meaningful representations. This was done both for the creation of audiovisualizations, as well as for a systematic process by which

one can represent these datasets for investigating Functional Connectivity. These approaches are only one solution, and are by no means a ground truth approach to operate from. However, the meaningful topographical organization of component maps into regions that agree with previous anatomical brain maps in the mouse (Figure 27) is an encouraging result, and leads us to conclude that these approaches effectively preserve the spatiotemporal properties of the raw data.

4 Chapter 4: A Behavioral Model of Dynamic Functional Connectivity

Having established that one can spatially cluster resting state neural activity in the mouse in a systematic, repeatable manner, I can now apply these techniques to a cohort of data to assess Functional Connectivity changes across the entire cortex. Our ability to simultaneously image neuronal and hemodynamic changes in real-time provides a unique opportunity to explore not just the existence of these fluctuations, but the proposed neuronal-driven hemodynamic changes that have been observed in humans. Our real time simultaneous behavioral monitoring will additionally enable us to compare measures of Functional Connectivity in different behavioral contexts, with the added ability to determine to what degree these properties may systematically persist independent of subject or imaging session.

4.1.1 Calculation of Functional Connectivity

A Functional Connectivity (FC) matrix is calculated as the row-wise correlation coefficient of K time-course pairs, with $(K^2 - 2K)/2$ unique comparisons, ignoring self-referential and redundant connections. The FC matrix of an extended period of time (5-15 minutes) is referred to as Static or Stationary Functional Connectivity (Menon and Krishnamurthy, 2019). It is advantageous to first understand the Static FC properties of cortical neural activity before progressing to time-dependent analyses.

4.2 Experimental Overview

We performed WFOM to simultaneously record ongoing large-scale neural and hemodynamic activity at 20 frames per second, longitudinally in five awake, head-fixed, behaving Thy1-jRGECO1a transgenic mice expressing a red-shifted calcium indicator in

excitatory neurons. Hemodynamic activity was imaged using green and red diffuse reflectance which was converted into changes in oxyhemoglobin (Δ[HbO]), deoxyhemoglobin (Δ[HbR]) and total hemoglobin concentration (Δ[HbT] = Δ[HbO] + Δ[HbR]). Reflectance data were also used to generate a correction for the jRGECO1a fluorescence data to account for the absorption effects of hemoglobin. The mice were free to move on a light-weight horizontal rotating, transparent acrylic wheel and were each imaged for up to six 10-minute runs within each imaging session, with imaging sessions spaced at least three days apart. See Figure 9 for an illustration of the experimental setup.

Using the technique described in Chapter 3, jRGECO1a fluorescence activity was decomposed into 92 unilaterally matching basis time-courses as described in the last chapter. Static Functional Connectivity measures were then determined by calculating the Pearson's correlation coefficient for all pairs of time-courses.

4.2.1 Behavioral monitoring

To measure changes in behavior and physiological arousal, I tracked the paw position, whisker movement and pupil diameter by extracting behavioral markers from raw webcam videos using DeepLabCut (Mathis et al., 2018), as detailed in Chapter 2. For movement/locomotion, I tracked the position of the front left and right paw, and defined movement as the average value of the frame-to-frame absolute differential in the x-y coordinate position of each paw. For whisking, I tracked three prominent whiskers on the left side of the face, and defined movement similarly to paw movements, taken as the average value of the frame-to-frame absolute differential in the x-y coordinate position of each whisker. Finally, I tracked pupil size by tracking 8 points on the pupil border. I extracted pupil diameter by

estimating the ellipse formed by these points using a least squares fitting method of the marker coordinates (Pratt, 1987).

We tracked multiple points for each behavioral variable to maximize the availability of data for analysis. While DeepLabCut is generally reliable, there are rare instances where tracking is poor, due to occlusion (i.e. one paw moves in front of the other) or framerate limitations (i.e. whisking is too fast to accurately track). DeepLabCut represents the label confidence for each marker a p value. I ignored all p values greater than 0.05, relying on the remaining markers to estimate behavior. In some instances, no markers had an adequate confidence level, such as when the mouse blinked or closed their eyes. In these instances, I set the behavioral value to NaN. An example ten-minute imaging session with behavior, raw jRGECO1a neural activity and Functional connectivity measures is shown in Figure 29.

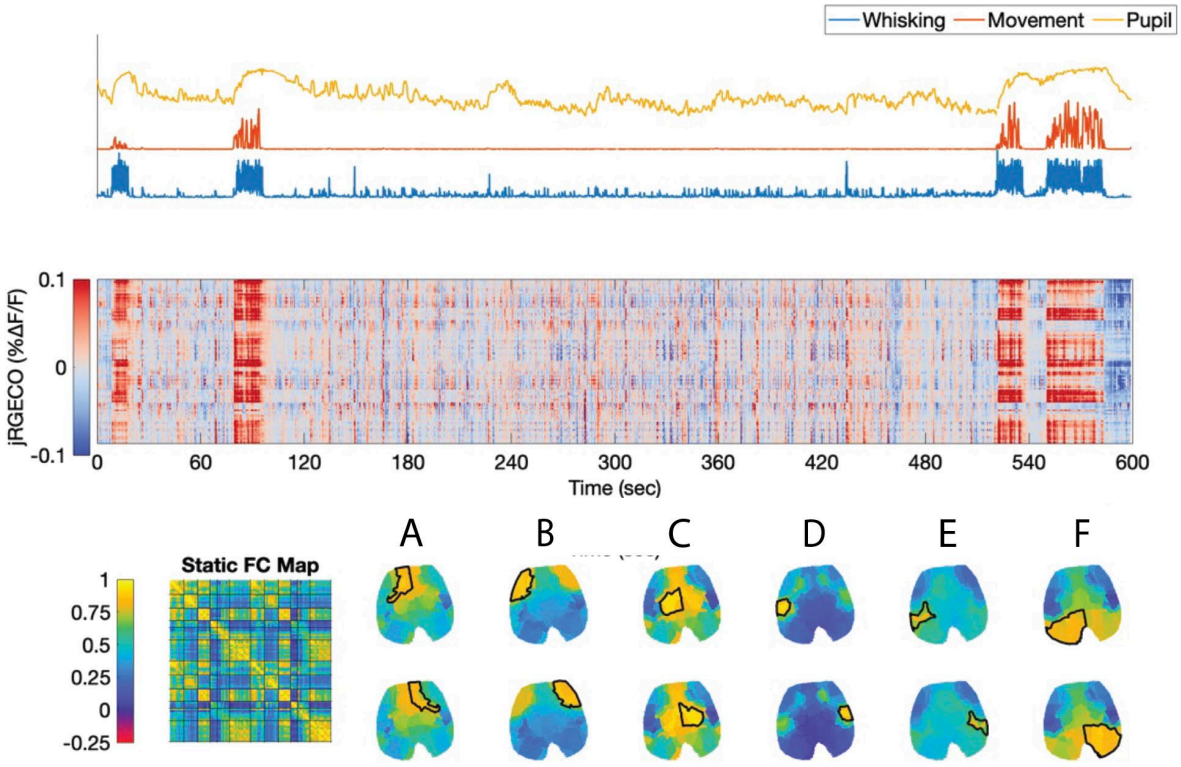

Figure 29 – Static Functional Connectivity of neural activity. (Top) Behavioral measures during a 10 minute imaging session where the mouse was allowed to freely move and rest. (Middle) Raw jRGECO1a fluorescence changes during the imaging session. (Bottom) Static Functional Connectivity map of the full imaging session. Left shows the unstructured FC matrix, and each brain map on the right illustrates the connectivity levels associated to each bordered region. Letters represent the Group defined in Figure 27.

4.2.2 Behavioral Dynamics

First, I observed that there was highly dynamic behavioral activity exhibited in the run above. Long periods of little to no movement are interspersed with short bursts of movement, often lasting approximately ten seconds. These movement epochs are accompanied with large increases in pupil diameter (yellow trace) and whisking activity (blue trace), although it should be noted that whisking activity is not exclusive to simply locomotion. Both whisking and pupil size peak and plateau during locomotion, and show a steady, consistent decrease as locomotion ceases. Pupil diameter returns to pre-locomotive levels in 30-60 seconds. During periods of non-locomotion, whisking activity exhibits a high degree of variability, with epochs of little to no whisking activity interspersed with highly variable whisking events, both in amplitude and frequency. When looking at locomotion, I see a broad increase in neural activity, indicating that locomotion engages a broad portion of cortical regions.

4.2.3 Analysis of Stationary Functional Connectivity

The stationary connectivity map during this session can be broken down by each of the six component groupings shown in the columns on the bottom of Figure 29. While all groups show relatively strong within-group connectivities (regions bounded by the black borders), each has unique FC patterns to distal brain regions. I also note the degree of bilateral connectivity, which is an important consideration to indicate coordination of separate, but functionally similar brain regions in separate hemispheres.

A. Moderately low FC with all groups. High bilateral connectivity.

B. Low FC with all other groups, particularly with visual cortex. High bilateral FC.
C. Strong FC across with Group A, low FC with Groups B and D, and moderate connectivity elsewhere. High bilateral connectivity.
D. Notable cluster of heightened FC toward in the midline-caudal direction, and low FC elsewhere. Low bilateral FC.
E. Notably low FC with frontal Groups B and D, and moderate FC elsewhere. Low bilateral FC.
F. Similar FC to Group E. Moderate bilateral FC.

4.3 Functional Connectivity changes during a single imaging session

The assumption of static connectivity across the entire imaging session is short lived, given the goal of this dissertation. Next, I assessed how these FC patterns change during different epochs. The raw neuronal data exhibited dramatic shifts during locomotion, so it is reasonable to hypothesize that FC dynamics will shift as well. At the same time, I also have the ability to link lesser behavioral dynamics to these observations. While gross changes in arousal such as locomotion may be shown to modulate FC dynamics, I can also observe the subtle shifts in arousal during resting state epochs, as well as transitionary periods in and out of locomotion. Figure 30 shows an image sequence of the first 5 minutes of the same example data acquired in Figure 29.

A comparison of FC maps within each epoch exhibits broad changes in FC moment to moment. Most notably, it is observed that epochs of locomotion are accompanied by strong positive fluctuations in the neural activity, suggesting that voluntary movement engages a broad part of the cortex in a stereotyped manner. Epoch D, a period with a portion of locomotion, also shows a relative increase in bilateral connectivity in group E (final column, see annotation in

Figure 30) indicating a synchronization of cross callosal visual regions during engaged movement.

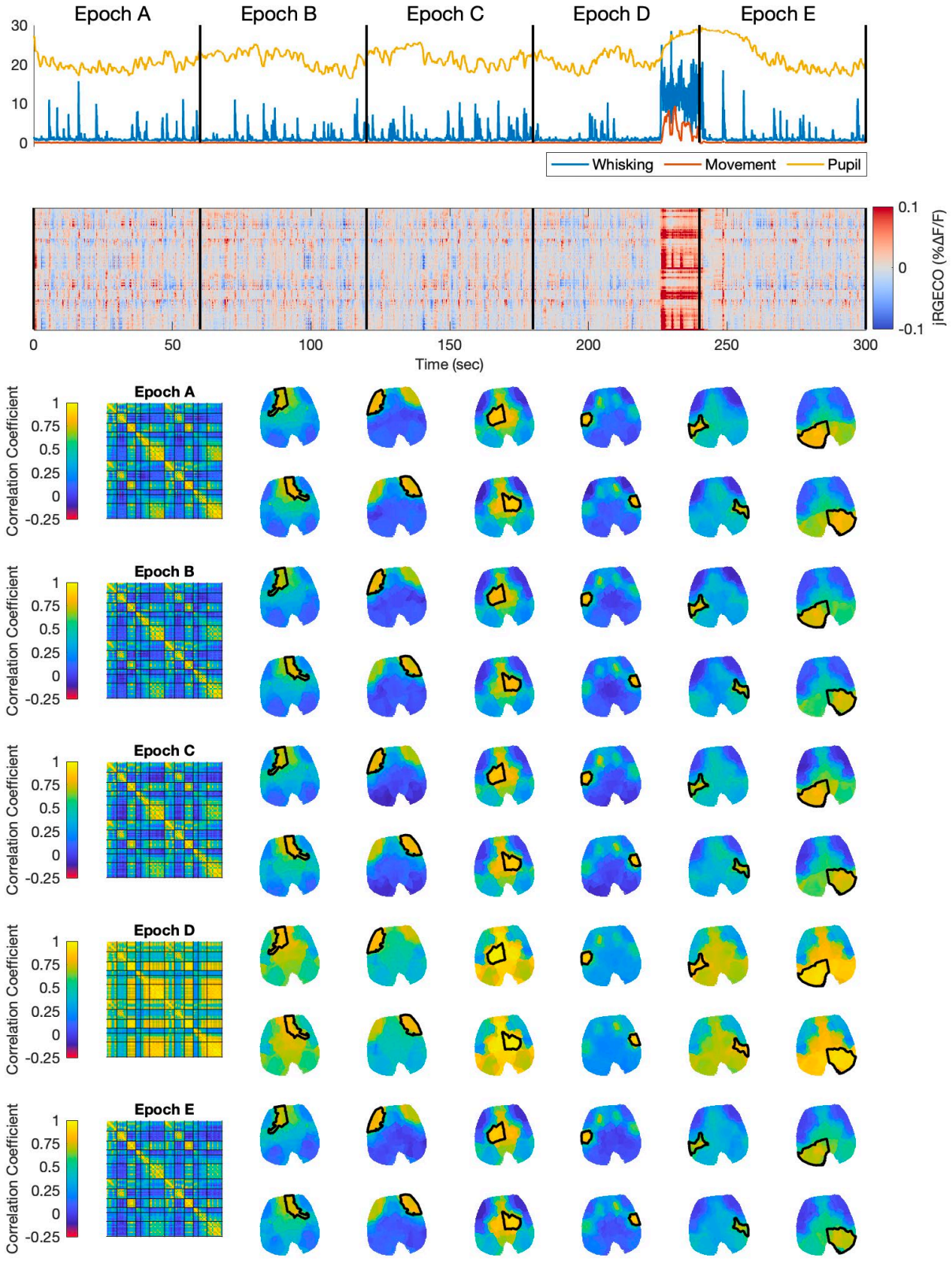
Epoch A
Epoch B
Epoch C
Epoch D
Epoch E
30
20
10
0
Whisking
Movement
Pupil
0.1
0
-0.1
jRGECO (%ΔF/F)
0
50
100
150
200
250
300
Time (sec)
Correlation Coefficient
1
0.75
0.5
0.25
0
-0.25

Figure 30 - Windowed Functional Connectivity of neural activity. (Top) Behavioral measures during a 10 minute imaging session where the mouse was allowed to freely move and rest. This session was divided into five epochs, labeled A-E. (Middle) Raw jRGECO1a fluorescence changes during the imaging session. (Bottom) FC map for each of the five epochs. Left shows the unstructured FC matrix, and each brain map on the right illustrates the connectivity levels associated to each bordered region.

4.3.1 Visualization of sliding window correlation reveals complex dynamic changes in Functional Connectivity

We next decided to utilize a sliding window to visualize FC dynamics in real time. A visualization was created (Figure 31), which shows raw neural activity, real time FC dynamics within a 2 second window, behavioral measures, and a real time webcam movie of the mouse behavior.

This visualization showcases the full range of FC dynamics. It is immediately obvious that movement is followed by dramatic positive shifts in FC values, while periods of rest lead to steady decreases in FC values, often moving into negative correlation in some regions. Based on this visualization, it was clear that FC is in a state of constant change, and that behavior was a key modulator of these changes. The next, most obvious step was then to better understand how these key behavior shifts played a role in modulation of Functional Connectivity in neural and hemodynamic activity.

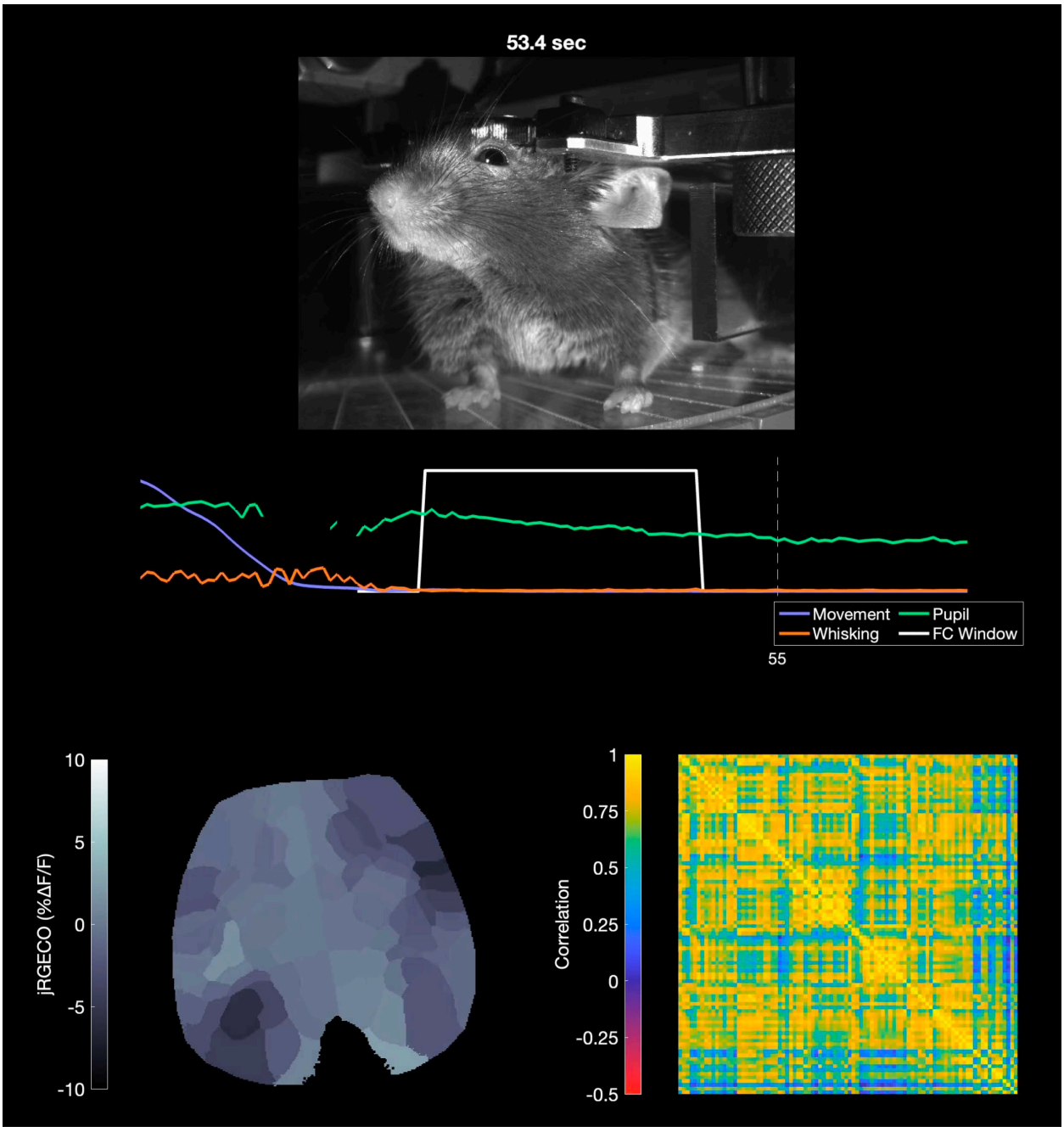

Figure 31 – Thumbnail of Supplemental Movie 1, showing sliding window FC along with raw neural data and behavior. (Top) Webcam video of mouse, captured in real time along with WFOM data. (Middle) Behavioral metrics extracted from above video using DeepLabCut (Mathis et al., 2018). Colored lines represent each behavioral metric, while the white line represents the FC window used to calculate FC metrics below. (Bottom) Left shows raw neural activity for each FC cluster projected onto the cortical window of the mouse. Right shows the calculated FC matrix within the window.

4.4 A Behavioral Model of Brain State

Note: This section is adapted from a manuscript currently under review (Shahsavarani, Somayeh et al.), of which I am a contributing author.

Based on these observations, it is clear that major events such as spontaneous running clearly alter interregional FC measures. To further understand these differences, I sought to better understand the key aspects of Functional Connectivity changes during stereotyped behavioral epochs. To this end, I identified five distinct behavioral states that all mice exhibited consistently throughout imaging sessions:

I. Sustained Locomotion State
II. Locomotion Offset State
III. Initial Resting State
IV. Sustained Resting State
V. Locomotion Onset State

These five behavioral states were used to capture Functional Connectivity maps, which could then be systematically compared to each other. Due to the timing of behavior shifts, I felt that 2 second windows were not sufficient to capture both the full range of behavioral dynamics, as well as the resulting signal changes in neural and hemodynamic activity. Thus, I chose to calculate FC maps over temporal segments of 10 seconds overlapping with each behavior of interest. For transitional states [II: Locomotion Offset] and [V: Locomotion Onset], these windows were centered to the transition. As an example, locomotion onset windows were situated to capture 5 seconds of rest followed by 5 seconds of locomotion. All other states were restricted so that the window fully contained either total rest or total locomotion. [I: Sustained Locomotion] was centered to the running epoch, [III: Initial Resting State] was the 10 seconds

immediately following locomotion offset, and [IV: Sustained Resting State] was the period from 40 to 50 seconds after locomotion offset. Figure 32A illustrates example windows for each of these states, annotated in dotted black boxes.

For each mouse, the average FC map within each behavioral window was assumed to be the representative 'brain state' associated to the mouse behavior. Figure 32B illustrates the behavior and associated brain states for one mouse. The FC maps for each behavioral state had distinct correlation patterns, while the differences between initial and sustained resting states were more subtle.

The most notable feature of the resting states was desynchrony between the anterior lateral frontal cortex (FC Group B) and the posterior brain regions. In addition, comparing the rest states with the locomotion state, I noted that the correlation patterns within the anterior lateral frontal cortex were more bilaterally symmetric during rest, whereas the visual cortex was more bilaterally symmetric during locomotion. To demonstrates how these patterns were manifested in the raw temporal signals, the average time series over five ROIs within the left and right anterior lateral frontal cortex (prefrontal cortex) and over four ROIs within the left and right visual cortex were extracted and plotted against each other. Figure 32C shows some examples of these time series across mice during the locomotion and sustained-rest states. As depicted, the time series extracted from the left and right prefrontal cortex are more synchronous during the sustained rest, whereas the visual cortex is more bilaterally synchronous during running.

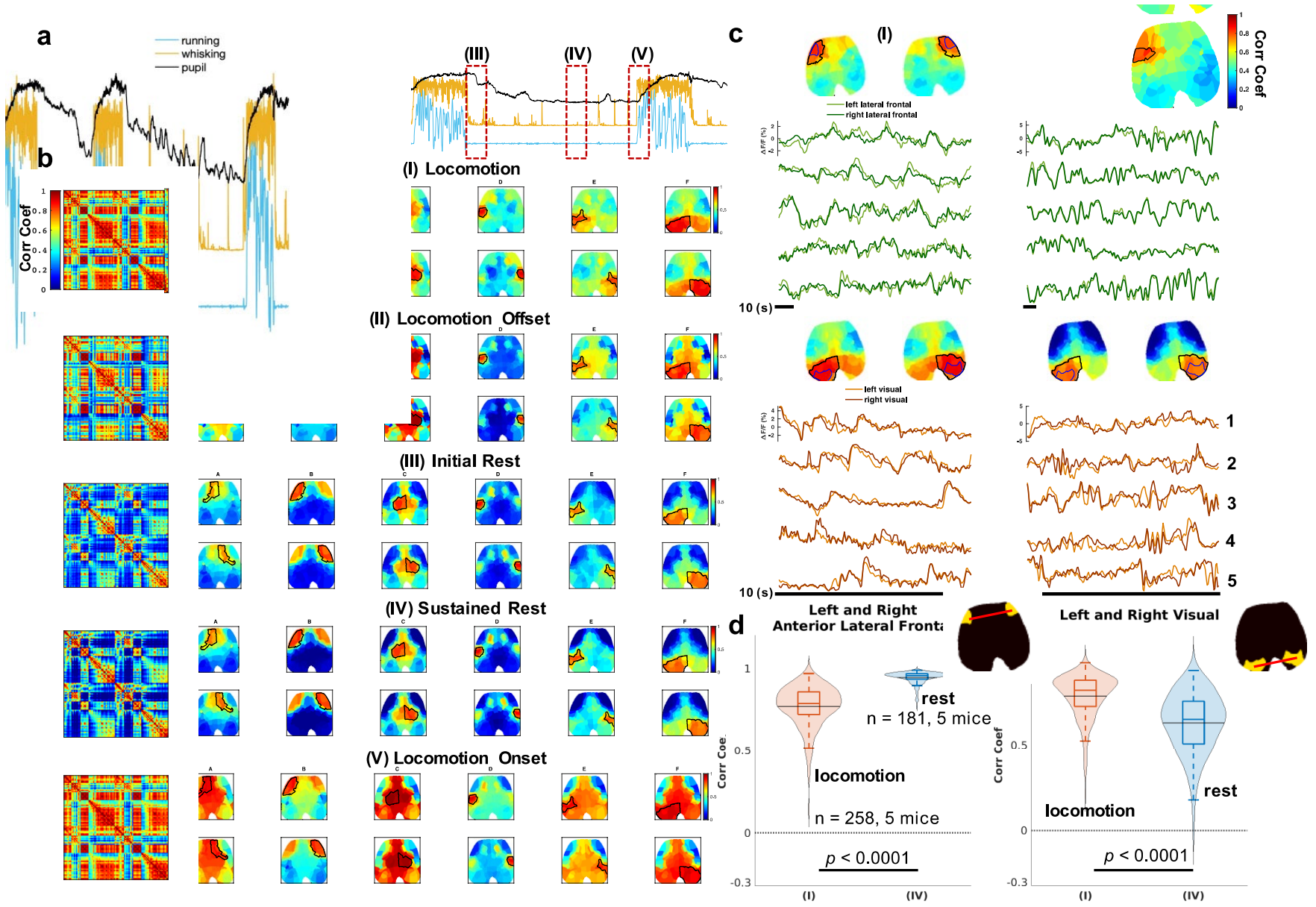
a
running
whisking
pupil
b
Corr Coef
(III)
(IV)
(V)
(I) Locomotion
(II) Locomotion Offset
(III) Initial Rest
(IV) Sustained Rest
(V) Locomotion Onset
c
(I)
left lateral frontal
right lateral frontal
10 (s)
left visual
right visual
1
2
3
4
5
d
Left and Right Anterior Lateral Fronta
Left and Right Visual
rest
n = 181, 5 mice
locomotion
n = 258, 5 mice
p < 0.0001
Corr Coef
(I)
(IV)

Figure 32 – Behavior driven brain states. A) Behavior. Signals related to locomotion, whisking, pupil radius are shown for one example of recording session. The behavioral states are marked with the red dotted lines, which are: (I) locomotion, (II) locomotion offset, (III) initial rest, (IV) sustained rest, and (V) locomotion onset. B) Brain states. The neural correlation maps corresponding to each behavioral state are given for one example mouse. Each correlation map is the average correlation maps of each behavior of interest within and across sessions. The brain maps corresponding to each brain state show the Pearson's correlation coefficients between the seed regions shown by black lines and all ROIs. Six bilateral seed regions were used for each hemisphere, resulting in 12 maps in total. C) Bilateral asymmetry between neural activity in the anterior lateral frontal cortex during locomotion (I) and in the visual cortex during sustained rest (IV). The time series are example extracted ROIs (outlined by blue lines) within the lateral frontal cortex and the visual cortex for 5 different bouts of one example mouse. During locomotion, the neural activity in the anterior lateral frontal cortex becomes more localized and unilateral, with higher relative correlation to the rest of the brain. During rest, the activity, is mostly bilaterally symmetric, clearly defined, and uncorrelated with the rest of the brain. D) Intra-regional and inter-regional correlation distributions by two states of locomotion (red) and sustained rest (blue). The temporal windows of interest across all mice (n = 258 locomotion windows, n = 181 sustained-rest windows for 5 mice) were used. Left: correlation between neural activity in the left and right anterior lateral frontal cortex. A significant increase was observed during rest ($Z = 6.19$, $p < 1e\text{-}09$). Right: correlation between neural activity in the left and right visual cortex. A significant reduction was noted during rest ($Z = -9.38$, $p < 1e\text{-}20$, Wilcoxon rank-sum test). The black lines within the violin plots indicate the mean. Boxplots are centered on the median (the orange or blue lines within the boxes) and extend to the 25th and 75th percentiles; data beyond the whiskers are considered as outliers (1.5 times the interquartile range less than the 25th or more than the 75th percentiles).

As demonstrated in the brain maps (Figure 32B), the key feature of the resting states was desynchrony between the anterior lateral frontal cortex (FC Group B) and the posterior brain regions. In addition, comparing the rest states with the locomotion state, it was noted that the correlation patterns within the anterior lateral frontal cortex were more bilaterally symmetric during rest, whereas the visual cortex was more bilaterally symmetric during locomotion. To demonstrates how these patterns were manifested in the raw temporal signals, the average time series over five ROIs within the left and right anterior lateral frontal cortex (prefrontal cortex)

and over four ROIs within the left and right visual cortex were extracted and plotted against each other. Figure 32C shows some examples of these time series across mice during the locomotion and sustained-rest states. As depicted, the time series extracted from the left and right prefrontal cortex are more synchronous during the sustained rest, whereas the visual cortex is more bilaterally synchronous during running.

To summarize the above effects, the connectivity between the anterior lateral frontal cortex (FC Group B) and the visual cortex (FC Group F) was quantified, as well as the connectivity between the left and right cortices within these regions, for every legitimate trial during locomotion vs rest. First, the Pearson's correlation coefficients were calculated between the average neural activity in the anterior lateral frontal cortex and the visual cortex (Figure 32D). It was hypothesized that the correlation between these two regions would be significantly lower during sustained rest than locomotion. Pearson's correlation coefficients were also calculated between the average neural activity in the left and right regions within both the anterior frontal cortex and the visual cortex (Figure 32D). It was hypothesized that the left and right anterior lateral frontal cortices would be more synchronized during sustained rest, whereas the visual cortex would be more bilaterally synchronized during locomotion. As expected, it was found that the synchrony between the anterior lateral frontal cortex and visual cortex was significantly lower during sustained rest ($Z = -15.43$, $p < 1e\text{-}53$, Wilcoxon rank-sum test). Also, it was noted that during rest the correlation between neural activity in the left and right anterior lateral frontal cortices significantly increased ($Z = 6.19$, $p < 1e\text{-}09$), while the bilateral synchrony within the visual cortex was also significantly reduced ($Z = -9.38$, $p < 1e\text{-}20$).

4.5 Behavioral States modeled using a least-squares regression model

We next investigated the presence of the representative brain states within individual trials by developing a model to approximate a given FC matrix as a linear decomposition of all other brain states. In doing so, every FC matrix was reconstructed as a linear combination of the FC brain states (Figure 32B) using non-negative least squares. Figure 33A shows the coefficients corresponding to each brain state, predicted by the model for one example recording session of neural activity. Qualitatively, it was observed that the estimated coefficients were in line with mouse behavior. To quantify this observation, the average coefficients were calculated by the model over the running bouts of interest (see Methods). As expected, the average coefficients changed in accordance with mice's behavior (Figure 33B). Such changes occurred gradually and continuously as the FC frames were passing through different behavioral states. These results validate the occurrence of the basis FC maps (estimated from the average correlations between the neural time series locked to a particular behavior, see Figure 32B) within the individual trials and show consistency in correlation patterns within a particular behavior. This indicates that the pre-defined basis FC maps manifest different states of the brain, the variations of which can be linked to changes in mouse behavior.

Figure 33 - Non-negative least squares regression. A) Coefficients corresponded to each basis FC matrix ('brain states') estimated by the model for one example recording session of neural activity. The upper plots depict the behavior and the average behavior within each correlation window, respectively. The correlation windows were shifted one frame at a time. The length of the window was 10 seconds. The remaining plots show the temporal evolution of the brain state coefficients predicted by the model. To assess the goodness of prediction, the relative residual was calculated as $\frac{\|(\mathbf{d}-\mathbf{cx})^2\|_1}{\|\mathbf{d}^2\|_1}$, where d is the actual correlation window, x is the brain states, and c is the coefficients (see Methods). B) Average brain state coefficients predicted by the model over the temporal windows of interest. The solid lines show the average values, and the shaded colors correspond to the standard errors. Left: running bouts were aligned with the running onset time. The dotted vertical line indicates the onset time. Middle: 10 seconds at the middle of running bouts were aligned. Right: running bouts were aligned with the running offset time. The dotted vertical line indicates the offset time.

4.5.1 Differences between resting-state correlation patterns may be explained by arousal level

A previous study reported that after locomotion, pupil size gradually decreases in mice and returns to baseline level over about 40 seconds after locomotion offset (Vinck et al., 2015). A similar trend was also observed in these animals (Figure 34A). Pupil diameter is expected to be positively coupled to alertness or arousal level (Reimer et al., 2016). Therefore, it was speculated that the initial-rest state would be associated with high arousal, while the sustained-rest state would be the representative of low arousal.

Despite the subtle differences between the initial-rest and sustained-rest FC maps (Figure 34B), the non-negative least squares model was able to identify a reciprocal relationship between their coefficients. Figure 34B illustrates this reciprocity, showing the temporal evolution of the initial-rest and sustained-rest coefficients for one example of recording sessions. Quantifying this relationship over the legitimate rest trials across all mice, the Pearson's correlation coefficients were calculated between the initial-rest and sustained-rest coefficients estimated by the model over the rest periods of at least 60-s long. Figure 34**C** depicts the distributions of these correlation values. As predicted, a strong negative correlation was found between these two coefficients (mean=-0.72, std=0.21). This indicates a back-and-forth switching behavior between the brain resting states when mice are not running. Although evident in the individual trials, the trial-averaged coefficients estimated by the non-negative least squares model failed to show this effect. One possible explanation is that the relative switching between these two states is not time-locked to the end of running after the first ~10 seconds of rest. As a results, the shifts in the resting states randomly varied across the individual trials and hence cancelled out on the average. In addition, the Pearson's correlation values were calculated between the resting-state

coefficients predicted by the non-negative least squares model and pupil diameter over the rest periods of at least 60 seconds across all mice. Figure 34D demonstrates the probability distribution of these correlation coefficients (fitting a kernel distribution). As expected, the initial rest was associated with the larger pupil size and thereby higher arousal level, whereas the sustained rest was associated with the smaller pupil size and hence lower arousal level (comparing the initial-rest and sustained-rest distributions, $k = 0.23$, $p < 1e\text{-}4$, Kolmogorov-Smirnov test). This trend held true between resting-state coefficients and whisking ($k = 0.3$, $p < 1e\text{-}7$, Kolmogorov-Smirnov test). These results show that the differential correlation patterns between the resting states can be ascribed to arousal level, and switching between the initial- and sustained-rest states can be associated with ongoing arousal fluctuations.

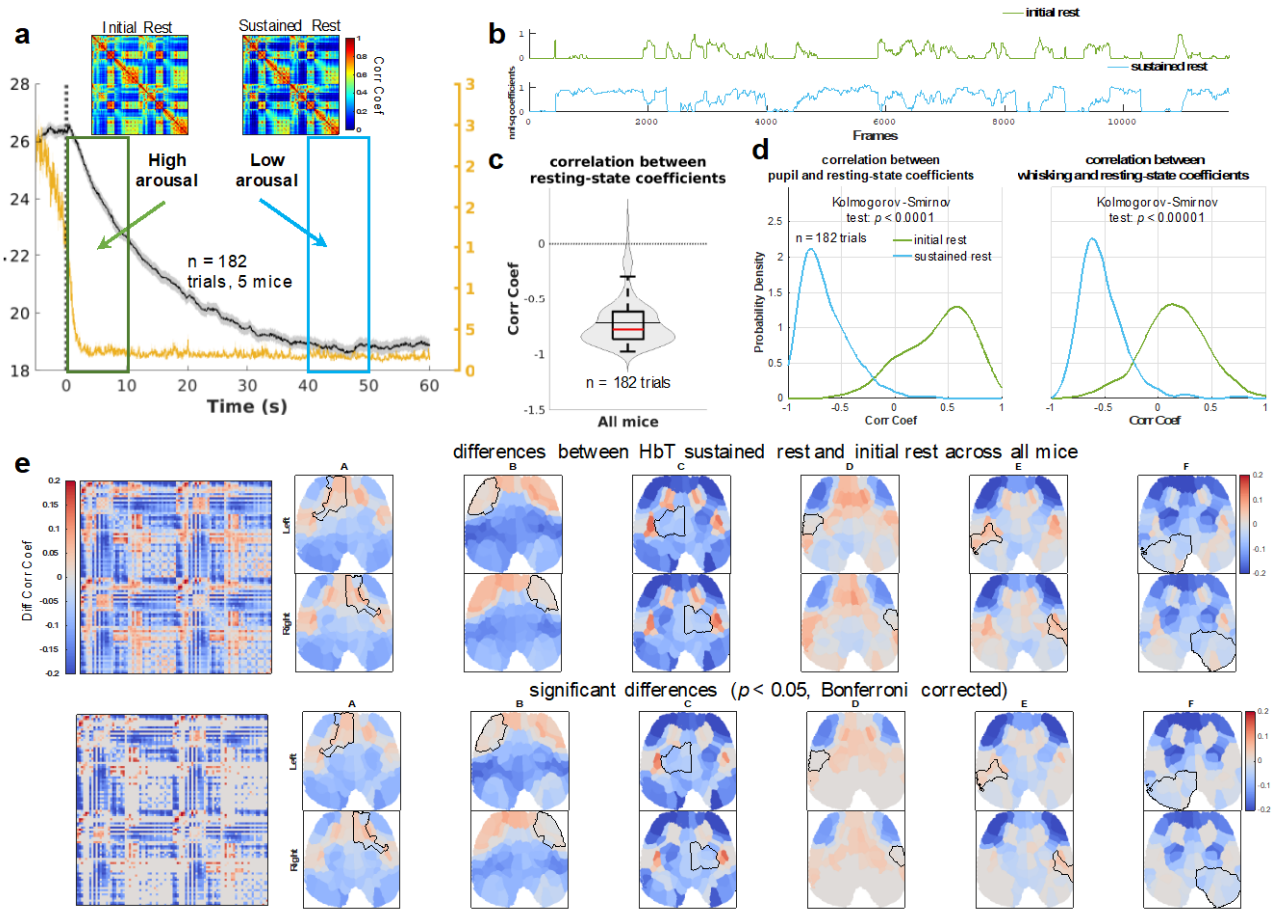

Figure 34 - Differences between the initial rest and sustained rest. A) Average whisking and pupil size over resting bouts. During the initial rest (right after running offset), indication higher arousal level, the pupil size is still large, while the pupil size returns to baseline during the sustained rest, implying lower arousal level. B) The resting-state coefficients predicted by the non-negative least squares model for one example of recording sessions. This plot demonstrates the fluctuation between the initial rest (green) and the sustained rest (blue) for one example trial. C) The reciprocal relationship between the initial-rest and sustained-rest coefficients. The plot shows the distribution of the correlation values between the initial-rest and sustained-rest coefficients estimated by the model for 182 resting bouts at least 60 seconds long. The box plot is centered on the median (the horizontal red line) and extend to the 25th and 75th percentiles. The black line within the violin plot indicates the mean. d Probability distribution of correlation values between resting-state coefficients (initial and sustained rests) and pupil size/whisking using kernel density estimation. 182 resting bouts at least 60 seconds long across all mice were considered. The green color indicates initial rest (high arousal) and blue color indicates sustained rest (low arousal). Using Kolmogorov-Smirnov test, a significant difference was found between the probability distributions (pupil: k = 0.23, p < 1e-4, whisking: Z = 0.3, p < 1e-7). E) Low arousal level accompanied with decreased synchrony between the anterior lateral frontal cortex and other brain regions. The brain maps show the significant differential correlation

coefficients relative to the seed regions. The red and blue colors indicate increased and decreased correlations when comparing the sustained rest with initial rest.

4.6 Conclusion

In this chapter, I found an association between ongoing changes in correlation patterns of neural jRGECO1a signals and overt behavior such as locomotion or endogenous brain states such as arousal level, showing that correlation patterns of neural signals encode behavior and arousal level. More importantly, I showed that the hemodynamic signals were able to capture the behavioral relevance of neural correlation patterns.

My findings provide strong evidence that rs-dFC has neural origins, and hemodynamic responses are able to depict correlation patterns that tracks rapid changes in behavior and internal brain states such as the level of arousal or alertness. One question still outstanding is how disease affects connectivity architecture of such spontaneous activity and how such alternations relate to behavioral impairments. More importantly, how much of the aberrant patterns can be captured by hemodynamic signals. As of now, previous fMRI rs-dFC studies have not been consistent in depicting reliable pathological patterns. One possible explanation can be that dynamic functional connectivity may capture differing transitions in moment-to-moment brain states rather than a generic aberrant pathological pattern. Since at the moment of fMRI scanning brain states such as alertness, mind wandering, or motor intents could be different between patients (particularly noting that an fMRI resting-state scan itself is an intense adventure and challenge for anyone, as in the case of a head fixed mouse), the structure of correlation patterns may mostly reflect how patients adjust to and accommodate the situation. Future studies are necessary to further investigate this speculation.

5 Chapter 5: Unsupervised Clustering of Neural activity

A key factor of our analysis that remains to be addressed is the relationship between these results and measures of Dynamic Functional Connectivity in human fMRI experiments. As discussed in Chapter 1, Dynamic Functional Connectivity is traditionally measured by clustering a set of temporally independent Functional Connectivity maps into some number of states, dimensionally reducing the dataset from a large number of FC windows to a small number of states, where each FC window is labeled as the state is it nearest to in the vector space. These states are then used to measure dynamic changes in brain state during imaging sessions by calculating the relative distances from raw FC maps to each dynamic state centroid.

Dynamic Functional Connectivity analysis is typically used in the context of human fMRI experiments. While most fMRI time series are on the order of hundreds of milliseconds per scan, WFOM enables orders imaging frequencies of magnitude higher at 20 frames per second per channel. Thus, I had more flexibility when considering the sliding window size, and initially opted to analyze dynamic changes on the order of two seconds, or 40 frames per FC window. I also opted to assess dynamic FC during periods of rest and locomotion, which differed from experimental paradigms used in human experiments, where subjects are required to remain at rest throughout the imaging session.

5.1.1 Calculation of Dynamic Functional Connectivity

Dynamic Functional Connectivity analysis is divided into three key steps, and is summarized visually in Figure 35:

1) Sliding correlation window calculation
2) Calculation of states via clustering

3) State vector labelling

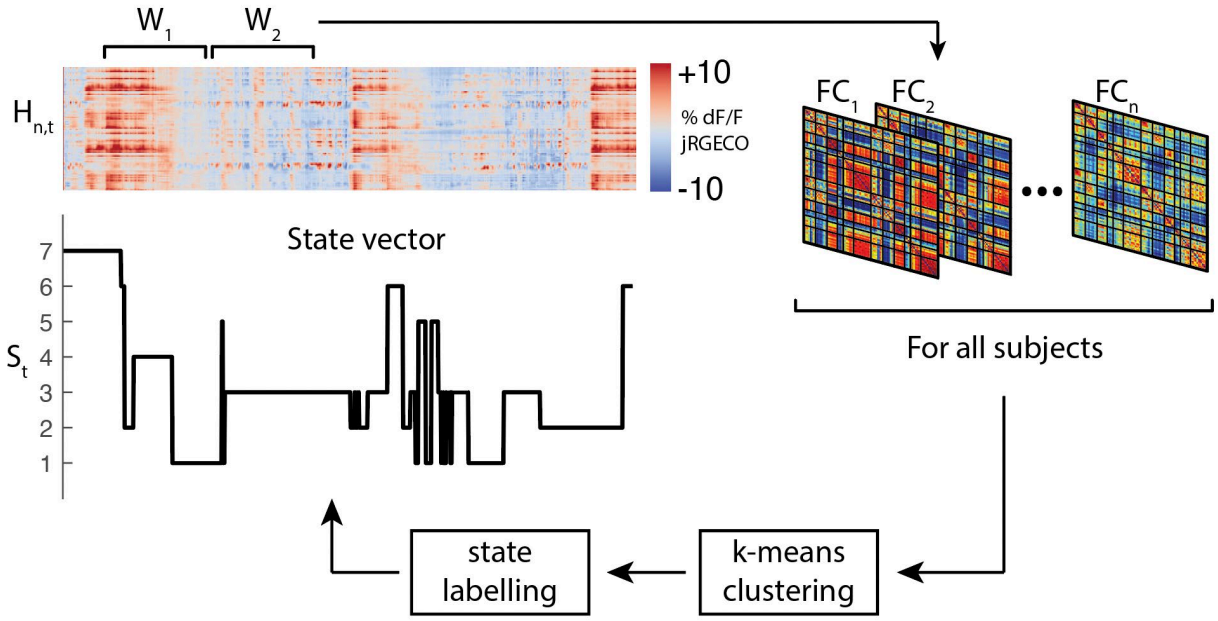

Figure 35 – Calculation of Dynamic Functional Connectivity.

Here, I will summarize the key conceptual and mathematical concepts that underly these steps.

5.1.2 Sliding window correlation changes in FC

The calculation of a sliding window can be summarized as follows. If we take two time series x and y with sampling rate *f*, we can calculate a sliding correlation window $cc_{t,x,y}$ at time point *t* as follows:

$$cc_{t,x,y} = corr(x[t-\Delta, t+\Delta], \mathrm{y}[t-\Delta, t+\Delta]) \tag{4.1}$$

We can then calculate the correlation coefficient for x and y using equation 1.1:

$$cc_{t,x,y} = \frac{\sum_{i=t-\Delta}^{t-\Delta}(x_i - \bar{x})(y_i - \bar{y})}{\sqrt{\sum_{i=t-\Delta}^{t+\Delta}(x_i - \bar{x})^2}\sqrt{\sum_{i=t-\Delta}^{t+\Delta}(y_i - \bar{y})^2}} \tag{4.2}$$

Here, Δ represents the window radius in samples. Thus, a given window is always centered at time *t* with an odd frame number $L = 2\Delta + 1$. Each FC window then has a full window width $W = L/f$. For a temporal sequence of *N* timecourses, this is calculated for every time course pair, creating a FC matrix with shape $N \times N$.

We first chose to use a 2 second sliding window ($\Delta = 20$ frames, $\mathrm{L} = 41$ frames) as I showed in Supplemental Movie 1, since WFOM enables us to measure neuronal activity at a high temporal frequency.

5.1.3 Calculation of states via clustering

For this work, I utilized k-means clustering, a simple yet popular clustering technique utilized in many studies of Dynamic Functional Connectivity in the human (Allen et al., 2014; Menon and Krishnamurthy, 2019; Sakoğlu et al., 2010). The k-means algorithm is summarized in Chapter 3. For our purposes here, we utilize k-means to decompose the full FC matrix:

$$FCM \xrightarrow{k-means} \begin{cases} S_t \\ C_k \end{cases} \tag{4.3}$$

Where S_t is an integer vector representing the nearest state for each sliding window FC, and C_k is a $k \times N \times N$ matrix, where M represents the number of independent basis timecourses that make up the FC window. Prior to clustering, all FC matrixes are collected, flattened, and concatenated to form the full sliding window FC matrix. This matrix has size $M \times N^2$, where M is the total number of FC windows captured.

5.1.4 State vector labelling

One advantage of dimensionality reduction approaches like k-means is that the centroids are an approximation of unseen data. Thus, a straightforward process can be carried out to label any FC window that was not included in the clustering by measuring the distance between each

state centroid and the raw FC matrix. This process assumes we have properly accounted for any differences in FC properties between the model and the data we choose to label. Thus, we do not need to use all data to create a representative model of it. This saves a great deal of computation time, and is a common technique in DFC studies.

5.2 Preliminary analysis of Dynamic Functional Connectivity in neural timecourses

We first carried out a series of exploratory analyses on a small subset of data collected in a Thy1-jRGECO1a mice (Dana et al., 2018, 2016). This analysis was carried out prior to our clustering technique developments outlined in Chapter 3, and utilized a more straightforward approach that did not account for cross subject inconsistencies or bilateral component matching.

5.2.1 Replicate analysis of k-means clustering

We first wanted to determine the consistency of clustering a single epoch into representative states, and the degree of consistency we would observe from multiple clustering initializations. This is a key first step to establish that our data is separable. One common approach to improving consistency of k-means clustering is to run the algorithm multiple times with different initializations, then choose the output with the lowest MSE to the input data. This ensures that the model escapes local minima, and is a good representation of the global minimum in the parameter space.

Figure 35 illustrates the effect of replicates on our data. Figure 35A shows the state centroids output from independent k-means iterations. Each row has slight, but noticeable inconsistencies in some states, most notably state 3 and 7. Figure 35B shows the output after using 20 replicates for 5 independently run models of the same dataset. Note that clusters could

be easily matched across multiple k-means initializations, and showed higher degree of consistency across separate instances.

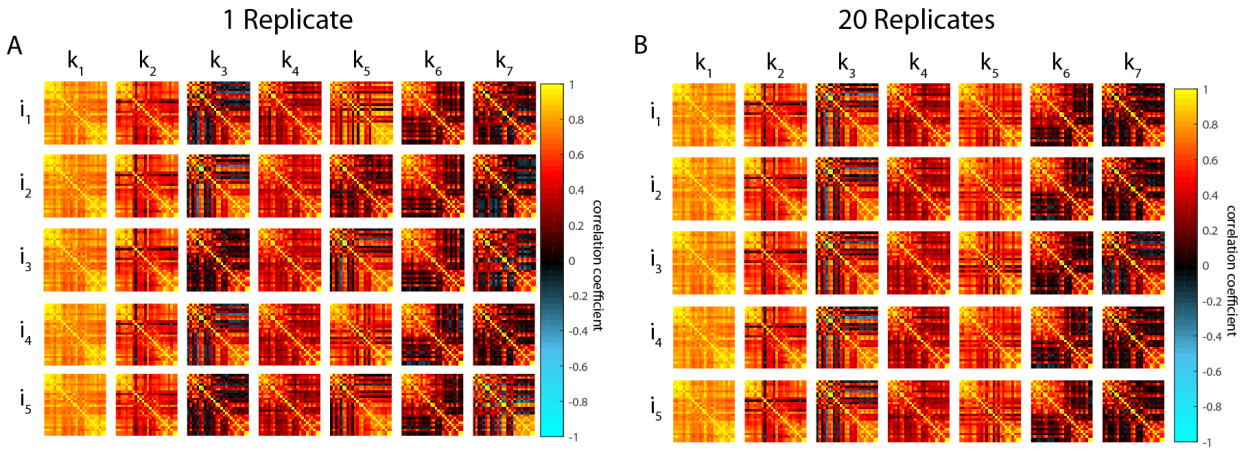

Figure 36 - Comparison of correlation state outputs. A) Outputs from 5 separate models, with one replicate. B) Outputs from 5 separate models, with 20 replicates. Note map inconsistencies in A that are resolved in B.

5.2.2 Cluster consistency across sessions and subjects

I next wanted to assess if correlation map states showed consistency across subjects, and across large periods of imaging. Figure 36 shows multiple comparisons of output correlation state maps, in one of three groupings:

1) Three 10-minute runs from the same mouse and imaging session

2) One 10-minute run each from three different imaging sessions

3) One 10-minute run from 3 different sessions and 3 different mice (9 runs in total).

The seven output states not only show general consistency across subjects and trials, but reveal structurally diverse correlations.

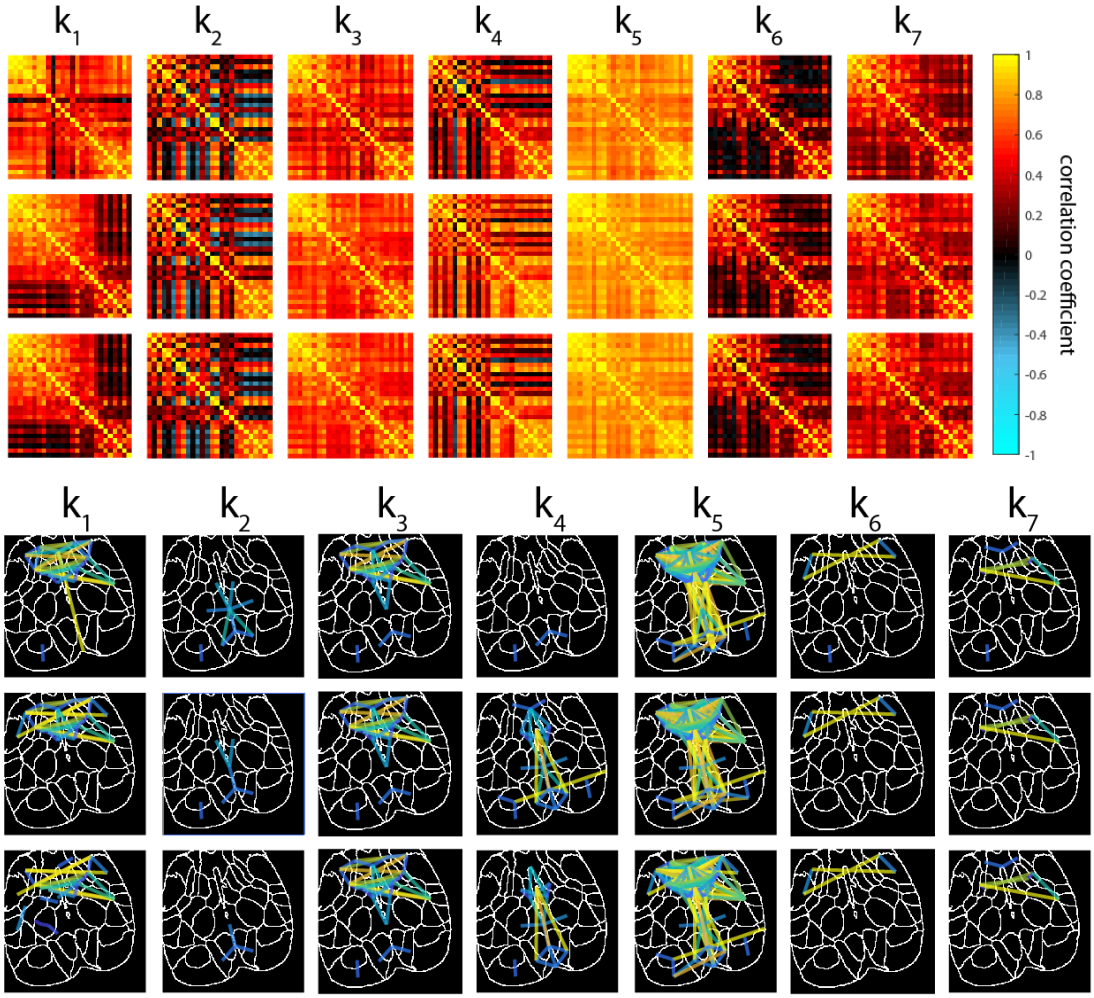

Figure 37 - Correlation state maps from three datasets: (Top row) One subject from a single imaging session, (Middle row) One subject from three separate imaging sessions, (Bottom row) Three subjects from three different imaging sessions (9 in total). (Bottom) Structural projections of highly correlated regions. Each plot shows an outline of the dorsal cortical area where neural activity was measured, with white borders representing cluster components for time course extraction. Each line indicates a strong functional connectivity measure between those regions, here defined as a correlation coefficient greater than 0.9. Color indicates physical distance between clusters, with nearby clusters colored in blue and disparate clusters colored in yellow.

I next wanted to better understand the topological structure of these correlations, by visually connecting highly correlated regions. Figure 36 shows all correlations higher than 0.9, and draws pseudo-colored lines (based on centroid distance) showing the anatomical connections between regions that share high correlations.

The structural representations of these correlations reveal more information about the functional mappings of these states:

1) State k1 shows high activation of primary and secondary somatosensory regions.

2) State k2 shows specific connectivity near retrosplenial and primary motor cortexes.

3) State k3 is similar to k1, but also shows high correlations in the left visual and right somatosensory regions.

4) State k4 shows inconsistencies, incorporating diverse regions along the midline and visual regions in conditions 2 and 3 but not in 1.

5) State k5 shows high correlations across a majority of the cortex.

6) State k6 is highly specific in only a few motor regions.

7) State k7 is similar to state k6, but seems to recruit differing motor regions, but similarly to state k3 incorporates a right somatosensory and whisker area.

To further an understanding of these states, I also assessed behavioral measures, grouped by the state label of each epoch. Figure 37 shows the average behavioral measures (movement speed and pupil size) within each state epoch, scaled using z-score to reduce cross-subject variability. Each of the seven states reveals a high degree of behavioral specificity, with states k_2, k_4, and k_7 containing a wide variety of pupil size, but relatively little movement.

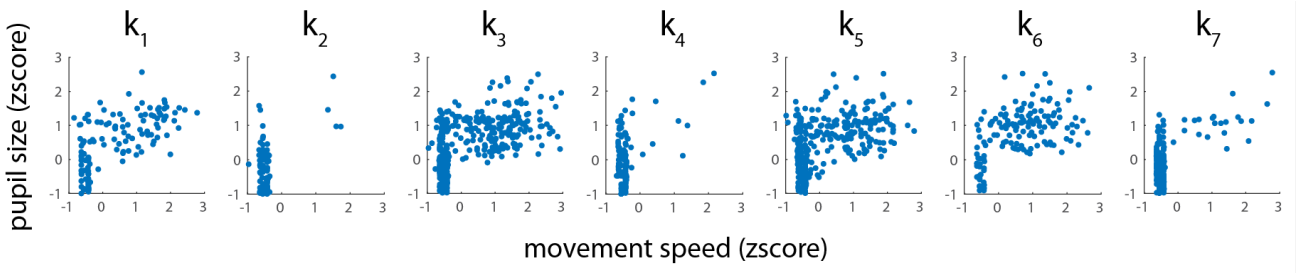

Figure 38 - Behavioral measures in each state – movement speed (z-score) is shown along the x axis, and pupil size (z-score) is shown along the y axis. States show high

specificity of behavioral tendencies, with some incorporating mostly pupil movements, and other incorporating both pupil and locomotion.

While these results show a promising effect of partitioning behavior by brain state, there are confounding issues that must be addressed. In this model, all states contained a mixture of locomotion activity and resting state epochs, with widely varying whisking parameters. We should ideally be able to separate movement and resting state epochs into entirely different representative states, rather than distributions that contain a mixture of both.

5.2.3 Locomotion discrimination

These observations lead me to hypothesize at least two dynamic states I could observe: a state observed during locomotion, and a state observed during rest. Similar to what I did in Chapter 4, I decided to expand the sliding window for continued analysis, first to better capture hemodynamic fluctuations, and to provide enough information to capture changes in behavior I observed in the last chapter.

We used 10 second sliding FC windows in a single 10-minute imaging session, which was then clustered into 2 states using k-means clustering and Euclidean distance as the optimization metric. The state labels were then assigned to two categories: states measured during rest, where all frames within the window contain no locomotion, and states measured during locomotion, where the window contains at least one frame of locomotion. I then assessed the sensitivity of the clustering model to detect running bouts.

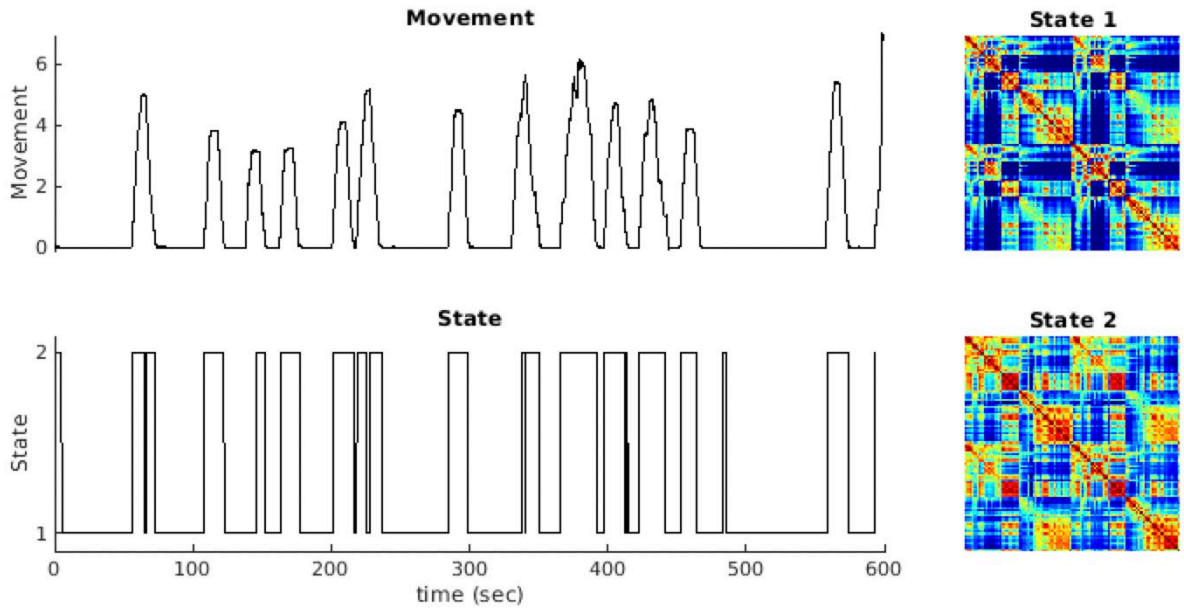

Figure 39 – Detection of running bouts using kmeans clustering (Left, top) Smoothed movement value using a 200 frame smooth filter. (Left, Bottom) State vector output from kmeans algorithm. (Right) State centroids from kmeans model. Note the heightened correlation coefficients in State 2, which is typically present during running.

Figure 38 illustrates the cluster outputs and labels for a two-state cluster model. A clear delineation between an "active" and "rest" state is observed, which affirms the hypothesis that Dynamic Functional Connectivity analytical methods are a valid approach to decompose gross changes in arousal such as locomotion and rest effectively. There is also a clear difference between the state centroids – State 1, most common during rest, has lower overall correlation coefficients than State 2, indicating that periods of rest are marked by a higher degree of desynchronous activity across the cortex. This is consistent with our initial observations of FC dynamics illustrated in Figure 30.

5.2.4 Non stationarity of Sliding Windows

To further validate that unsupervised clustering reveals dynamic FC changes, I performed a test of non-stationarity in both neural and hemodynamic data. This can be done in a few ways (Hutchison et al., 2013), notably through bootstrapping (Keilholz et al., 2013), permutation

(Sakoğlu et al., 2010), and phase randomization (Allen et al., 2014). Phase randomization in particular tests "… the hypothesis that the frequency characteristics of sliding window time series were dependent on the precise timing relationships between regional time courses by keeping the amplitude spectra of individual time series constant while randomizing the phase" (Hutchison et al., 2013). This approach is the most straightforward and direct method to validating non-stationarity.

Phase randomization was applied to both neural and hemodynamic FC windows, first by applying a uniform phase randomization, and then by applying a different phase randomization to each FC window, similar to the technique shown in Figure 39 above. The expected result was that state centroids would not change when applying a consistent phase shift (SR1), and that state centroids would be similar to the average FC map (Figure 39B) when applying a randomized phase shift (SR2).

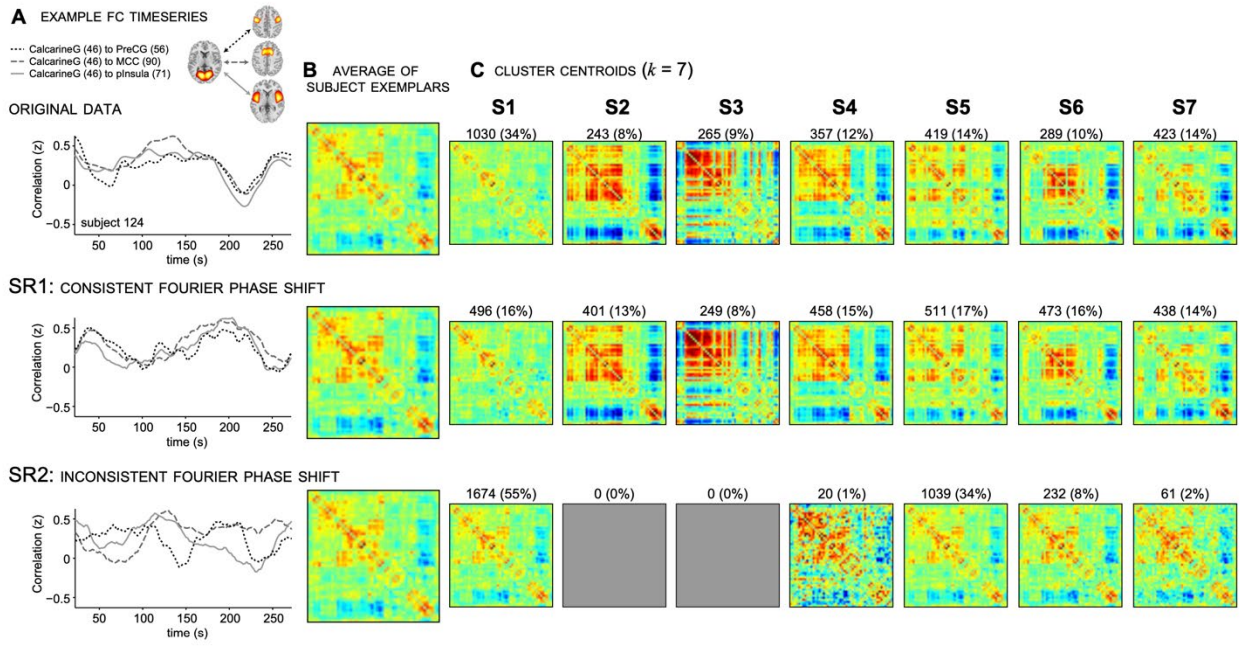

Figure 40 – Phase randomization of human fMRI FC timecourses to validate Dynamic Functional Connectivity. (Top row) Standard output from clustering algorithm. (Middle row)

Phase randomized output with consistent phase. (Bottom row) Phase randomized output with inconsistent phase. Adapted from (Allen et al., 2014).

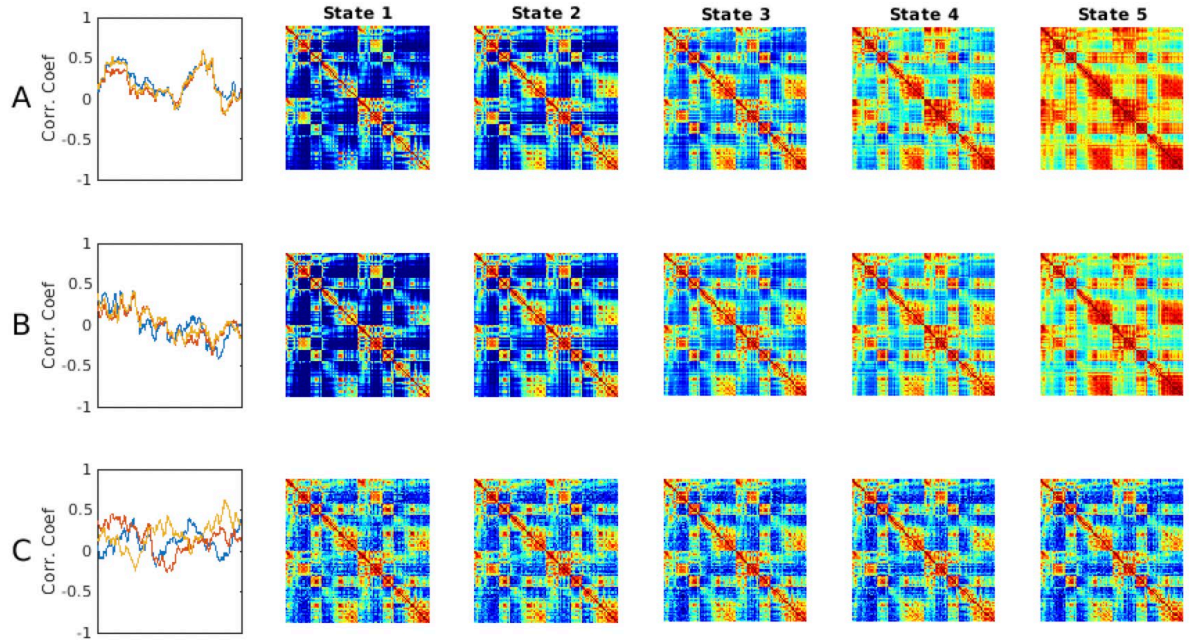

Figure 41 – Phase randomization of mouse neural FC matrixes. (A) Standard output from clustering algorithm. (B) Phase randomized output with consistent phase. (C) Phase randomized output with inconsistent phase.

Phase randomization was applied to neural FC timecourses (Figure 40). Condition A (control) and condition B (uniform phase randomization) resulted in nearly identical centroids, while condition C (nonuniform phase randomization) resulted in a total loss of heterogeneity between state centroids. This strongly supports the hypothesis that neural activity clustering produces independent state centroids.

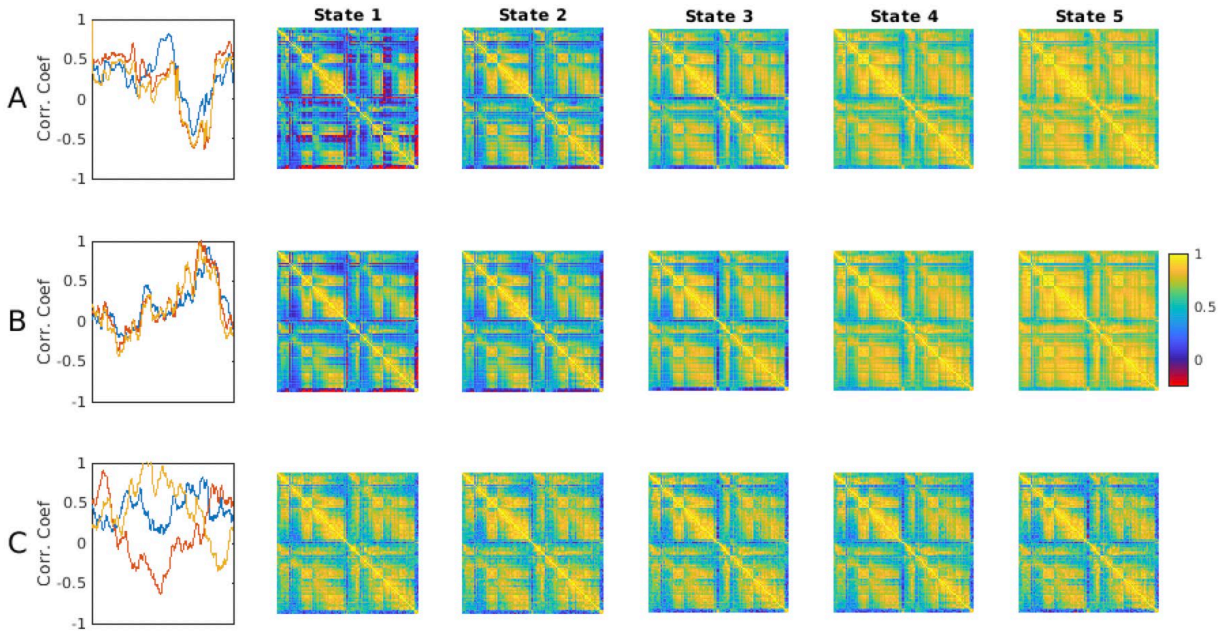

Figure 42 - Phase randomization of mouse hemodynamic FC matrixes. (Top row) Standard output from clustering algorithm. (Middle row) Phase randomized output with consistent phase. (Bottom row) Phase randomized output with inconsistent phase.

Phase randomization was applied to hemodynamic FC timecourses (Figure 41). Similar to neural activity, Condition A (control) and condition B (uniform phase randomization) resulted in nearly identical centroids, while condition C (nonuniform phase randomization) resulted in a total loss of heterogeneity between state centroids.

5.3 A systematic model of Dynamic Functional Connectivity: Neural Activity

Having established that neural activity exhibits fluctuations in Functional Connectivity linked to behavioral changes, and that unsupervised clustering does reveal distinct neural states that are not stationary in nature, I next created a model to assess the relationship between behavior and dynamic FC state as measured by unsupervised clustering. Based on the locomotion discrimination results and my work in Chapter 4, I decided to use a 10 second window, which balances providing enough information to estimate Functional Connectivity

within the epoch, as well as discriminating between different behavioral transitions, which typically occur at least every 10-20 seconds.

5.3.1 Analytical methods

A total of 43 ten-minute sessions across 5 mice were used to cluster neural activity into 5 representative states. For the clustering step, windows were captured every 100 frames, which resulted in a total of 5160 FC windows for k-means clustering. To avoid any local minima in the clustering step, 100 replicate clustering iterations were run, and the replicate with the lowest MSE to the input data were used for the final model. Then, all data were labeled using the 5 state centroids, by assigning each FC window to the state with the lowest Euclidean distance. Once all data had been labeled, states vectors were ordered to minimize the overall transition magnitude, calculated as the average magnitude of each state transition over all data. This was done to improve the interpretability of state vector visualization, since transitions to neighboring states may help us better understand the overall dynamics of state transitions.

5.3.2 Results

First, I assessed the resulting state centroids and compared multiple labeled imaging sessions. Figure 42 shows the state centroids, along with behavioral data and state vectors for one ten-minute session from each mouse. I immediately noted that in all sessions, states 4 and 5 were most commonly present during locomotion events, while states 1-3 were present during resting state and transitionary epochs. While some periods of rest exhibited rapid oscillations between states, others were quite stable, remaining in a steady state for minutes at a time. This general pattern of the state vectors was consistent across all mice.

Next, I assessed the connectivity patterns for each state. I noted that states present during rest (States 1-3) had lower overall correlation values, and State 1 had a notable group of negative correlations.

5.3.3 K-means efficacy

The primary goal when applying techniques such as k-means clustering is to provide some low dimensional representation of the input data that approximates it meaningfully. To measure the efficacy of this approach, I measured if the distance to each FC window's centroid was lower than the distance to the average of all FC windows. This effectively compares clustered data to unclustered data, while accounting for the variance within the data itself. These measures were used to perform a paired, left tailed t-test to test the null hypothesis that the average distance to the state centroid does not decrease meaningfully. I used a Bonferroni correction for multiple comparisons, and set the level of significance at $p = 0.05/5 = 0.01$. All models rejected the null hypothesis at a level of p = 0.01, indicating that k-means clustering is reliably reducing the average label distance to state centroids compared to an unclustered control model. The table below summarizes these results:

variable	zval	signedrank	pval	h_reject
Mouse 1, Neural model	-17.31	4491	1.9786e-67	true
Mouse 2, Neural model	-17.702	3329	2.028e-70	true
Mouse 3, Neural model	-17.74	3217	1.0361e-70	true
Mouse 4, Neural model	-17.928	2660	3.5964e-72	true
Mouse 5, Neural model	-17.891	2769	6.9613e-72	true
Mouse 1, Hemodynamic model	-16.381	7244	1.2979e-60	true
Mouse 2, Hemodynamic model	-17.833	2939	1.9448e-71	true
Mouse 3, Hemodynamic model	-18.092	2172	1.8389e-73	true
Mouse 4, Hemodynamic model	-16.342	7362	2.495e-60	true
Mouse 5, Hemodynamic model	-18.064	2255	3.055e-73	true

Figure 42 shows the neural state centroids and a single 10-minute imaging session in each of the five mice, with behavioral metrics and the associated state vector during that timeframe. I immediately noted that based on the state order I had determined, that movement epochs coincided with two particular states (State 4 and 5), and seemed completely absent outside of movement epochs. This is most obvious when looking at Mouse 5's imaging session (bottom plot, Figure 42), where a long period of no locomotion remains in states 1-3 nearly the entire period, with a few brief "excursions" into state 4. Interestingly, those few short "excursions" into state 4 seem to be associated with brief whisking events, which leads us to hypothesize that even small whisking events with no associated locomotion have impacts on overall Dynamic FC metrics.

Assessment of functional connectivity structure (Figure 30) revealed some notable properties between these states. Neural states present during locomotion (States 4 and 5) had the same increased overall correlation values that I observed in the single session analysis, while those states observed during rest (States 1, 2, and 3), exhibited decreased connectivity with disparate regions, in particular with Group B (Figure 43). I also noted that bilateral connectivity between anterior regions was heightened in the locomotion-associated states compared to states observed during rest, which indicates a degree of bilateral coordination present in the visual cortex and associated regions during focused tasks such as locomotion. These results are similar to those I observed in Chapter 4, but require a closer look to confirm.

We noted a striking desynchronization between posterior visual regions (Group F) and anterior lateral frontal cortical components (Group B). This desynchronization increases in the lower, less active states. Recently, the anterolateral area has been reported as a key subnetwork, the correlation patterns of which with posterior networks are modulated by arousal level (Benisty

et al., 2021). Therefore, in line with mouse behavior, the anatomical differences between these rest states may also indicate the changes in these FC patterns may be linked to arousal fluctuations. This finding suggests that changes in spontaneous activity of the anterior lateral frontal cortex that becomes significantly less synchronized with other brain regions may be a key feature of shifts in arousal during resting state.

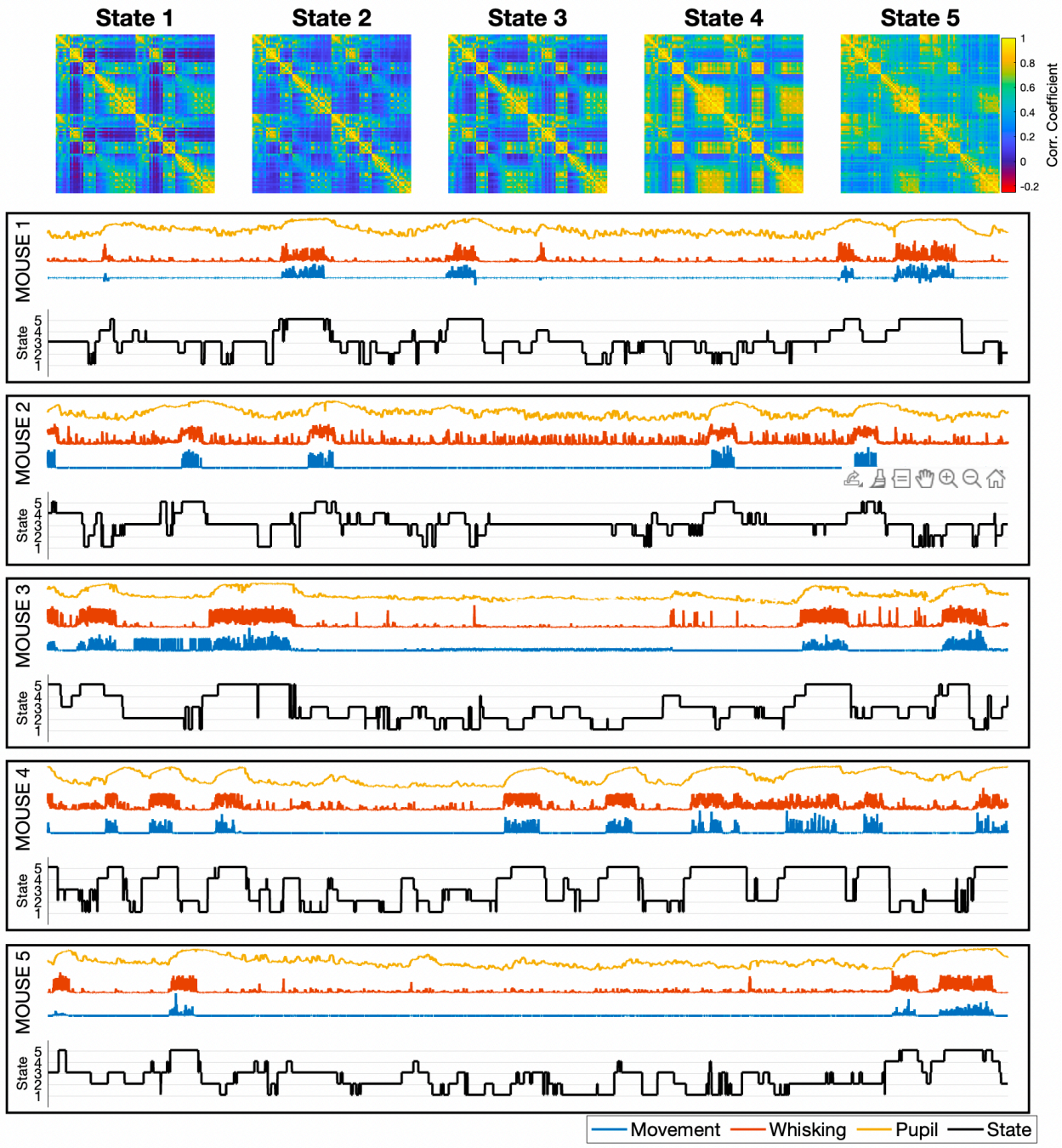

Figure 43 – Neural Dynamic Functional Connectivity model. (A) State centroids, arranged to maximize neighboring transitions. (B) Example sessions from each mouse. Colored lines represent measures of pupil (yellow), whisking (blue) and paw movement/locomotion (red). Black lines indicate state assignments using a 10 second centered sliding FC window. All epochs are 10 minutes in length.

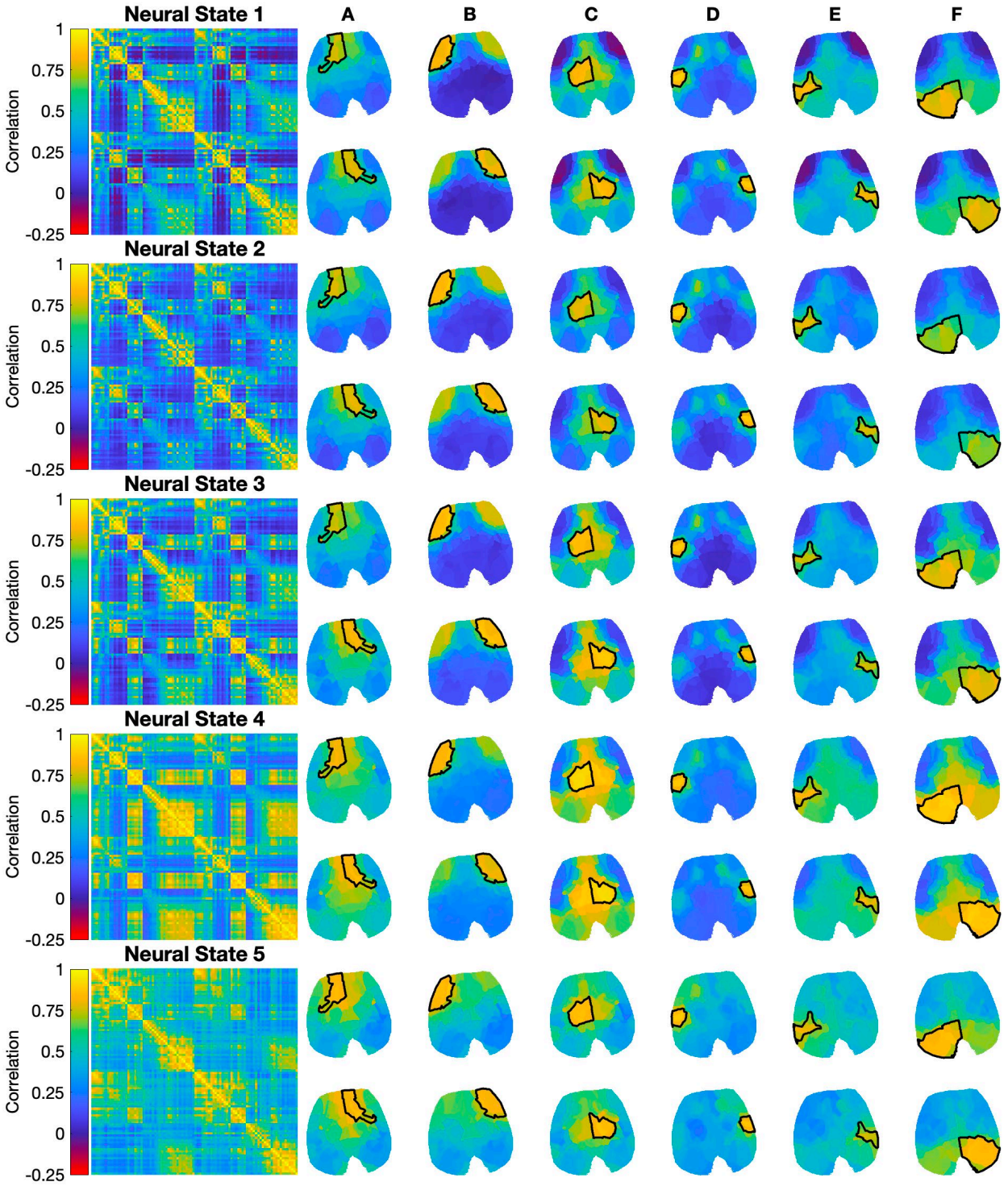

Figure 44 – Anatomical visualization of neural FC state centroids. Square FC matrixes represent the same states shown in Figure 42, and each brain map illustrates the average correlation coefficient with components inside the bordered region.

5.3.4 Behavioral dynamics

Based on a cursory analysis of individual imaging sessions, I hypothesize that behavioral dynamics seemed to exist on a continuum where states exhibited increasing average pupil diameter, movement activity, and whisking activity. Additionally, I hypothesize that even small behavioral changes such as minor whisking events seem to result in significant fluctuations in FC metrics, pushing the state vector into higher, more behaviorally active states. To assess these questions, I captured pupil size and whisking activity levels across all labeled datasets (42 ten-minute runs in total across 5 mice) by measuring average movement, whisking and pupil levels within FC window indexes. Each average behavioral value was then assigned to the state vector assignment at the center of the window. To prevent redundant measurements due to window overlap, I captured behavioral metrics every 200 frames. Behavioral variables were normalized to account for differences in camera and mouse positioning within the behavior camera FOV.

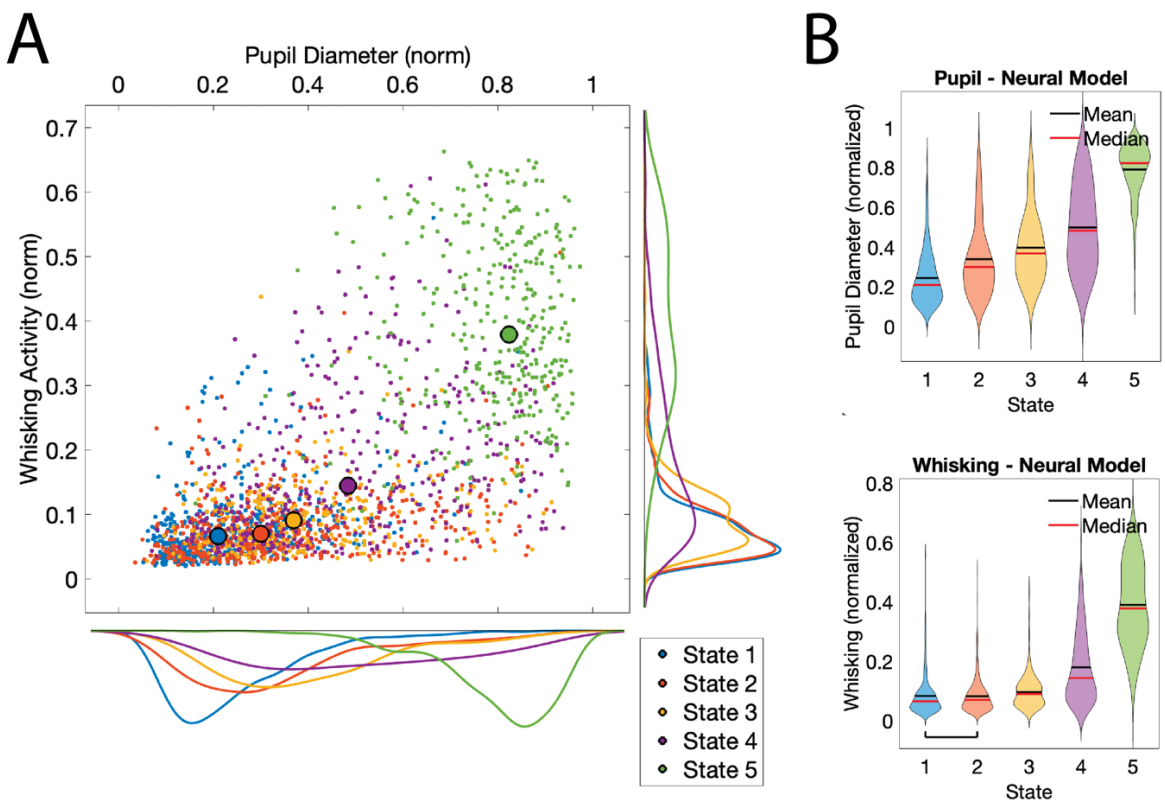

Figure 45 - Behavioral metrics of Dynamic Functional Connectivity in Neural activity. (A) Scatter plot of behavioral values. Small colored dots represent average behavior values within a single FC window (x axis: pupil diameter, y axis: whisking activity), with each color representing one of the five neural state assignments. Large dots represent the average of all measures in that state. Distributions along each axes represent the kernel distribution approximation of each variable dimension. (B) Violin plots of the same distributions. Black bars indicate the mean and red bars indicate the median of the distribution. All distribution pairs were found to have statistically significant differences, except for Whisking groups 4 and 5 (black bracket, bottom right).

Figure 44 Illustrates the behavioral distribution in pupil and whisking metrics. There is a clear continuum of increasing whisking activity and pupil size, confirming our previous hypothesis that these behavioral changes are associated with state vector. While state 5 is a key outlier, the other states have less drastic differences. Comparing these distributions, all were found to have meaningfully different distributions (average k = 0.53, average *p* 2.2147e-07,

Kolmogorov-Smirnov test with Bonferroni correction.) except for one pair (State 4 vs State 5, k = 0.04, p = 0.5677). See Table 2 for full results.

5.4 A model of Dynamic Functional Connectivity: Hemodynamic Activity

Having established that neural activity exhibits fluctuations in Functional Connectivity linked to behavioral changes, and that unsupervised clustering does reveal distinct neural states, I next created a model to assess the relationship between behavior and dynamic FC state as measured by unsupervised clustering. Based on the locomotion discrimination results, I decided to use a 10 second window, which balances providing enough information to estimate Functional Connectivity within the epoch, as well as discriminating between different behavioral transitions, which typically occur at least every 10-20 seconds.

5.4.1 Analytical methods

Analysis was carried out identically to the neural model, with a few key differences. Hemodynamic activity was assessed using total hemoglobin (CHBO+CHBR), and was lowpass filtered prior to clustering, due to the presence of high frequency components I believed to be spurious in nature and not representative of actual hemodynamic activity. A total of 43 ten-minute sessions across 5 mice were used to cluster neural activity into 5 representative states. For the clustering step, windows were taken every 100 frames, which resulted in a total of 5160 FC windows for k-means clustering, and 100 replicate clustering iterations. Similar to the neural model, states were ordered to minimize the overall transition magnitude.

5.4.2 Fisher transform

A common analytical technique in DFC fMRI analysis is the use of the fisher transform to normalize correlation coefficient distributions prior to clustering (Allen et al., 2014). The fisher transform normalizes skewed distributions using the inverse hyperbolic tangent function:

$$cc_F = tanh^{-1}(cc) \tag{4.4}$$

Since normally distributed data is an ideal candidate for clustering algorithms like k-means, the fisher transform is typically applied to fMRI BOLD FC matrixes, since they tend to have skewed distributions (Thompson and Fransson, 2016).

I first validated the need for a fisher transform to normalize correlation distribution in neural and hemodynamic timecourses. A subset of collected FC windows was collected in both neural and hemodynamic activity, shown in Figure 45. While neural activity has near-normal distribution, hemodynamic activity exhibits a highly skewed distribution. This is corrected after applying the fisher transform. Based on these results, I opted to use the fisher transform prior to clustering.

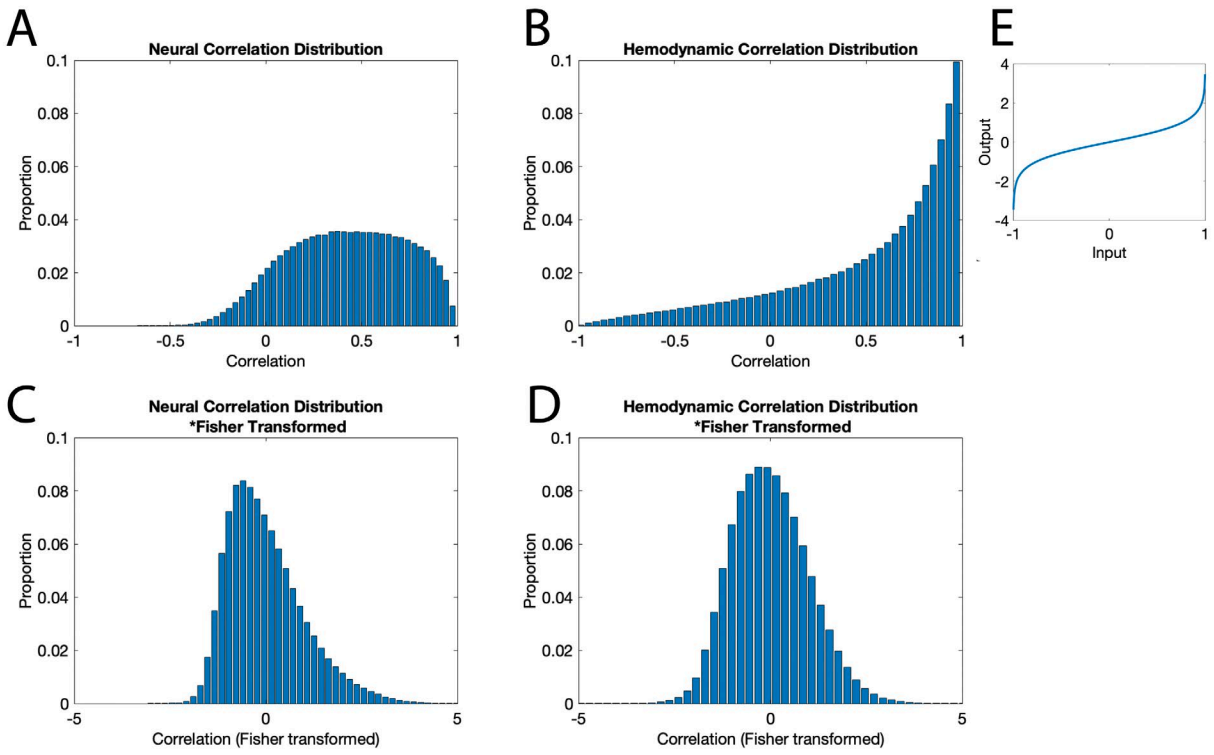

Figure 46 – Comparison of correlation coefficient distributions. (A) Neural model, (B) Hemodynamic model, (C) Neural model after Fisher transform (D) Hemodynamic model after Fisher transform. (E) Fisher transform function ($cc_F = tanh^{-1}(cc)$)

5.4.3 Differences between hemodynamic state centroids

Figure 42 shows the overall state centroids, along with behavioral data and state vectors for one ten-minute session from each mouse. I immediately noted that in all sessions, states 4 and 5 were most commonly present during locomotion events, while states 1-3 were present during resting state and transitionary epochs. While some periods of rest exhibited rapid oscillations between states, others were quite stable, remaining in a steady state for minutes at a time. This general pattern of the state vectors was consistent across all mice.

Next, I assessed the connectivity patterns for each state. I noted that states present during rest (States 1-3) had lower overall correlation values, and State 1 had a notable group of negative correlations.

Assessment of functional connectivity structure (Figure 30) revealed some similar properties between these states compared to neural activity, as well as some divergent properties. Hemodynamic states 4 and 5 were more present during locomotion, similar to the neural model. However, the differences in correlation amplitude were not as clear compared to the neural model. Additionally, state 5 had notable disruptions in the overall structure of the correlation map (visualized as discolored bands running through the map), which were also slightly present in State 4.

While I did observe strong desynchronous activity in States 1 and 2, each state has a strikingly different architecture – Hemodynamic State 2 was very similar to neural State 1, while Hemodynamic state 1 seemed to have its own desynchronous network. Looking at the anatomical projections on hemodynamic State 1, I observed that the while the Visual networks (Cluster F) were broadly dissociated with all other groups similar to neural State 1, there was also strong dissociation between Cluster D and Cluster F, a property not observed in the neural model. Based on our previous assessment of the Cluster map and anatomical overlays of mouse cortical regions, I hypothesize that Cluster D could represent somatosensory/whisker barrel regions responsible for fine touch sensation.

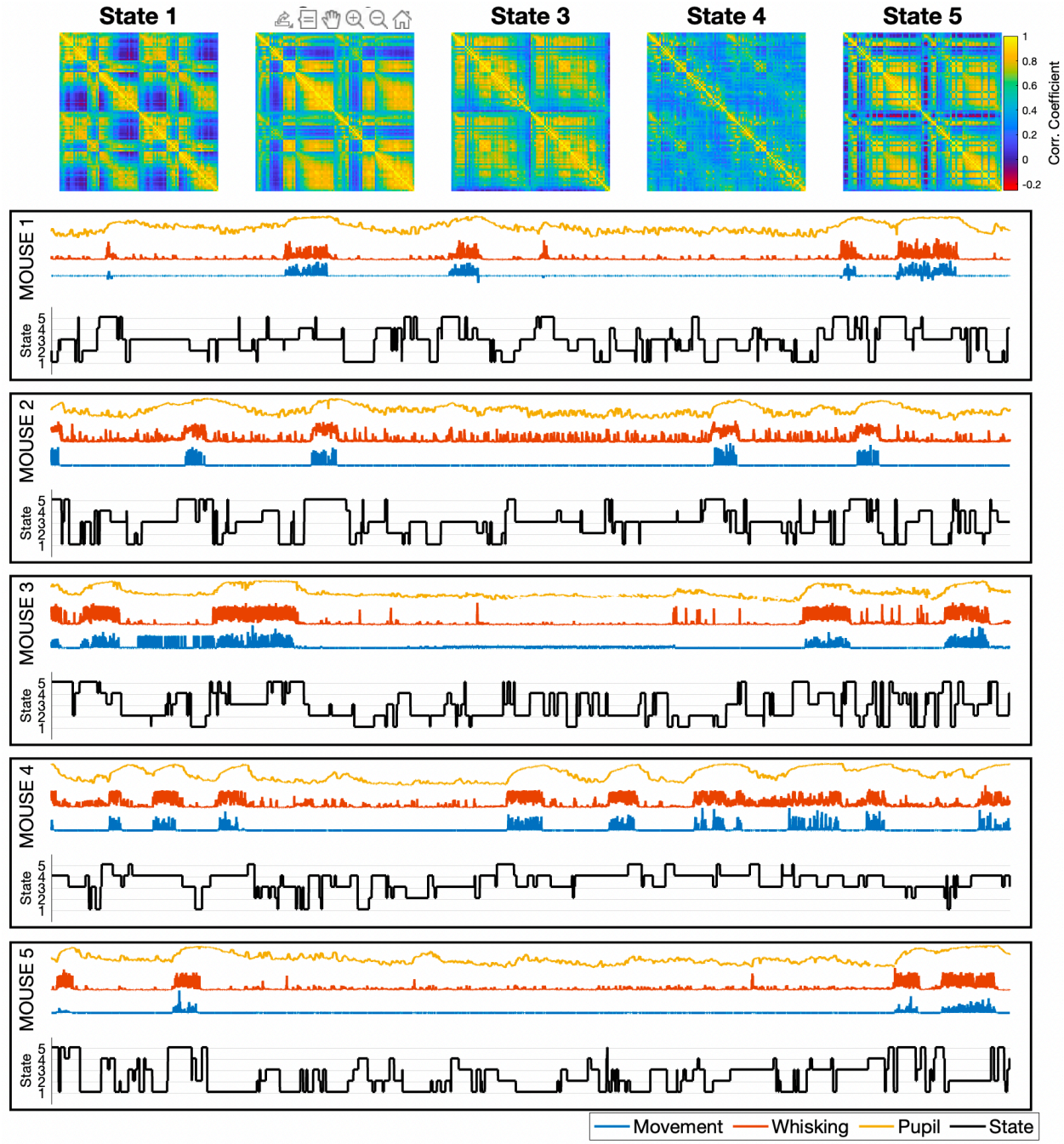

Figure 47 – Hemodynamic Dynamic Functional Connectivity model. The top row shows State centroids, arranged to maximize neighboring transitions. Black boxes contain example sessions from each mouse. Colored lines represent measures of pupil (yellow), whisking (blue) and paw movement/locomotion (red). Black lines indicate hemodynamic state assignments using a 10 second centered sliding FC window. All epochs are 10 minutes in length.

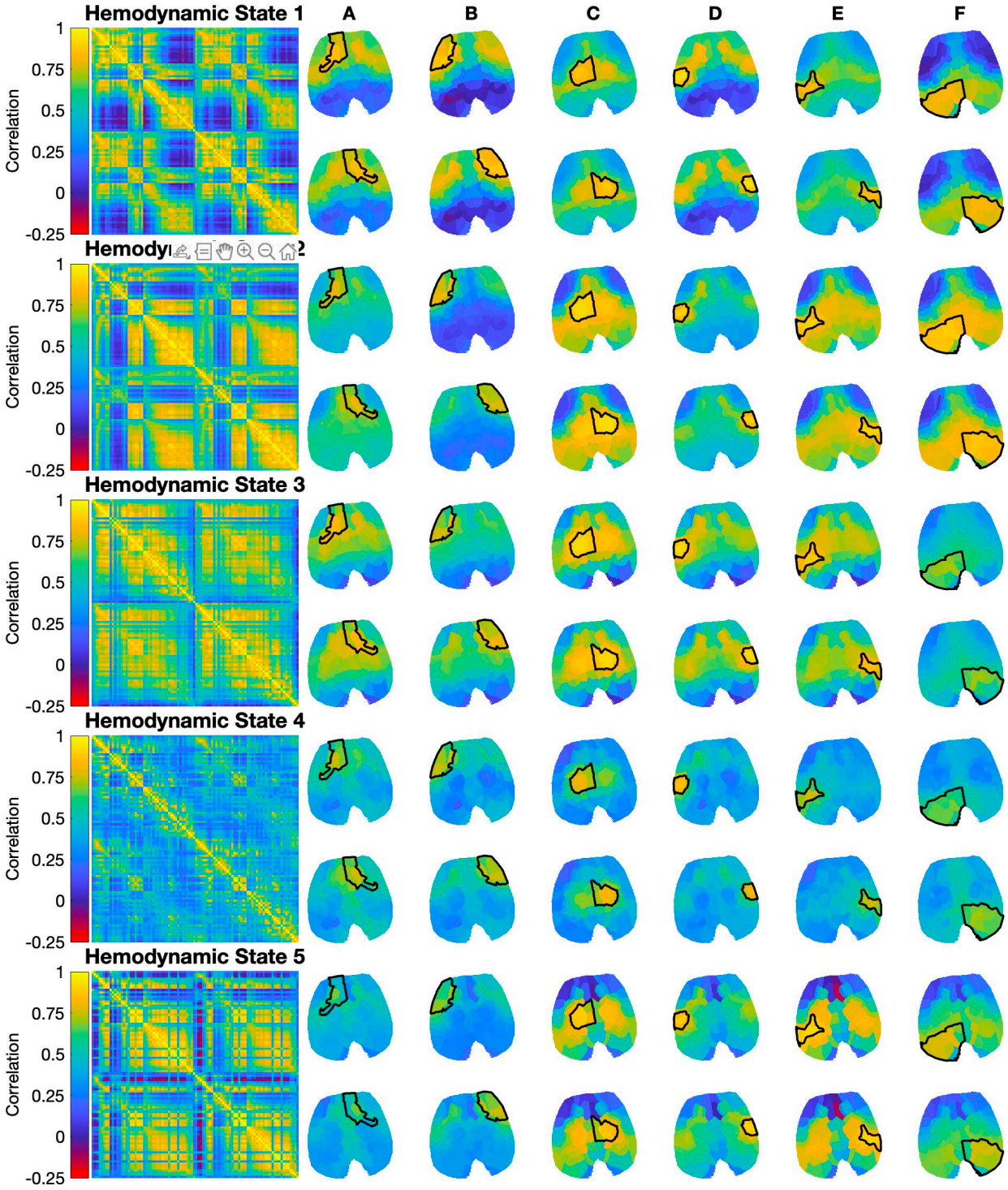

Figure 48 – Anatomical visualization of hemodynamic FC state centroids. Square FC matrixes represent the same states shown in Figure 46, and each brain map illustrates the average correlation coefficient with components inside the bordered region.

5.4.4 Behavioral dynamics

Based on a cursory analysis of individual imaging sessions, I hypothesize that behavioral dynamics seem to exist on a continuum where states 1-5 exhibit increasing average pupil diameter, movement activity, and whisking activity. To assess this, I captured behavioral activity levels across all labeled datasets (42 ten minute runs in total across 5 mice) by measuring average movement, whisking and pupil levels within FC window indexes. Each average behavioral value was then assigned to the state vector assignment, after normalization to account for differences in camera and mouse positioning within the behavior camera FOV.

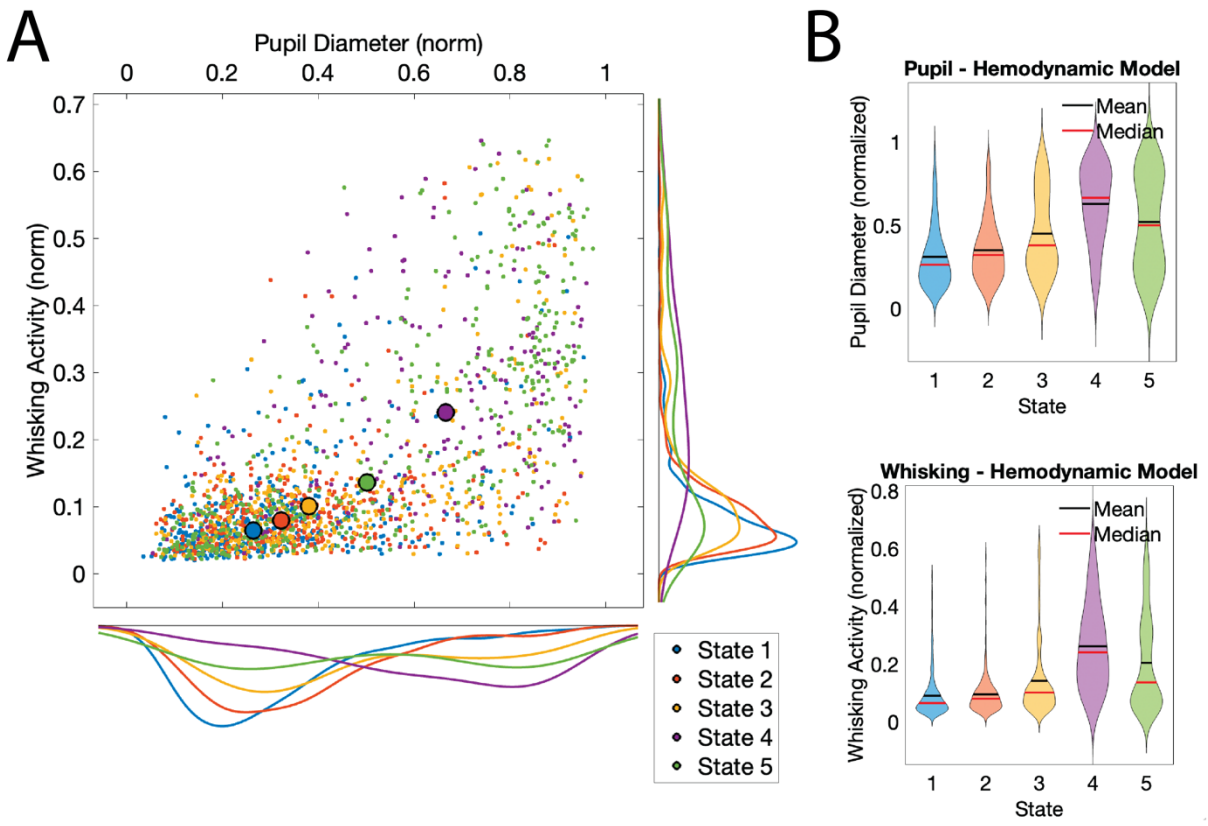

Figure 49 Raw behavioral metrics summary for hemodynamic model. (A) Scatter plot of behavioral values. Small colored dots represent average behavior values within a single FC window (x axis: pupil diameter, y axis: whisking activity), with each color representing one of the five neural state assignments. Large dots represent the average of all measures in that state. Distributions along each axes represent the kernel distribution approximation of

each variable dimension. (B) Violin plots of the same distributions. Black bars indicate the mean and red bars indicate the median of the distribution. All distribution pairs were found to have statistically significant differences.

Figure 48 shows the behavioral distribution in pupil and whisking metrics for the hemodynamic model. Similar to the neural model, there is a clear continuum of increasing whisking activity and pupil size. One notable difference is that the overall distribution is slightly less varied compared to the neural model. Comparing these distributions, all were found to have meaningfully different distributions (average k = 0.48, average p = 5.7164e-06, Kolmogorov-Smirnov test with Bonferroni correction). See Table 3 for full results. Overall, these results agree with the neural DFC model as a discriminator between varying levels of arousal, which clearly modulate FC dynamics.

5.4.5 Neural and hemodynamic centroids exhibit consistency when comparing across subjects

While k-means is an effective way to separate data into meaningful groups, it is crucial that the model output is checked for adequate representation across the sample space. For example, a model that clusters 1000 samples into 5 groups, but only assigns one cluster using a single sample is not a representative model of that data, but rather a model that was exposed to an outlier and clustered that outlier into its own group. If the state vectors were biased by group level differences (either due to subject or session level differences), we would find that certain states were not represented in the training dataset.

FC windows from the full model were grouped according to the state label and mouse, and the average FC map was calculated and compared across each subject to verify consistency of modeling (Figure 49).

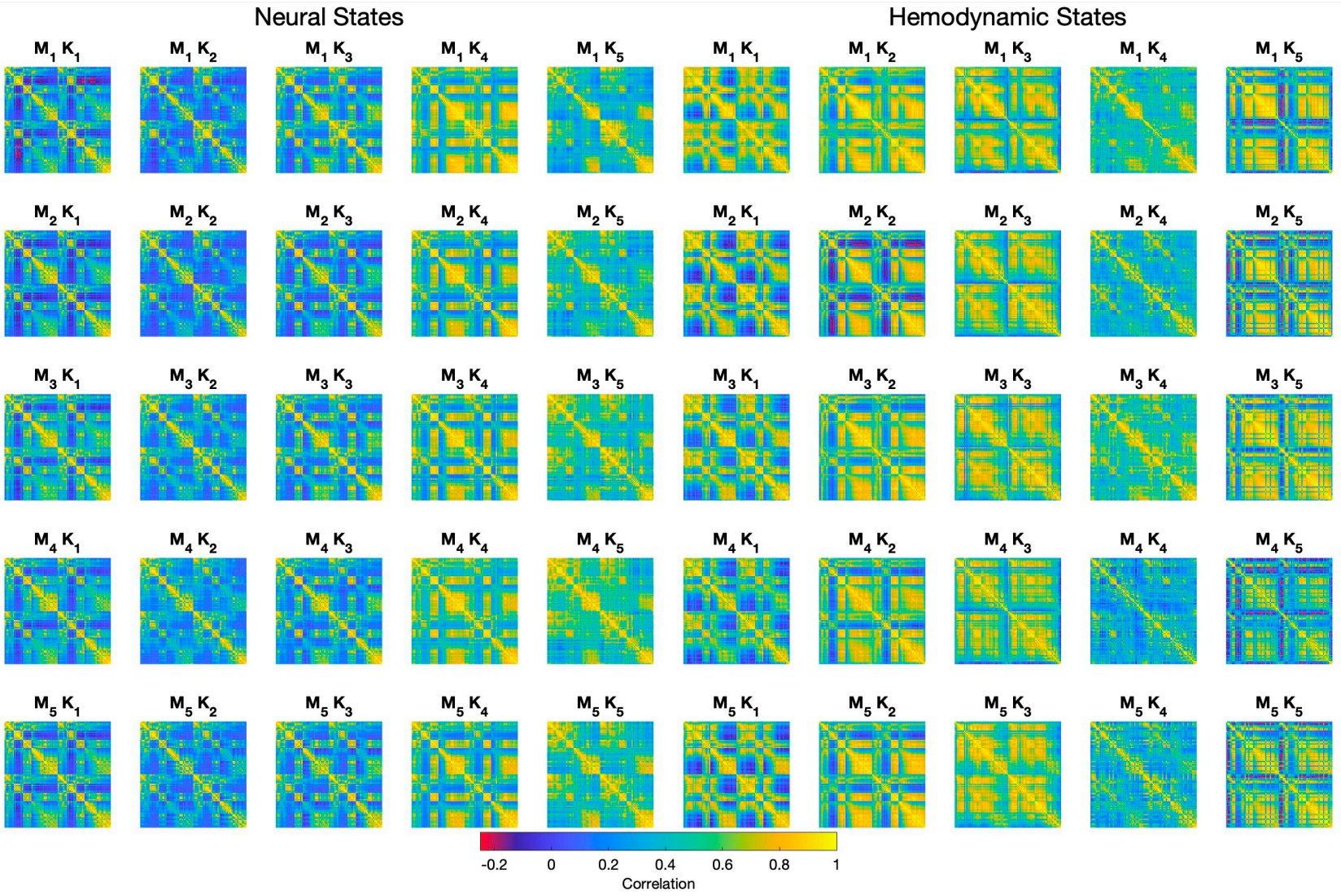
Neural States
Hemodynamic States
M1 K1
M1 K2
M1 K3
M1 K4
M1 K5
M2 K1
M2 K2
M2 K3
M2 K4
M2 K5
M3 K1
M3 K2
M3 K3
M3 K4
M3 K5
M4 K1
M4 K2
M4 K3
M4 K4
M4 K5
M5 K1
M5 K2
M5 K3
M5 K4
M5 K5
-0.2
0
0.2
0.4
0.6
0.8
1
Correlation

Figure 50 – Comparison of neural (left) and hemodynamic (right) state centroids in different mice. Each row represents neural state centroids from each subject, and each column represents one of the five states from each model. Title format: M = Mouse, K = State. (e.g. M_2K_3 = Mouse 2, State 3). These states were calculated by measuring the average FC matrix for each occurrence of a state label, but with the added grouping by mouse.

State centroids exhibited a high degree of consistency when comparing across subjects, both in neural and hemodynamic models. The most notable differences were in the slight negative correlation coefficients (red colored areas), which were of varying magnitude in neural state 1 in mouse 1, and Hemodynamic states 2 and 5. Otherwise, subject level differences were minimal, and seemed to reflect overall correlation offsets, which could be due to differences in skull thickness or optical window quality.

5.4.6 State transitions in neural and hemodynamic models

A cursory look at state transitions in the provided example sessions (Figure 42 and Figure 46) points to a meaningful pattern of state transitions in neural activity, while state transitions in the hemodynamic model seem to be slightly more disparate. While I did choose the assortment of states that best maximizes neighboring transitions, this did not guarantee that the transitions will exhibit consistency in this regard. For example, given a transition vector that is uniformly random, no assortment of states will maximize neighboring transitions, and will have an expected neighboring transition frequency of $(1 + 2 + 2 + 2 + 1)/(5 \times 5) = 32\%$ for a 5 state model.

A full compilation of all state transitions for both neural and hemodynamic FC Models is shown in Figure 50. As I hypothesized, neural transitions were much more common in neighboring states. I found that overall, 76% of transitions were to a neighboring state (i.e. the next state was either one higher or one lower). In the hemodynamic model, the transition matrix is more uniform, as 45.2% of transitions were to neighboring states.

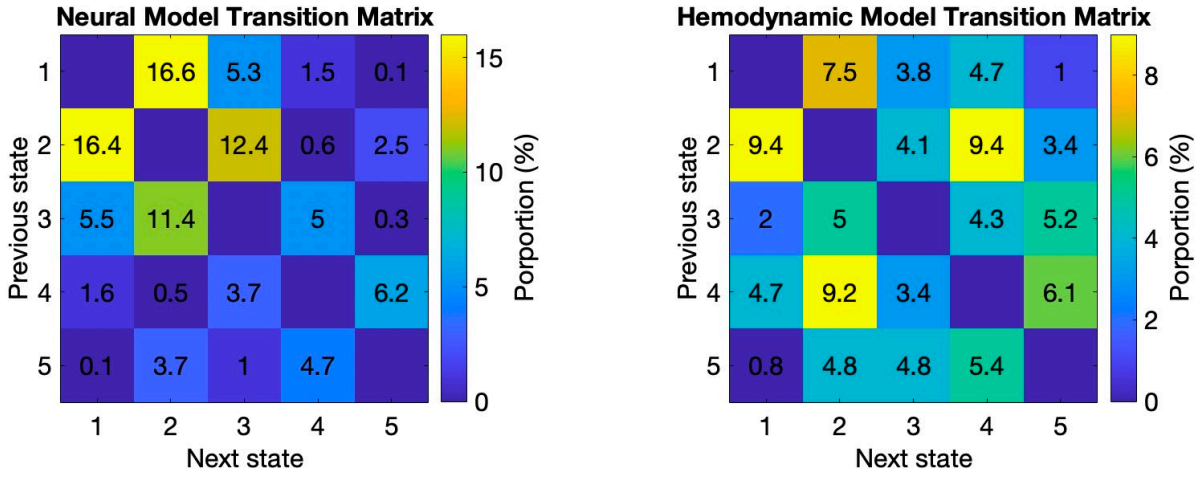

Figure 51 – Transition matrixes for hemodynamic and neural models. (Left) Neural model transition matrix. (Right) Hemodynamic model transition matrix. All numbers represent the overall proportion of transitions (e.g. all cells in each matrix sum to 100%).

These results along with our previous observations point to a key difference between neuronal and hemodynamic activity in our measurements. It seems that in general, neural activity is consistently linked to behavior, and has stereotyped transitionary dynamics that are linear. Comparatively, hemodynamic activity is less clearly linked to behavior and has transition dynamics that are less consistent and more unpredictable. This contrast is reinforced when comparing the average Euclidean distance between centroids and labels: In the neural model, FC windows had an average Euclidean distance of 12.6 (std = 5.3), while hemodynamic FC windows had a significantly higher Euclidean distance of 24.7 (std = 8.0). This implies that hemodynamic activity is more variable, and thus is harder to model comparatively. This is something that requires more investigation, as it may be an intrinsic property of the datasets, or may be due to external factors such as physiological noise only present in reflectance datasets.

5.4.7 Key differences between DFC states in neural and hemodynamic models

In Chapter 4, I noted that during locomotion and rest, I observed differences in correlation coefficients when comparing regions in visual and anterior lateral prefrontal cortex. In summary, during rest:

1. Bilateral anterior lateral prefrontal connectivity increases
2. Bilateral visual connectivity decreases
3. Connectivity between these two regions decreases

These properties were observed to reverse during rest. I compared these results to those observed in both models of neural and hemodynamic activity (Figure 51). I noted the same dynamic in Bilateral anterior lateral prefrontal connectivity, noting an overall decrease in bilateral connectivity from state 1 (low activity state) to state 5 (high activity state) (Figure 51A). When comparing bilateral visual connectivity, the results were mixed. In neural activity, there was a general positive increase in connectivity in states 2-4, while states 1 and 5 showed more moderate levels comparatively (Figure 51B). This was similar in hemodynamic activity as well. Finally, I observed a strong increase in visual-frontal connectivity from state 1 to 5 (Figure 51C) in neural activity, and a less clear but still positive trend in hemodynamics. Overall, these observations validated our previous observations in Chapter 4.

It is important to note here that these models are much more difficult to detect differences compared to our previous approach. In the previous approach, I directly compared mouse level differences, and made sure to exclude periods where behavioral activity was unpredictable and/or not as I expected. This model encompasses all data within 43 different 10-minute epochs with no prejudice, and attempts to model all data within all subjects using only 5 states, without the ability to exclude data that is not as expected. Thus, it is quite encouraging that we see

similar results when using an unsupervised clustering approach, and the level of agreement between this model and the behavior-based model further confirms that these brain regions play a key role in key changes in arousal, most notably within varying levels of rest.

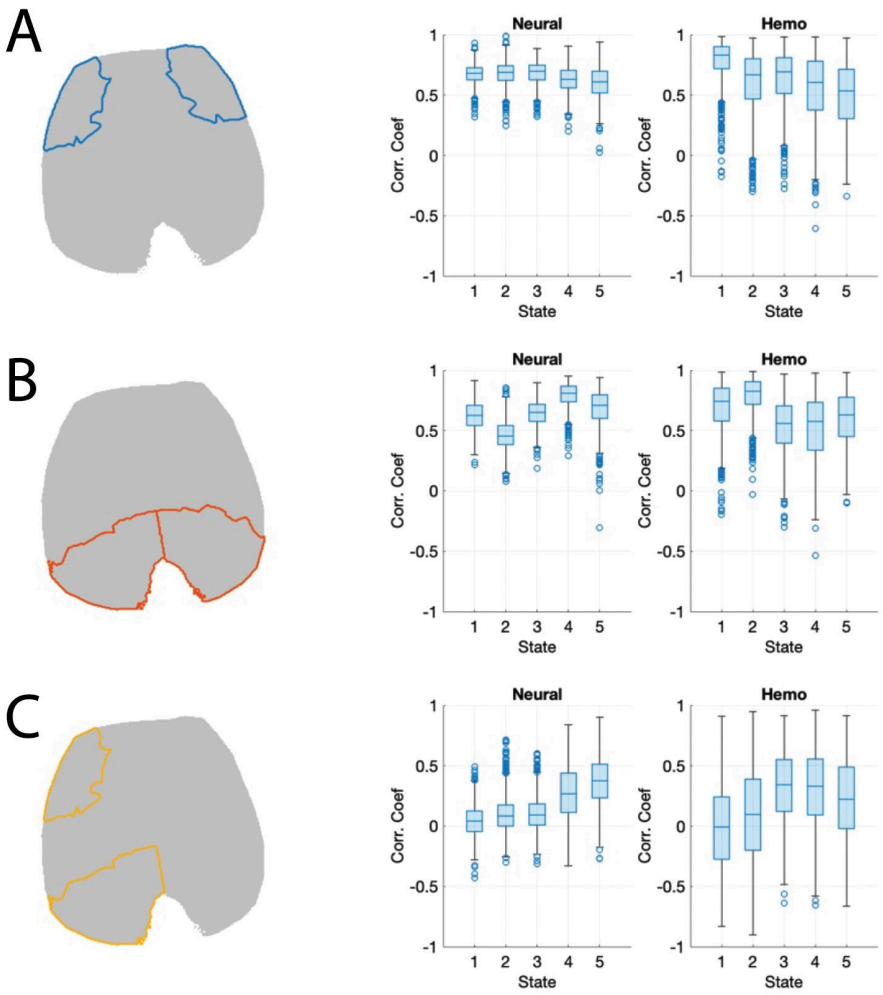

Figure 52 – Comparisons of average FC distributions between key component Groups. (A) Bilateral connectivity values for anterior lateral prefrontal cortex (FC Group B). (B) Bilateral connectivity values for visual cortex (FC group F). (C) Connectivity values for FC group B vs. FC Group F.

5.5 Discussion and Conclusions

In this chapter, I evaluated and explored the properties of Functional Connectivity in neural and hemodynamic activity. I immediately observed that FC dynamics are strikingly

different at rest and during locomotion, which motivated us to continue exploring how we can better summarize these dynamic changes using unsupervised clustering methods. By applying an unsupervised clustering technique, I found a multitude of states that persist in both neural and hemodynamic activity, and across imaging sessions and subjects.

One of the notable contrasts I observed in these states was the presence of changes in the bilateral correlation coefficients in anterior lateral prefrontal cortical areas, as well as anterior visual areas. I observed that during rest, bilateral connectivity slightly decreased in anterior lateral prefrontal regions. Further, the connectivity between these regions was drastically lower at rest compared to during locomotion. These observations were consistent in neural and hemodynamic activity, leading me to conclude that these measures of Functional Connectivity changes are a property of both neural dynamics and the resulting hemodynamic response. Not only this, but these observations agree with previous behavioral FC modeling, which made the same observations when comparing periods of initial and sustained rest.

My current findings provide strong evidence that Resting State Functional Connectivity has neural origins, and hemodynamic responses are able to depict correlation patterns that track rapid changes in behavior and internal brain states such as the level of arousal or alertness. This opens up many new questions, such as how disease and/or pharmacological agents affects connectivity architecture of such spontaneous activity, and how such alternations relate to behavioral impairments. This is of course reliant on aberrant patterns of neuronal activity propagating to hemodynamic responses, a link which has not been elucidated at all, and has rather only been implicated in proxies of neural activity such as the BOLD signal.

One key question that should be addressed in future investigations is the following: Why do we see less reliable metrics of Functional Connectivity in hemodynamics? This property may

be due to the choice of window length, some sources of physiological noise, or a true nonlinearity in the connections between neuronal and hemodynamic fluctuations. Moreover, the high-dimensional nature of these FC measures may present some difficulties when attempting to cluster many windows into distinct groups. The use of regularization techniques such as those employed in (Allen et al., 2014), are theorized to reduce the dimensionality of FC matrices, allowing for increased efficiency in clustering algorithms. Additionally, the use of superior clustering methodologies, such as fuzzy clustering, gaussian mixture modeling, or even forms of recursive neural networks may prove to better separate and identify shifts in the dynamic organization of brain activity.

6 Chapter 6: Conclusions and Future Work

This work aimed to expand knowledge of Dynamic Functional Connectivity using simultaneous measurements of neural activity and blood flow in the awake, behaving mouse. By utilizing a fast, multichannel wide field imaging system combined with awake behavioral monitoring, I interrogated these questions using advanced imaging hardware/software as well as custom analysis routines.

Analysis of resting state neural and hemodynamic activity revealed that cortical dynamics undergo drastic moment to moment shifts in FC dynamics. These shifts can be shown to coincide with changes in behavioral measures such as movement, whisking and pupil dynamics. These results also indicate that rs-dFC has neural origins, and hemodynamic responses depict correlation patterns that tracks these rapid changes in behavior. Based on these observations, I hypothesize that these shifts are related to internal brain states such as the level of arousal or alertness.

6.1.1 Wide Field Optical Mapping as a probe of pan-cortical neurological signals

In Chapter 1, I laid the groundwork for the current questions and challenges when considering neurological measurements, particularly in the context of human fMRI. Our current understanding of brain activity in fMRI recordings is limited by the inferred changes in BOLD signal, which can be considered a proxy for neural activity. I identified WFOM as an ideal candidate to investigate the underlying neural changes and associated hemodynamic activity, as it enables simultaneous measurement of neural and hemodynamic activity. Additionally, I made improvements to the WFOM system by integrating a behavioral monitoring system, which when combined with pretrained deep learning tools such as DeepLabCut (Mathis et al., 2018) allows for automated behavioral tracking with minimal manual annotations.

The usage of DeepLabCut opened up additional questions I addressed in this work, namely the associated dynamic changes in Functional Connectivity with respect to behavior. These questions helped shape the larger conclusions concerning behavioral activity and its inherent connection to brain dynamics, especially when it comes to transitional states such as movement and arousal changes.

6.1.2 Decomposition of wide field neural and hemodynamic datasets

The large amount of data collected using WFOM necessitated an efficient, repeatable methodology for decomposing, analyzing and eventually visualizing large scale changes in FC dynamics. By utilizing K-means clustering decomposition in combination with inherent knowledge about the architecture of cortical dynamics, I developeded a detailed map of the mouse cortex, which showed a high degree of consistency across subjects. This process reduced the feature space of a given dataset from hundreds of thousands of individual timecourses (e.g. pixels) to 92 in total. This analytical approach enhanced understanding of these deeply complex signals, and provided a way to compare dynamics across subjects for statistical analysis.

6.1.3 Dynamic changes in FC and behavior

Next, I examined the dynamic correlation structure of neural activity in the brain of awake, spontaneously behaving mice using simultaneous wide-field optical imaging of both neural and hemodynamic activity. I found that neural signals exhibited patterns of correlations with a rich dynamic structure, and the variations in correlation patterns were coupled to mouse behavior. I noted that locomotion caused a global synchronization across cortex, and the fluctuating correlations during ‘rest’, when mice were not running, were explained by ongoing arousal fluctuations. In addition, examining the correlation structure of hemodynamic responses corresponding to neural activity revealed that although the hemodynamics representations were

not exactly identical to the neural patterns, they did recapitulate the differences between brain states and their relationship with behavior and arousal level. Finally, I pinpointed a brain region located in the anterior lateral frontal cortex, the correlation patterns of which were found to exhibit dynamic changes when switching between high and low arousal. I found that the neural activity of the left and right anterior lateral frontal cortices was less synchronized during running compared with sustained rest. This decreased connectivity within the anterior lateral frontal regions (prefrontal cortex) during active behaviors resembles the default mode network (DMN) in human, the connectivity of which decreases during goal-directed and attention-demanding tasks (Mantini et al., 2007). Intriguingly, previous work, using resting-state fMRI in both rats (Lu et al., 2012) and mice (White et al., 2011), and wide-field voltage sensitive dye imaging in mice (Chan et al., 2015), has suggested the prefrontal cortex as one of the major DMN hubs. For the visual cortex, I observed an opposite effect. That is the visual cortex exhibited greater bilateral synchrony during locomotion rather than rest.

6.1.4 Pupil size and DFC states

To assess arousal in awake, behaving mice, I used pupillometry to estimate pupil size. One of the first observations I made during preliminary experiments was that pupil size rapidly changes during wakeful rest and locomotion. These rapid dilations of the pupil have been previously observed to be tightly coupled to changes in brain states such as arousal level (Vinck et al., 2015). Right after locomotion offset, pupil size decreases gradually rather than quickly. Nevertheless, pupil size continues to fluctuate during rest once it returns to its baseline. I could identify two distinct resting states that were associated to the arousal level. The initial rest, which occurred right after locomotion offset, and the sustained rest, which was defined when the pupil returned to its baseline. The trial-level results of our non-negative least squares model showed

that the coefficients of the initial and sustained rest reciprocally fluctuated when the animals were not running, suggesting shifts between the resting states when animals are at wakeful rest. Furthermore, the positive correlations between the initial-rest coefficients and pupil size and negative correlations between the sustained-rest coefficients and pupil size are indicative of switching between high and low arousal.

6.1.5 Prefrontal cortex and arousal

Over a temporal segment of 10 seconds, comparing the correlation structures of the brain during locomotion and the initial rest (right after locomotion offset), I noted the anterior lateral frontal cortex (prefrontal cortex) was less synchronized with other brain regions**.** Comparing the sustained rest, which is representative of low arousal, with the initial rest, which is associated with higher arousal during rest, I found that the prefrontal cortex became even more desynchronized with other brain regions, especially posterior areas. This finding suggests a possible role for the prefrontal cortex in arousal. Functional connections between cortical brain regions are essential for integrating information and consciousness (Alkire et al., 2008). Using both EEG in humans and local field potential in rats, previous work showed that anesthesia disrupts the frontal-posterior and frontal-parietal synchronization of neural activity (Imas et al., 2006; John et al., 2001; Lee et al., 2012). The global synchronization that I observed during locomotion may be suggestive of cortical integration associated with high arousal needed for performing a complex, coordinated behavior such as running. On the other hand, the decreased interactions between brain regions, specifically between the prefrontal cortex and posterior regions, may manifest the lower integration and lower arousal needed during wakeful rest. Additionally, evidence from circuit and neurochemistry studies converges to suggest that mouse prefrontal cortex has a central role in modulating the level of arousal (Garcia-Junco-Clemente et

al., 2017; Van Dort et al., 2009; Zhang et al., 2020). Taken together, it can be speculated that the prefrontal cortex is an important brain region in regulating arousal in the mouse.

6.1.6 Neural origins of fMRI brain states

One of the core discoveries of this work was an association between ongoing changes in correlation patterns of neural jRGECO signals and overt behavior such as locomotion or endogenous brain states such as arousal level, showing that correlation patterns of neural signals encode behavior and arousal level. More importantly, I showed that the hemodynamic signals were also able to capture the behavioral relevance of the underlying neural correlation patterns. Over the last decade, fMRI resting-state data has drawn special attention owing to its promising role in better understanding functional organization of the brain and developing fMRI-based biomarkers of neurological and psychiatric disorders (Khalili-Mahani et al., 2017). Previous work using fMRI rs-DFC has shown that spontaneous fluctuations in the blood oxygenation level dependent signal, a proxy for neural activity, are dynamically coherent (Calhoun et al., 2014; Fox et al., 2005; Gonzalez-Castillo et al., 2014). The origin of such ongoing time-varying synchrony, however, has been the subject of debate. A recent study suggests that shifts in underling mental processes or brain states may drive changes in FC captured by fMRI.

Our current findings provide strong evidence that rs-dFC has neural origins, and hemodynamic responses are able to depict correlation patterns that tracks rapid changes in behavior and internal brain states such as the level of arousal or alertness. One question still outstanding is how disease affects connectivity architecture of such spontaneous activity and how such alternations relate to behavioral impairments. More importantly, how much of the aberrant patterns can be captured by hemodynamic signals. As of now, previous fMRI rs-dFC studies have not been consistent in depicting reliable pathological patterns. One possible

explanation can be that dynamic functional connectivity may capture differing transitions in moment-to-moment brain states rather than a generic aberrant pathological pattern. Since at the moment of fMRI scanning brain states such as alertness, mind wandering, or motor intents could be different between patients (particularly noting that an fMRI resting-state scan itself is an intense adventure and challenge for anyone, as in the case of a head fixed mouse), the structure of correlation patterns may mostly reflect how patients adjust to and accommodate the situation. Future studies are necessary to further investigate this speculation. Current study offers an excellent framework to better understand the brain and its diseases.

6.1.7 Analysis of dynamic FC fluctuations in new experimental paradigms

A preliminary experiment was carried out to assess dynamic FC changes during periods of sleep and wakefulness. To accomplish this, animals were head fixed in a WFOM system similar to all other experiments, and were first imaged while awake for 30 minutes. Then, mice were administered medetomidine anesthesia (Virtanen, 1989) and imaged for an additional 30 minutes while anesthetized. Then, mice were injected with a reversal agent (Virtanen, 1989), and imaged for 20 more minutes during anesthetic recovery. After imaging for both awake and

anesthetized experiments, mice were removed from the imaging rig, and returned to their home cage.

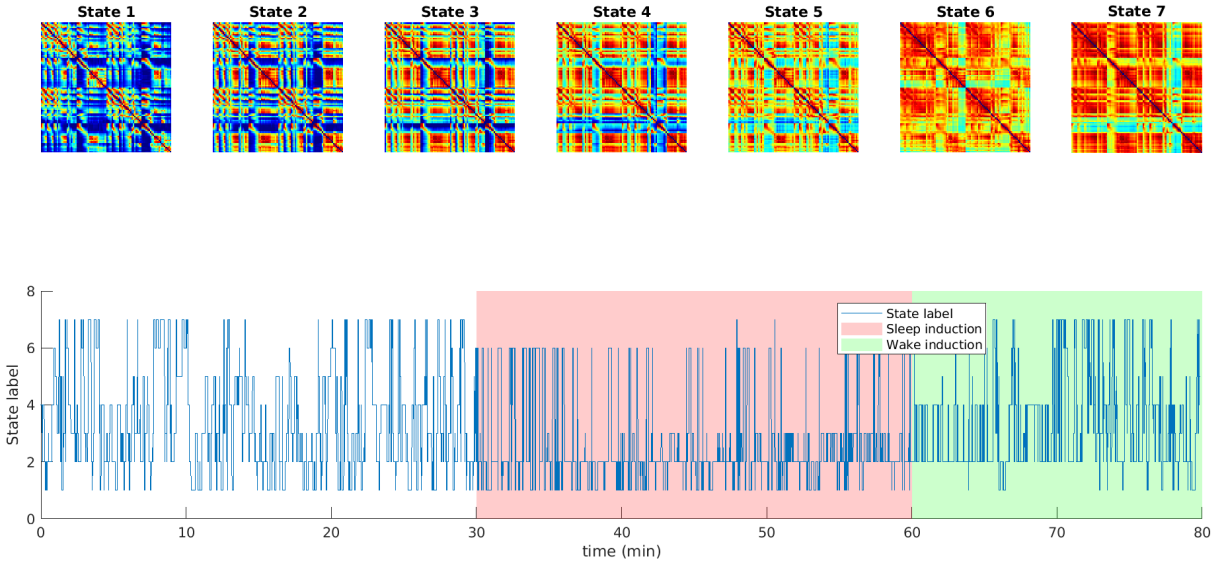

Figure 53 – Analysis of brain state during sleep. (Top) Brain states extracted from awake imaging sessions using K-means clustering (K=7). (Middle) State vector during sleep induction experiment. Red shaded area represents a 30-minute period of imaging during anesthesia. Green shaded area represents a 20-minute period of awake imaging after anesthesia reversal.

DFC analysis was carried out similar to what was described in Chapter 5, by clustering 10 second windowed FCs into 7 states. Then, state vectors were calculated in a similar manner to previous analysis, by measuring the Euclidean distance from raw FC windows to state centroids.

The results for one experiment are summarized in Figure 53. It was observed that during the initial awake imaging period, the state vector varied between one of the seven states throughout the 30 minutes of imaging. However, during the sleep induction period, state variability was noticeably reduced, oscillating between 3-4 particular states rather than all 7. This reduction in state variability was reversed soon after anesthesia reversal, indicating that state variability may be reduced during sleep, and is quickly returned to normal variability upon waking.

This experiment is just one example of many that could be explored to better understand the relationship between brain state and various physiological states. Changes in DFC states have already been used as a marker of some diseases such as Dementia in Parkinson's disease (Fiorenzato et al., 2019), Schizophrenia and Autism (Rabany et al., 2019). The use of this approach to reduce highly complex datasets to a summary vector representing a repeatable, stereotyped brain state allows for easily interpretable results, which could lead to a better understanding of the intricate dynamic processes that are modified by disease, drug interactions, and other factors.

As of now, DFC studies in humans and animals are still in their infancy, as we have just begun to scratch the surface of understanding the complex architecture of the brain, and how the myriad functional connections play a role in our mood, thought patterns, and quality of life. This work has made a small but meaningful contribution to answering these questions, and offers an excellent framework to better understand and investigate Dynamic Functional Connectivity through the lens of direct neural and hemodynamic recordings.

Bibliography

Adrian, E.D., 1954. The basis of sensation: Some recent studies of olfaction. Br. Med. J. 1, 287–290. https://doi.org/10.1136/bmj.1.4857.287

Akerboom, J., Calderón, N.C., Tian, L., Wabnig, S., Prigge, M., Tolö, J., Gordus, A., Orger, M.B., Severi, K.E., Macklin, J.J., Patel, R., Pulver, S.R., Wardill, T.J., Fischer, E., Schüler, C., Chen, T.W., Sarkisyan, K.S., Marvin, J.S., Bargmann, C.I., Kim, D.S., Kügler, S., Lagnado, L., Hegemann, P., Gottschalk, A., Schreiter, E.R., Looger, L.L., 2013. Genetically encoded calcium indicators for multi-color neural activity imaging and combination with optogenetics. Front. Mol. Neurosci. 0, 2. https://doi.org/10.3389/FNMOL.2013.00002/BIBTEX

Alkire, M.T., Hudetz, A.G., Tononi, G., 2008. Consciousness and anesthesia. Science 322, 876–880. https://doi.org/10.1126/science.1149213

Allen, E.A., Damaraju, E., Plis, S.M., Erhardt, E.B., Eichele, T., Calhoun, V.D., 2014. Tracking whole-brain connectivity dynamics in the resting state. Cereb. Cortex 24, 663–676. https://doi.org/10.1093/cercor/bhs352

Andrews-Hanna, J.R., 2012. The brain's default network and its adaptive role in internal mentation. Neuroscientist 18, 251–270. https://doi.org/10.1177/1073858411403316

Beckmann, C.F., DeLuca, M., Devlin, J.T., Smith, S.M., 2005. Investigations into resting-state connectivity using independent component analysis. Philos. Trans. R. Soc. B Biol. Sci. 360, 1001–1013. https://doi.org/10.1098/rstb.2005.1634

Benisty, H., Moberly, A.H., Lohani, S., Barson, D., Coifman, R.R., Mishne, G., Cardin, J.A., Higley, M.J., 2021. Rapid fluctuations in functional connectivity of cortical networks encode spontaneous behavior. https://doi.org/10.1101/2021.08.15.456390

Berry, M.W., Browne, M., Langville, A.N., Pauca, V.P., Plemmons, R.J., 2007. Algorithms and applications for approximate nonnegative matrix factorization. Comput. Stat. Data Anal. 52, 155–173. https://doi.org/10.1016/j.csda.2006.11.006

Bhaskara, S., Sakorikar, T., Chatterjee, S., Shabari Girishan, K.V., Pandya, H.J., 2022. Recent advancements in Micro-engineered devices for surface and deep brain animal studies: A review. Sens. Bio-Sens. Res. 36, 100483. https://doi.org/10.1016/j.sbsr.2022.100483

Biswal, B., Yetkin, F.Z., Haughton, V.M., Hyde, J.S., 1995. Functional connectivity in the motor cortex of resting human brain using echo-planar mri. Magn. Reson. Med. 34, 537–541. https://doi.org/10.1002/MRM.1910340409

Bouchard, M.B., Chen, B.R., Burgess, S.A., Hillman, E.M.C., 2009. Ultra-fast multispectral optical imaging of cortical oxygenation, blood flow, and intracellular calcium dynamics. Opt. Express 17, 15670–15678. https://doi.org/10.1364/OE.17.015670

Bouchard, M.B., Voleti, V., Mendes, C.S., Lacefield, C., Grueber, W.B., Mann, R.S., Bruno, R.M., Hillman, E.M.C., 2015. Swept confocally-aligned planar excitation (SCAPE) microscopy for high-speed volumetric imaging of behaving organisms. Nat. Photonics 9, 113–119. https://doi.org/10.1038/nphoton.2014.323

Britz, J., Van De Ville, D., Michel, C.M., 2010. BOLD correlates of EEG topography reveal rapid resting-state network dynamics. NeuroImage 52, 1162–1170. https://doi.org/10.1016/j.neuroimage.2010.02.052

Bro, R., De Jong, S., 1997. A fast non-negativity-constrained least squares algorithm. J. Chemom. 11, 393–401. https://doi.org/10.1002/(SICI)1099-128X(199709/10)11:5<393::AID-CEM483>3.0.CO;2-L

Brookes, M.J., Hale, J.R., Zumer, J.M., Stevenson, C.M., Francis, S.T., Barnes, G.R., Owen, J.P., Morris, P.G., Nagarajan, S.S., 2011a. Measuring functional connectivity using MEG: Methodology and comparison with fcMRI. NeuroImage 56, 1082–1104. https://doi.org/10.1016/j.neuroimage.2011.02.054

Brookes, M.J., Woolrich, M., Luckhoo, H., Price, D., Hale, J.R., Stephenson, M.C., Barnes, G.R., Smith, S.M., Morris, P.G., 2011b. Investigating the electrophysiological basis of resting state networks using magnetoencephalography. Proc. Natl. Acad. Sci. 108, 16783–16788. https://doi.org/10.1073/pnas.1112685108

Buckner, R.L., Krienen, F.M., Yeo, B.T.T., 2013. Opportunities and limitations of intrinsic functional connectivity MRI. Nat. Neurosci. 16, 832–837. https://doi.org/10.1038/nn.3423

Calhoun, V.D., Miller, R., Pearlson, G., Adalı, T., 2014. The Chronnectome: Time-Varying Connectivity Networks as the Next Frontier in fMRI Data Discovery. Neuron 84, 262–274. https://doi.org/10.1016/j.neuron.2014.10.015

Chen, Q., Cichon, J., Wang, W., Qiu, L., Lee, S.-J.R., Campbell, N.R., Destefino, N., Goard, M.J., Fu, Z., Yasuda, R., Looger, L.L., Arenkiel, B.R., Gan, W.-B., Feng, G., 2012. Imaging neural activity using Thy1-GCaMP transgenic mice. Neuron 76, 297–308. https://doi.org/10.1016/j.neuron.2012.07.011

Chen, T.W., Li, N., Daie, K., Svoboda, K., 2017. A Map of Anticipatory Activity in Mouse Motor Cortex. Neuron 94, 866-879.e4. https://doi.org/10.1016/j.neuron.2017.05.005

Dana, H., Mohar, B., Sun, Y., Narayan, S., Gordus, A., Hasseman, J.P., Tsegaye, G., Holt, G.T., Hu, A., Walpita, D., Patel, R., Macklin, J.J., Bargmann, C.I., Ahrens, M.B., Schreiter, E.R., Jayaraman, V., Looger, L.L., Svoboda, K., Kim, D.S., 2016. Sensitive red protein

calcium indicators for imaging neural activity. eLife 5, e12727. https://doi.org/10.7554/eLife.12727

Dana, H., Novak, O., Guardado-Montesino, M., Fransen, J.W., Hu, A., Borghuis, B.G., Guo, C., Kim, D.S., Svoboda, K., 2018. Thy1 transgenic mice expressing the red fluorescent calcium indicator jRGECO1a for neuronal population imaging in vivo. PLOS ONE 13, e0205444. https://doi.org/10.1371/journal.pone.0205444

de Pasquale, F., Della Penna, S., Snyder, A.Z., Lewis, C., Mantini, D., Marzetti, L., Belardinelli, P., Ciancetta, L., Pizzella, V., Romani, G.L., Corbetta, M., 2010. Temporal dynamics of spontaneous MEG activity in brain networks. Proc. Natl. Acad. Sci. U. S. A. 107, 6040–6045. https://doi.org/10.1073/pnas.0913863107

Di, X., Biswal, B.B., 2015. Dynamic brain functional connectivity modulated by resting-state networks. Brain Struct. Funct. 220, 37–46. https://doi.org/10.1007/s00429-013-0634-3

Dunn, A.K., Devor, A., Bolay, H., Andermann, M.L., Moskowitz, M.A., Dale, A.M., Boas, D.A., 2003. Simultaneous imaging of total cerebral hemoglobin concentration, oxygenation, and blood flow during functional activation. Opt. Lett. 28, 28. https://doi.org/10.1364/ol.28.000028

FFmpeg README, 2022.

Fiorenzato, E., Strafella, A.P., Kim, J., Schifano, R., Weis, L., Antonini, A., Biundo, R., 2019. Dynamic functional connectivity changes associated with dementia in Parkinson's disease. Brain 142, 2860–2872. https://doi.org/10.1093/brain/awz192

Fox, M.D., Snyder, A.Z., Vincent, J.L., Corbetta, M., Essen, D.C.V., Raichle, M.E., 2005. The human brain is intrinsically organized into dynamic, anticorrelated functional networks. Proc. Natl. Acad. Sci. U. S. A. 102, 9673–9678. https://doi.org/10.1073/pnas.0504136102

Friedman, J.H., 1997. On bias, variance, 0/1-loss, and the curse-of-dimensionality. Data Min. Knowl. Discov. 1, 55–77.

Fukushima, M., Betzel, R.F., He, Y., van den Heuvel, M.P., Zuo, X.-N., Sporns, O., 2018. Structure–function relationships during segregated and integrated network states of human brain functional connectivity. Brain Struct. Funct. 223, 1091–1106. https://doi.org/10.1007/s00429-017-1539-3

Garcia-Junco-Clemente, P., Ikrar, T., Tring, E., Xu, X., Ringach, D.L., Trachtenberg, J.T., 2017. An inhibitory pull-push circuit in frontal cortex. Nat. Neurosci. 20, 389–392. https://doi.org/10.1038/nn.4483

Giovannucci, A., Friedrich, J., Gunn, P., Kalfon, J., Koay, S.A., Taxidis, J., Najafi, F., Gauthier, J.L., Zhou, P., Tank, D.W., Chklovskii, D., Pnevmatikakis, E.A., 2018. CalmAn: An open source tool for scalable Calcium Imaging data Analysis. bioRxiv 339564. https://doi.org/10.1101/339564

Gonzalez-Castillo, J., Handwerker, D.A., Robinson, M.E., Hoy, C.W., Buchanan, L.C., Saad, Z.S., Bandettini, P.A., 2014. The spatial structure of resting state connectivity stability on the scale of minutes. Front. Neurosci. 8.

Grinvald, A., Lieke, E., Frostig, R.D., Gilbert, C.D., Wiesel, T.N., 1986. Functional architecture of cortex revealed by optical imaging of intrinsic signals. Nature 324, 361–364. https://doi.org/10.1038/324361a0

Hadjipanayis, C.G., Jiang, H., Roberts, D.W., Yang, L., 2011. Current and Future Clinical Applications for Optical Imaging of Cancer: From Intraoperative Surgical Guidance to Cancer Screening. Semin. Oncol., Molecular Imaging in Oncology 38, 109–118. https://doi.org/10.1053/j.seminoncol.2010.11.008

Hartigan, J.A., Wong, M.A., 1979. Algorithm AS 136: A K-Means Clustering Algorithm. Appl. Stat. 28, 100. https://doi.org/10.2307/2346830

Heuvel, M.P. van den, Pol, H.E.H., 2010. Exploring the brain network: A review on resting-state fMRI functional connectivity. Eur. Neuropsychopharmacol. 20, 519–534. https://doi.org/10.1016/j.euroneuro.2010.03.008

Hillman, E.M.C., 2014. Coupling mechanism and significance of the BOLD signal: a status report. Annu. Rev. Neurosci. 37, 161–181. https://doi.org/10.1146/annurev-neuro-071013-014111

Hillman, E.M.C., 2007. Optical brain imaging in vivo: techniques and applications from animal to man. J. Biomed. Opt. 12, 051402. https://doi.org/10.1117/1.2789693

Hsu, L.M., Liang, X., Gu, H., Brynildsen, J.K., Stark, J.A., Ash, J.A., Lin, C.P., Lu, H., Rapp, P.R., Stein, E.A., Yang, Y., 2016. Constituents and functional implications of the rat default mode network. Proc. Natl. Acad. Sci. U. S. A. 113, E4541–E4547. https://doi.org/10.1073/pnas.1601485113

Hutchison, R.M., Womelsdorf, T., Allen, E.A., Bandettini, P.A., Calhoun, V.D., Corbetta, M., Penna, S.D., Duyn, J.H., Glover, G.H., Gonzalez-Castillo, J., Handwerker, D.A., Keilholz, S., Kiviniemi, V., Leopold, D.A., Pasquale, F. de, Sporns, O., Walter, M., Chang, C., 2013. Dynamic functional connectivity: Promise, issues, and interpretations. NeuroImage 80, 360–378. https://doi.org/10.1016/J.NEUROIMAGE.2013.05.079

Ikegaya, Y., Aaron, G., Cossart, R., Aronov, D., Lampl, I., Ferster, D., Yuste, R., 2004. Synfire Chains and Cortical Songs: Temporal Modules of Cortical Activity. Science 304, 559–564. https://doi.org/10.1126/science.1093173

Imas, O.A., Ropella, K.M., Wood, J.D., Hudetz, A.G., 2006. Isoflurane disrupts anterio-posterior phase synchronization of flash-induced field potentials in the rat. Neurosci. Lett. 402, 216–221. https://doi.org/10.1016/j.neulet.2006.04.003

Jöbsis, F.F., 1977. Noninvasive, infrared monitoring of cerebral and myocardial oxygen sufficiency and circulatory parameters. Science 198, 1264–1267. https://doi.org/10.1126/science.929199

John, E.R., Prichep, L.S., Kox, W., Valdés-Sosa, P., Bosch-Bayard, J., Aubert, E., Tom, M., diMichele, F., Gugino, L.D., 2001. Invariant Reversible QEEG Effects of Anesthetics. Conscious. Cogn. 10, 165–183. https://doi.org/10.1006/ccog.2001.0507

Kabra, M., Robie, A.A., Rivera-Alba, M., Branson, S., Branson, K., 2013. JAABA: Interactive machine learning for automatic annotation of animal behavior. Nat. Methods 10, 64–67. https://doi.org/10.1038/nmeth.2281

Keilholz, S.D., Magnuson, M.E., Pan, W.-J., Willis, M., Thompson, G.J., 2013. Dynamic properties of functional connectivity in the rodent. Brain Connect. 3, 31–40. https://doi.org/10.1089/brain.2012.0115

Khalili-Mahani, N., Rombouts, S.A.R.B., van Osch, M.J.P., Duff, E.P., Carbonell, F., Nickerson, L.D., Becerra, L., Dahan, A., Evans, A.C., Soucy, J.-P., Wise, R., Zijdenbos, A.P., van Gerven, J.M., 2017. Biomarkers, designs, and interpretations of resting-state fMRI in translational pharmacological research: A review of state-of-the-Art, challenges, and opportunities for studying brain chemistry. Hum. Brain Mapp. 38, 2276–2325. https://doi.org/10.1002/hbm.23516

Kozberg, M.G., Chen, B.R., DeLeo, S.E., Bouchard, M.B., Hillman, E.M.C., 2013. Resolving the transition from negative to positive blood oxygen level-dependent responses in the

developing brain. Proc. Natl. Acad. Sci. U. S. A. 110, 4380–4385. https://doi.org/10.1073/pnas.1212785110

Laufs, H., 2010. Multimodal analysis of resting state cortical activity: what does EEG add to our knowledge of resting state BOLD networks? NeuroImage 52, 1171–1172. https://doi.org/10.1016/j.neuroimage.2010.05.034

Lee, D.D., Seung, H.S., 1999. Learning the parts of objects by non-negative matrix factorization. Nature 401, 788–791. https://doi.org/10.1038/44565

Lee, M.H., Hacker, C.D., Snyder, A.Z., Corbetta, M., Zhang, D., Leuthardt, E.C., Shimony, J.S., 2012. Clustering of resting state networks. PLoS ONE 7, e40370. https://doi.org/10.1371/journal.pone.0040370

Liu, T.T., Nalci, A., Falahpour, M., 2017. The Global Signal in fMRI: Nuisance or Information? NeuroImage 150, 213–229. https://doi.org/10.1016/j.neuroimage.2017.02.036

Lu, H., Zou, Q., Gu, H., Raichle, M.E., Stein, E.A., Yang, Y., 2012. Rat brains also have a default mode network. Proc. Natl. Acad. Sci. 109, 3979–3984. https://doi.org/10.1073/pnas.1200506109

Ma, Y., Shaik, M.A., Kim, S.H., Kozberg, M.G., Thibodeaux, D.N., Zhao, H.T., Yu, H., Hillman, E.M.C., 2016. Wide-field optical mapping of neural activity and brain haemodynamics: Considerations and novel approaches. Philos. Trans. R. Soc. B Biol. Sci. 371. https://doi.org/10.1098/rstb.2015.0360

Ma, Ying, Shaik, M.A., Kozberg, M.G., Kim, S.H., Portes, J.P., Timerman, D., Hillman, E.M.C., 2016. Resting-state hemodynamics are spatiotemporally coupled to synchronized and symmetric neural activity in excitatory neurons. Proc. Natl. Acad. Sci. U. S. A. 113, E8463–E8471. https://doi.org/10.1073/pnas.1525369113

Mantini, D., Perrucci, M.G., Del Gratta, C., Romani, G.L., Corbetta, M., 2007. Electrophysiological signatures of resting state networks in the human brain. Proc. Natl. Acad. Sci. 104, 13170–13175. https://doi.org/10.1073/pnas.0700668104

Mathis, A., Mamidanna, P., Cury, K.M., Abe, T., Murthy, V.N., Mathis, M.W., Bethge, M., 2018. DeepLabCut: markerless pose estimation of user-defined body parts with deep learning. Nat. Neurosci. 21, 1281–1289. https://doi.org/10.1038/s41593-018-0209-y

Menon, S.S., Krishnamurthy, K., 2019. A Comparison of Static and Dynamic Functional Connectivities for Identifying Subjects and Biological Sex Using Intrinsic Individual Brain Connectivity. Sci. Rep. 9, 5729. https://doi.org/10.1038/s41598-019-42090-4

Miyawaki, A., Llopis, J., Heim, R., McCaffery, J.M., Adams, J.A., Ikura, M., Tsien, R.Y., 1997. Fluorescent indicators for Ca2+ based on green fluorescent proteins and calmodulin. Nature 388, 882–887. https://doi.org/10.1038/42264

Montgomery, M.K., Kim, S.H., Dovas, A., Patel, K., Mela, A., Humala, N., Zhao, H.T., Thibodeaux, D.N., Shaik, M., Ma, Y., Grinband, J., Chow, D.S., Schevon, C., Hillman, E.M.C., Canoll, P., 2019. Glioma-induced alterations in neuronal activity and neurovascular coupling during disease progression. bioRxiv 763805. https://doi.org/10.1101/763805

Mulder, K.J., Mulder, J.B., 1979. Ketamine and xylazine anesthesia in the mouse. Vet. Med. Small Anim. Clin. 74, 569–570.

Mwangi, B., Tian, T.S., Soares, J.C., 2014. A review of feature reduction techniques in Neuroimaging. Neuroinformatics 12, 229–244. https://doi.org/10.1007/s12021-013-9204-3

Oh, J., Lee, C., Kaang, B.-K., 2019. Imaging and analysis of genetically encoded calcium indicators linking neural circuits and behaviors. Korean J. Physiol. Pharmacol. Off. J. Korean Physiol. Soc. Korean Soc. Pharmacol. 23, 237–249. https://doi.org/10.4196/kjpp.2019.23.4.237

Orbach, H.S., Cohen, L.B., Grinvald, A., 1985. Optical mapping of electrical activity in rat somatosensory and visual cortex. J. Neurosci. 5, 1886–1895. https://doi.org/10.1523/JNEUROSCI.05-07-01886.1985

Pal, D., Silverstein, B.H., Sharba, L., Li, D., Hambrecht-Wiedbusch, V.S., Hudetz, A.G., Mashour, G.A., 2017. Propofol, sevoflurane, and ketamine induce a reversible increase in delta-gamma and theta-gamma phase-amplitude coupling in frontal cortex of rat. Front. Syst. Neurosci. 11, 41. https://doi.org/10.3389/fnsys.2017.00041

Pascual-Marqui, R.D., Michel, C.M., Lehmann, D., 1995. Segmentation of brain electrical activity into microstates: model estimation and validation. IEEE Trans. Biomed. Eng. 42, 658–665. https://doi.org/10.1109/10.391164

Pauletto, S., Hunt, A., 2005. A comparison of audio and visual analysis of complex time-series data sets. ICAD05.

Pereira, T.D., Aldarondo, D.E., Willmore, L., Kislin, M., Wang, S.S.-H., Murthy, M., Shaevitz, J.W., 2019. Fast animal pose estimation using deep neural networks. Nat. Methods 16, 117–125. https://doi.org/10.1038/s41592-018-0234-5

Peterka, D.S., Takahashi, H., Yuste, R., 2011. Imaging Voltage in Neurons. Neuron 69, 9–21. https://doi.org/10.1016/j.neuron.2010.12.010

Pnevmatikakis, E.A., Soudry, D., Gao, Y., Machado, T.A., Merel, J., Pfau, D., Reardon, T., Mu, Y., Lacefield, C., Yang, W., Ahrens, M., Bruno, R., Jessell, T.M., Peterka, D.S., Yuste,

R., Paninski, L., 2016. Simultaneous Denoising, Deconvolution, and Demixing of Calcium Imaging Data. Neuron 89, 285. https://doi.org/10.1016/j.neuron.2015.11.037

Pratt, V., 1987. Direct least-squares fitting of algebraic surfaces. ACM SIGGRAPH Comput. Graph. 21, 145–152. https://doi.org/10.1145/37402.37420

Rabany, L., Brocke, S., Calhoun, V.D., Pittman, B., Corbera, S., Wexler, B.E., Bell, M.D., Pelphrey, K., Pearlson, G.D., Assaf, M., 2019. Dynamic functional connectivity in schizophrenia and autism spectrum disorder: Convergence, divergence and classification. NeuroImage Clin. 24, 101966. https://doi.org/10.1016/j.nicl.2019.101966

Raichle, M.E., 2015. The restless brain: how intrinsic activity organizes brain function. Philos. Trans. R. Soc. B Biol. Sci. 370, 20140172. https://doi.org/10.1098/rstb.2014.0172

Saad, Z.S., Gotts, S.J., Murphy, K., Chen, G., Jo, H.J., Martin, A., Cox, R.W., 2012. Trouble at Rest: How Correlation Patterns and Group Differences Become Distorted After Global Signal Regression. Brain Connect. 2, 25–32. https://doi.org/10.1089/brain.2012.0080

Sakoğlu, U., Pearlson, G.D., Kiehl, K.A., Wang, Y.M., Michael, A.M., Calhoun, V.D., 2010. A method for evaluating dynamic functional network connectivity and task-modulation: application to schizophrenia. Magma N. Y. N 23, 351–366. https://doi.org/10.1007/s10334-010-0197-8

Saxena, S., Kinsella, I., Musall, S., Kim, S.H., Meszaros, J., Thibodeaux, D.N., Kim, C., Cunningham, J., Hillman, E.M.C., Churchland, A., Paninski, L., 2020. Localized semi-nonnegative matrix factorization (LocaNMF) of widefield calcium imaging data. PLoS Comput. Biol. 16, 650093. https://doi.org/10.1371/journal.pcbi.1007791

Shahsavarani, Somayeh, Thibodeaux, David N., Xu, Weihao, Kim, Sharon H., Lodgher, Fatema, Yagielski, Alexis, Handwerker, Daniel, Gonzalez-Castillo, Javier, Bandettini, Peter,

Hillman, Elizabeth M. C., n.d. Cortex-wide neural dynamics predict behavioral states and provide a neural basis for resting-state dynamic functional connectivity. Nueron Rev.

Sheroziya, M., Timofeev, I., 2014. Global intracellular slow-wave dynamics of the thalamocortical system. J. Neurosci. 34, 8875–8893. https://doi.org/10.1523/JNEUROSCI.4460-13.2014

Sirotin, Y.B., Das, A., 2009. Anticipatory haemodynamic signals in sensory cortex not predicted by local neuronal activity. Nature 457, 475–479. https://doi.org/10.1038/nature07664

Stafford, J.M., Jarrett, B.R., Miranda-Dominguez, O., Mills, B.D., Cain, N., Mihalas, S., Lahvis, G.P., Lattal, K.M., Mitchell, S.H., David, S.V., Fryer, J.D., Nigg, J.T., Fair, D.A., 2014. Large-scale topology and the default mode network in the mouse connectome. Proc. Natl. Acad. Sci. U. S. A. 111, 18745–18750. https://doi.org/10.1073/pnas.1404346111

Steriade, M., Nunez, A., Amzica, F., 1993. A novel slow (< 1 Hz) oscillation of neocortical neurons in vivo: Depolarizing and hyperpolarizing components. J. Neurosci. 13, 3252–3265. https://doi.org/10.1523/jneurosci.13-08-03252.1993

Sun, R., Bouchard, M.B., Hillman, E.M.C., 2010. SPLASSH: Open source software for camera-based high-speed, multispectral in-vivo optical image acquisition. Biomed. Opt. Express 1, 385–397. https://doi.org/10.1364/BOE.1.000385

Thibodeaux, N., 2020. FLIR cameras and Python: An efficient multi-cam setup using a hardware trigger/freerun capture.

Thompson, W.H., Fransson, P., 2016. On Stabilizing the Variance of Dynamic Functional Brain Connectivity Time Series. Brain Connect. 6, 735–746. https://doi.org/10.1089/brain.2016.0454

Tort, A.B.L., Neto, W.P., Amaral, O.B., Kazlauckas, V., Souza, D.O., Lara, D.R., 2006. A simple webcam-based approach for the measurement of rodent locomotion and other behavioural parameters. J. Neurosci. Methods 157, 91–97. https://doi.org/10.1016/j.jneumeth.2006.04.005

Ts'o, D.Y., Frostig, R.D., Lieke, E.E., Grinvald, A., 1990. Functional organization of primate visual cortex revealed by high resolution optical imaging. Science 249, 417–420. https://doi.org/10.1126/science.2165630

Uddin, L.Q., 2013. Complex relationships between structural and functional brain connectivity. Trends Cogn. Sci. 17, 600–602. https://doi.org/10.1016/j.tics.2013.09.011

Van Dort, C.J., Baghdoyan, H.A., Lydic, R., 2009. Adenosine A1 and A2A Receptors in Mouse Prefrontal Cortex Modulate Acetylcholine Release and Behavioral Arousal. J. Neurosci. 29, 871–881. https://doi.org/10.1523/JNEUROSCI.4111-08.2009

Vinck, M., Batista-Brito, R., Knoblich, U., Cardin, J.A., 2015. Arousal and Locomotion Make Distinct Contributions to Cortical Activity Patterns and Visual Encoding. Neuron 86, 740–754. https://doi.org/10.1016/j.neuron.2015.03.028

Virtanen, R., 1989. Pharmacological profiles of medetomidine and its antagonist, atipamezole. Acta Vet. Scand. Suppl. 85, 29–37.

Voleti, V., Patel, K.B., Li, W., Perez Campos, C., Bharadwaj, S., Yu, H., Ford, C., Casper, M.J., Yan, R.W., Liang, W., Wen, C., Kimura, K.D., Targoff, K.L., Hillman, E.M.C., 2019. Real-time volumetric microscopy of in vivo dynamics and large-scale samples with SCAPE 2.0. Nat. Methods 16, 1054–1062. https://doi.org/10.1038/s41592-019-0579-4

White, B.R., Bauer, A.Q., Snyder, A.Z., Schlaggar, B.L., Lee, J.M., Culver, J.P., 2011. Imaging of functional connectivity in the mouse brain. PLoS ONE 6, e16322. https://doi.org/10.1371/journal.pone.0016322

Wold, S., Esbensen, K., Geladi, P., n.d. Principal Component Analysis 16.

Wu, D., Li, C., Yao, D., 2013. Scale-Free Brain Quartet: Artistic Filtering of Multi-Channel Brainwave Music. PLoS ONE 8, e64046. https://doi.org/10.1371/journal.pone.0064046

Wu, D., Li, C.Y., Yao, D.Z., 2009. Scale-free music of the brain. PLoS ONE 4, e5915. https://doi.org/10.1371/journal.pone.0005915

Xiao, D., Vanni, M.P., Mitelut, C.C., Chan, A.W., Ledue, J.M., Xie, Y., Chen, A.C.N., Swindale, N.V., Murphy, T.H., 2017. Mapping cortical mesoscopic networks of single spiking cortical or sub-cortical neurons. eLife 6. https://doi.org/10.7554/eLife.19976

Zhang, X., Baer, A.G., Price, J.M., Jones, P.C., Garcia, B.J., Romero, J., Cliff, A.M., Mi, W., Brown, J.B., Jacobson, D.A., Lydic, R., Baghdoyan, H.A., 2020. Neurotransmitter networks in mouse prefrontal cortex are reconfigured by isoflurane anesthesia. J. Neurophysiol. 123, 2285–2296. https://doi.org/10.1152/jn.00092.2020

Appendix A: The pyanthem Graphical User Interface

To share this audiovisualization method broadly I developed an open-source, Python based graphical user interface (GUI) pyanthem, which enables conversion of dynamic datasets into audiovisualizations using the same techniques described in this manuscript.

The GUI accepts data that has already been spatiotemporally unmixed, although I also provide basic code to implement dimensionality reduction of a range of data types, first by k-means clustering the data to obtain temporal ROIs H, and then by performing nonnegative least squares to obtain spatial components W. The output of the GUI is a fully merged movie with audio soundtrack, although the package can also output renderings at intermediate steps, such as the visualization, or MIDI format outputs for use in external audio programs. Basic features and functions are explained below. Full instructions, along with an installation guide can be found here: https://github.com/nicthib/pyanthem. Supplemental Figure 1 shows a screen-shot of the GUI and basic functionality is detailed briefly below. All GUI components are referred to using **bold text.**

A 1.1 Data import

After installing and opening pyanthem, a dataset in the .mat or .h5 format can be loaded using the **File** dialog (Supplemental Figure 1A). The file should at least include an H (n x t) variable, for audio-only output, or both H (n x t) and W (s_x x s_y x n) variables for audiovisualization. An additional single float variable will be interpreted as the data's frame rate. Once loaded, video and audio previews are displayed in the bottom and right panels using default settings (Supplemental Figure 1D,E).

A 1.2 Parameter tuning

A variety of video and audio parameters can be changed and previewed using the associated panes in the top left area of the GUI. Parameter adjustments are made in one of the three parameter categories: **File Parameters**, **Video Parameters**, and **Audio Parameters** (Supplemental Figure 1B). The GUI permits selection of the color-scale for visualization including component order, as well as background subtraction and audio digitization settings. The musical scale and instrument to be rendered can also be selected. Changes are reflected in the plots when clicking the **Update** button on the middle left side of the GUI window, and most errors will be indicated in the status box next to the **Update** button (Supplemental Figure 1C). Configurations can be saved and re-loaded for application to multiple datasets.

Spatial components and their dynamic merge can be previewed by using the scroll bar below the **Video** preview plot (Supplemental Figure 1D). Audio components can also be previewed using the **Preview** button in the **Audio Parameters** column. The pyanthem GUI comes with 3 installed instruments to choose from – Grand Piano, Electric Piano, and Strings. pyanthem can only render audio using one instrument and dataset at a time, but it is possible to merge together multiple separately generated audio streams using included functions. Data can also be saved in MIDI format for more complex rendering in a 3rd party VST such as Garage Band or REAPER.

A 1.3 File output and merging

Files can be output individually using **Save → Audio** or **Save → Video** (Supplemental Figure 1A). These output files can then be merged using **Save → Merge A/V**.

Separately generated audio and video streams can also be merged using command line functions.

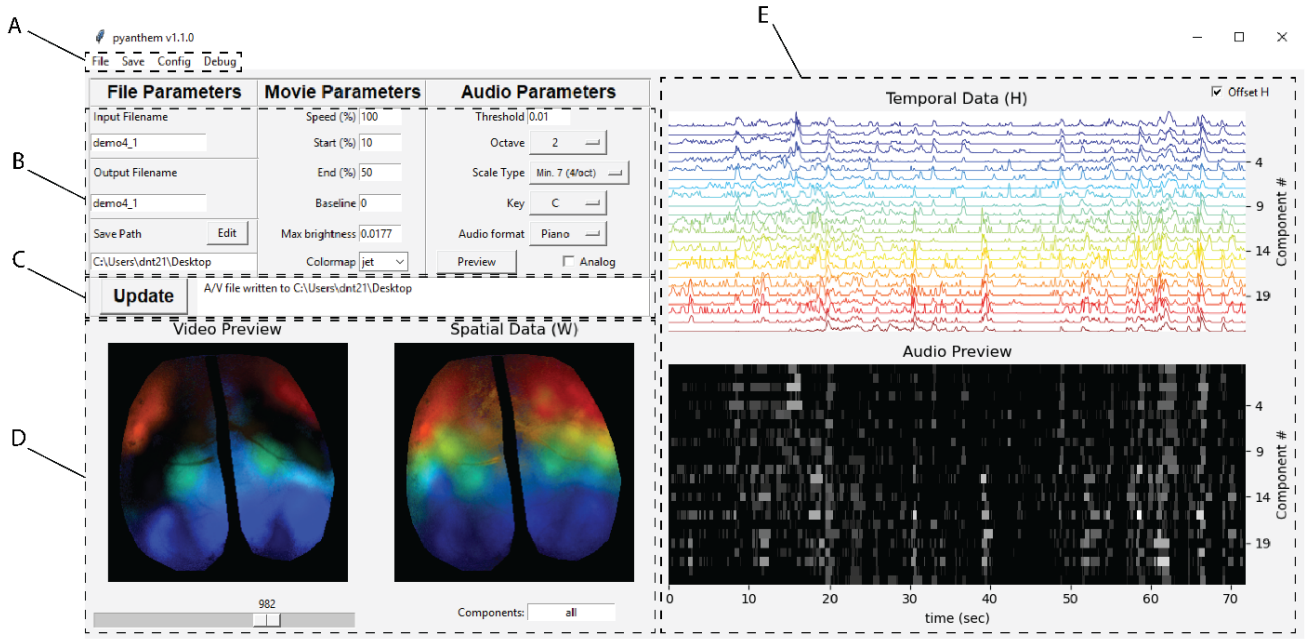

Supplemental Figure 1 - pyanthem Graphical User Interface for creating audiovisualizations. Data is imported in the .mat or .h5 format using the file dialog in Box A, and should contain a temporal variable (n x t) and a spatial variable (s_x x s_y x n). Parameters for the audio and video outputs are adjusted in Box B. Preview updates and GUI status are shown in Box C. A video preview and illustration of the spatial components are shown in Box D. Raw temporal data and an audio preview are shown in Box E. Finally, files can be saved using the Save menu in Box A. Full documentation of pyanthem can be accessed at https://github.com/nicthib/pyanthem

Appendix B: Supplemental Tables

Experiment	Method	Data Sources	Audio conversion technique	Time course selection	Number of components
1	WFOM	Neural (GCaMP6f)	Analog	K-means	18
2	SCAPE	Neural (GCaMP6f)	Digital	K-means	43
3	WFOM	Neural (GCaMP6f), Hemodynamic, Behavior	Analog & Digital	K-means	12

Table 1 - Summary of experimental analysis steps used to create audiovisualizations in Chapter 3.

Variable	States compared	Z score	Rank Sum	p value
Pupil	2 vs 1	-17.36	89142	1.80E-67*
	3 vs 1	-19.57	46860	3.04E-85*
	3 vs 2	-6.19	80269	6.01E-10*
	4 vs 1	-23.24	157634	1.77E-119*
	4 vs 2	-11.33	206461	8.93E-30*
	4 vs 3	-5.20	209859	2.00E-07*
	5 vs 1	-24.45	124314	5.48E-132*
	5 vs 2	-17.58	150703	3.38E-69*
	5 vs 3	-12.58	154906	2.62E-36*
	5 vs 4	-8.94	213705	3.96E-19*
Whisking	2 vs 1	-17.57	88509	3.94E-69*
	3 vs 1	-21.20	42980	9.32E-100*
	3 vs 2	-9.53	72096	1.60E-21*
	4 vs 1	-24.83	151487	4.08E-136*
	4 vs 2	-14.56	193629	4.93E-48*
	4 vs 3	-5.41	209178	6.44E-08*
	5 vs 1	-24.04	125765	1.05E-127*
	5 vs 2	-14.45	162217	2.43E-47*
	5 vs 3	-6.06	174740	1.38E-09*
	5 vs 4	-1.15	251323	**2.50E-01**

Table 2 – Statistical Test results for Neural Dynamic Functional Connectivity model (These results are summarized in Figure 44).

Variable	States compared	Z score	Rank Sum	p value
Pupil	2 vs 1	-4.20	132057	2.68E-05
	3 vs 1	-7.83	81715	4.85E-15
	3 vs 2	-3.10	128165	1.96E-03
	4 vs 1	-12.57	93021	3.01E-36
	4 vs 2	-7.90	138337	2.80E-15
	4 vs 3	-5.10	132762	3.42E-07
	5 vs 1	-13.97	110480	2.23E-44
	5 vs 2	-10.66	153800	1.65E-26
	5 vs 3	-8.33	147318	8.17E-17
	5 vs 4	-3.94	170421	8.31E-05
Whisking	2 vs 1	-5.35	129572	8.75E-08
	3 vs 1	-10.43	77101	1.85E-25
	3 vs 2	-4.41	123995	1.05E-05
	4 vs 1	-14.56	89094	4.79E-48
	4 vs 2	-8.95	134667	3.54E-19
	4 vs 3	-5.09	132802	3.67E-07
	5 vs 1	-15.09	108075	1.85E-51
	5 vs 2	-11.17	151848	5.58E-29
	5 vs 3	-7.79	149039	6.84E-15
	5 vs 4	-3.56	171730	3.70E-04

Table 3 – Statistical Test results for Hemodynamic Dynamic Functional Connectivity model (These results are summarized in Figure 48).

Appendix C: Supplemental Videos

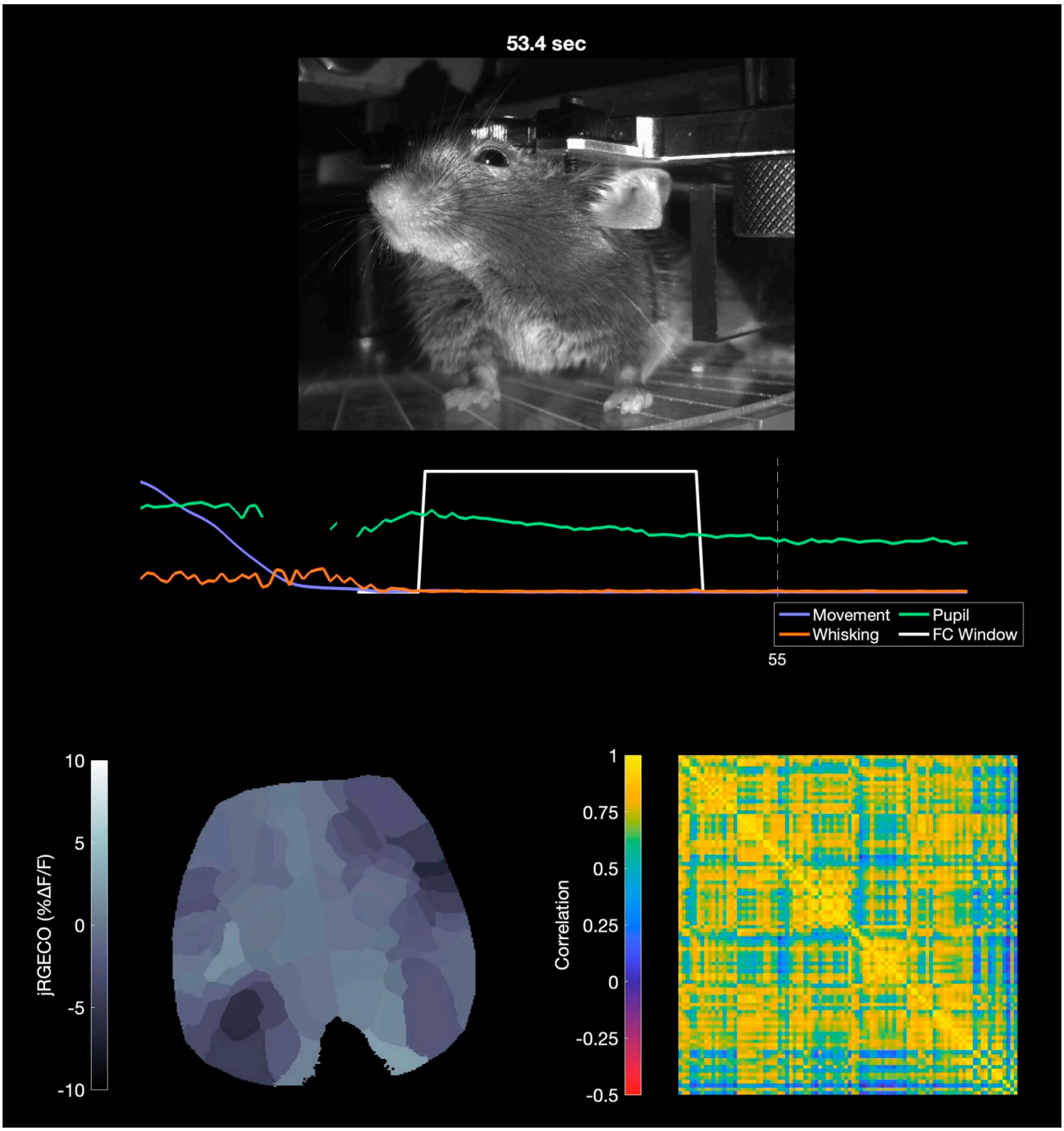

Supplemental Movie 1 – Visualization of sliding window FC along with raw neural data and behavior. (Top) Webcam video of mouse, captured in real time along with WFOM data. (Middle) Behavioral metrics extracted from above video using DeepLabCut (Mathis et al., 2018). Colored lines represent each behavioral metric, while the white line represents the FC window used to calculate FC metrics below. (Bottom) Left shows raw neural activity for each FC cluster projected onto the cortical window of the mouse. Right shows the calculated FC matrix within the window.
Video link: https://ipfs.io/ipfs/QmeUs5Duo2Rqo3RC317ReM3YVQ5n2j7AoXMmsxBAnLwGiR

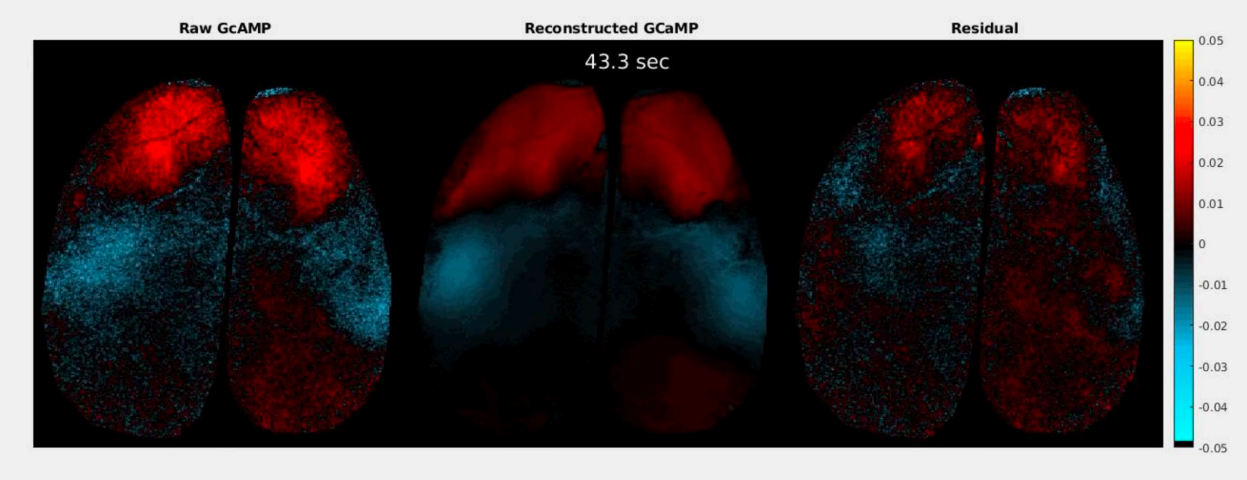

Supplemental Movie 2 – Reconstruction of raw neural activity in Thy1-GCaMP6f mouse using Nonnegative least squares decomposition. Left: Raw GCaMP activity. Middle: Spatiotemporally unmixed linear model, created by multiplying temporal H (obtained by k-means clustering into 18 ROIs) with spatial W (obtained as an output of nonnegative least squares, where H was used as the input). Right: Residual, obtained by subtracting the raw from the reconstruction.
Video link: https://ipfs.io/ipfs/QmbkhMh7YwjXoaCRS6QGUTvyE8YZwFoMZZhZ7RpXmqfyKj

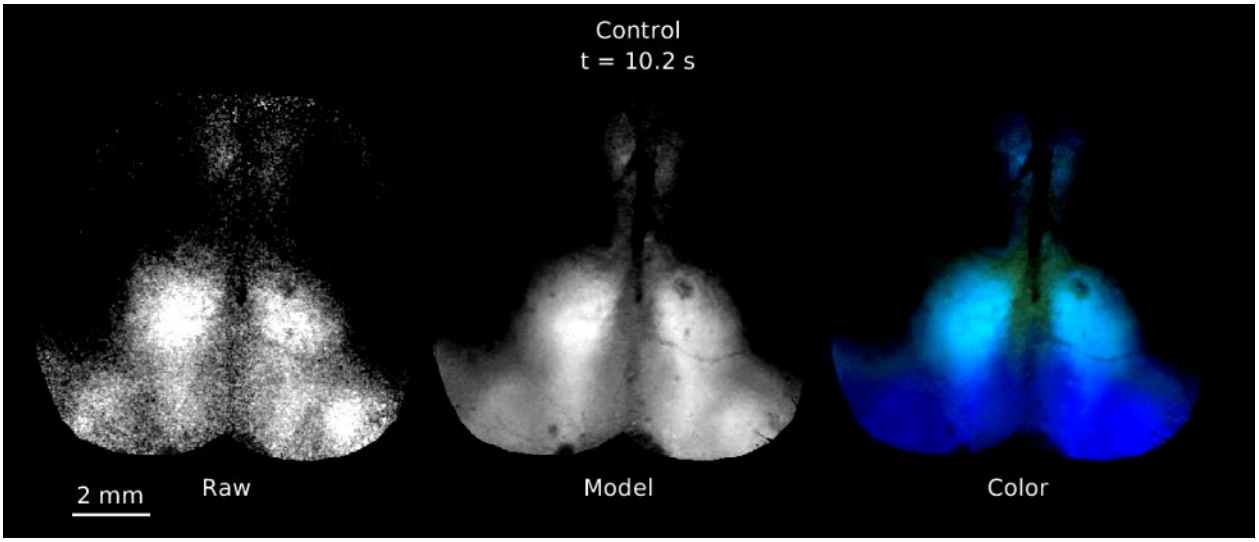

Supplemental Movie 3 - Audiovisualization of Neural activity from the dorsal surface of the thinned skull cortex of the awake mouse. Left: Raw GCaMP activity. Middle: Spatiotemporally unmixed linear model, created by multiplying temporal H (obtained by k-means clustering into 18 ROIs) with spatial W (obtained as an output of nonnegative least squares, where H was used as the input). Right: color remixed reconstructed model data, where each component of W was assigned a unique color from the jet color map, arranged from top (red) to bottom (blue). Movie's soundtrack uses analog (sine-wave) based audio encoding of temporal patterns of each spatial component, ordered in an ascending Cmin7 scale from the back (bottom) to the front (top) of the brain. ***Note: Movie has sound.***
Video link: https://ipfs.io/ipfs/QmS16ajjC8z3jrEorh1SZsbUcR3RzRP1xZYacpcBYGosEr

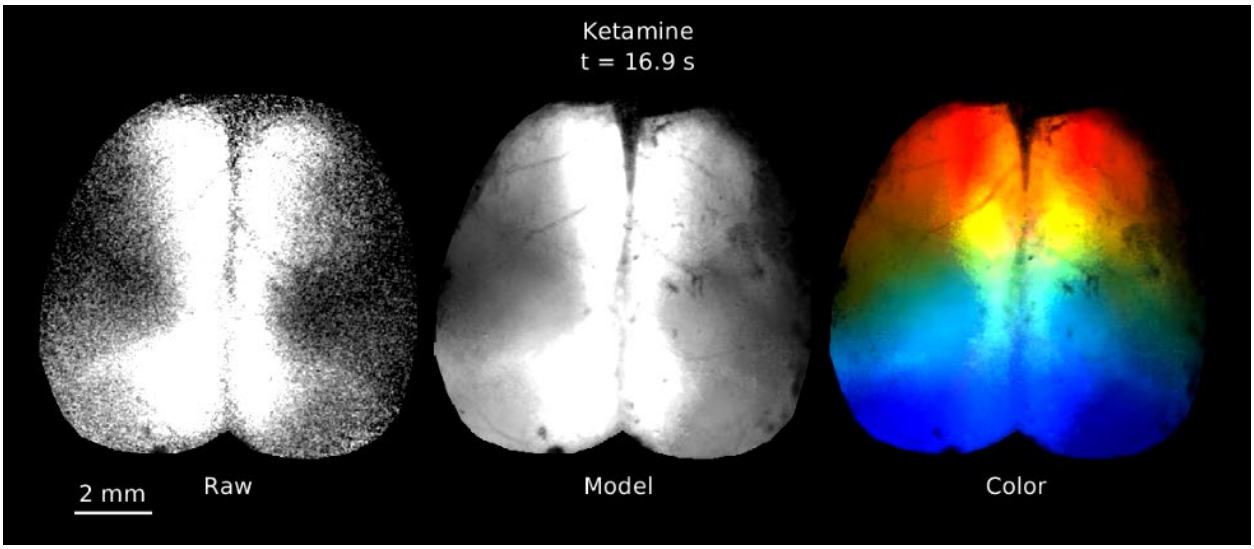

Supplemental Movie 4 - Audiovisualization of Neural activity from the dorsal surface of the thinned skull cortex of the ketamine/xylazine anesthetized mouse. Left: Raw GCaMP activity. Middle: Reconstructed data, created by multiplying temporal H (obtained by k-means clustering into 18 ROIs) with spatial W (obtained as an output of nonnegative least squares, where H was used as the input). Right: color remixed reconstructed model data, where each component of W was assigned a unique color from the jet color map, arranged from top (red) to bottom (blue). Movie's soundtrack uses analog (sine-wave) based audio encoding of temporal patterns of each spatial component, ordered in an ascending Cmin[7] scale from the back (bottom) to the front (top) of the brain. ***Note: Movie has sound.***
Video link: https://ipfs.io/ipfs/QmS35ESiQU3xSzXesfVv4fGiZ8kN628mMA5fHqB7LnyB5A

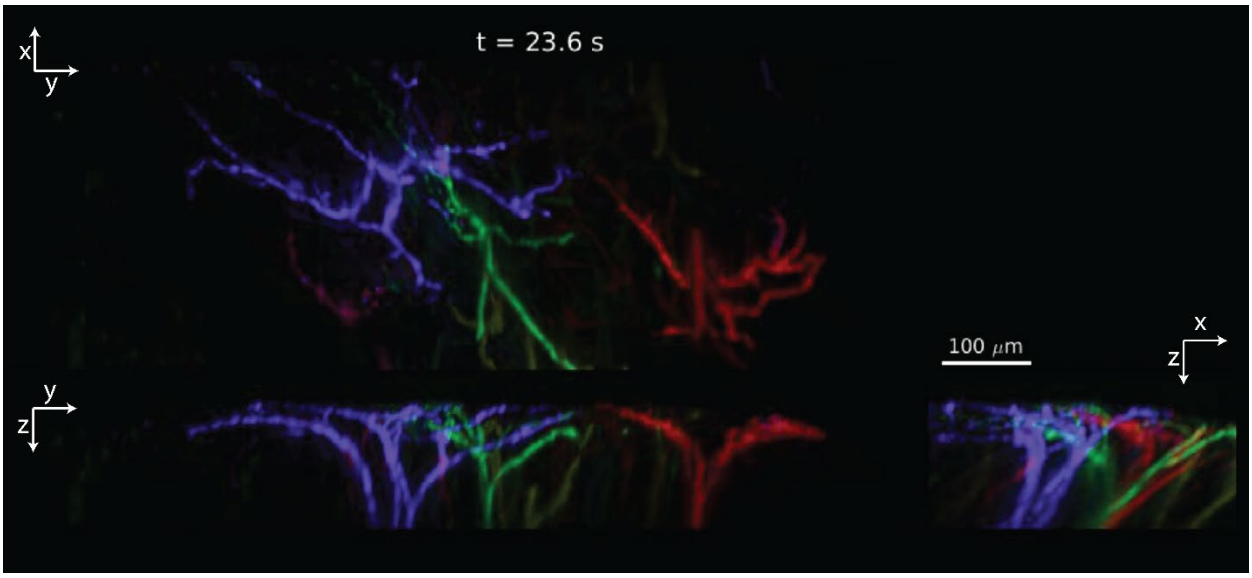

Supplemental Movie 5 - Audiovisualization of SCAPE microscopy data capturing calcium activity in apical dendrites in the awake mouse brain. Panels show top and side maximum intensity projections of color-encoded re-mixed spatial components. Dimensionality reduction was applied to voxels in which at least 5% of values over time exceeded a z-score of 4. Time-course from these voxels were then k-means clustered, and the resulting timecourses were used as an input for nonnegative least squares. 43 output components were color-coded from left to right using an HSV color map. Movie's soundtrack depicts supra-threshold events as piano notes and were chosen on an ascending scale according to order of activity. *Note: Movie has sound.*
Video link: https://ipfs.io/ipfs/QmPpNvrwbsUERjHbjHyCYxVzYVmnCnR7nWQUoWYfb45v6i

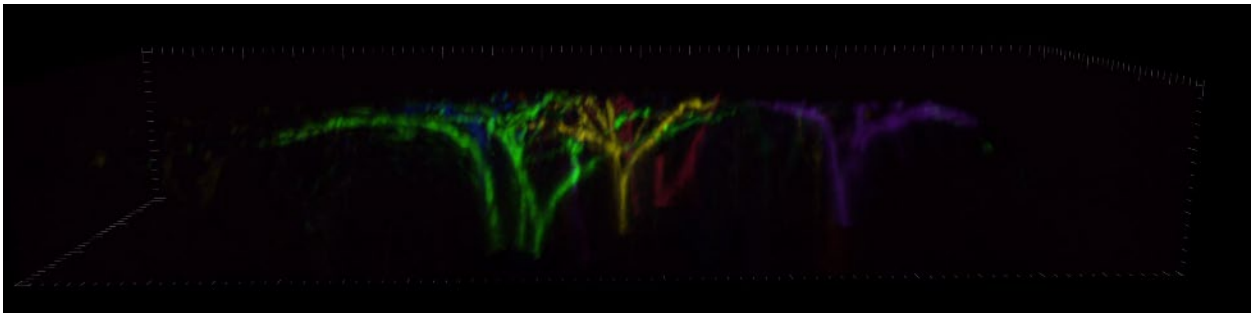

Supplemental Movie 6 - Audiovisualization of 3D reconstructed color mixed GCaMP activity in layer 5 apical dendrites of the awake mouse. This data were obtained using a modified technique from experiment 1, where each voxel's time course was checked for values that exceeded a z-score of 4, and was kept if at least 5% of values exceeded this threshold. The remaining data were then k-means clustered, and the resulting timecourses were used as an input for NNLS. 43 Output components were colored spatially using an HSV color map. Notes were chosen on an ascending scale according to order of activity.
Video link: https://ipfs.io/ipfs/QmSycqBju54AYkKwJsqoaCvtyboJqD3G2evFzeysLcaiaj

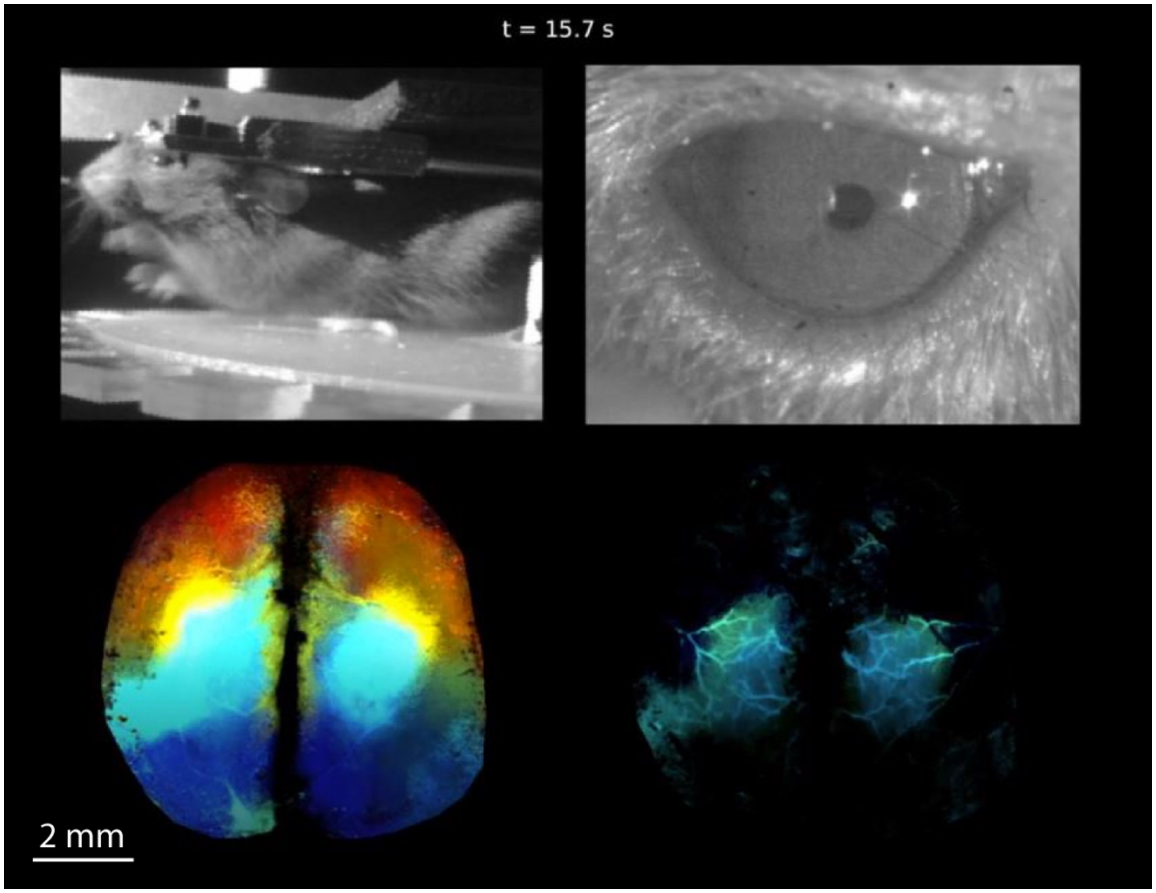

Supplemental Movie 7 - Audiovisualization of neural activity and blood flow from the dorsal surface of the thinned skull cortex of the awake mouse. Behavioral data (top), neuronal activity (GCaMP6f) (bottom left), and cortical hemodynamics (bottom right). Webcam data was acquired simultaneously using two PS3 Eye webcams. Raw GCaMP data was k-means clustered to derive regions of interest (ROIs) from which to extract 12 basis time-courses from both neural and hemodynamic data-streams. Corresponding spatial components fitting a linear model to the original data were derived using non-negative least-squares fitting. Spatial components were then color-coded and re-combined for both datasets, with colors from the Matlab™ jet color map ordered from the front (top, red) to the back (bottom, blue) of the brain. Time-courses for each ROI were converted into audible representations, combined in the movie's soundtrack as piano notes for neural activity and violin as hemodynamics. *Note: Movie has sound*.
Video link: https://ipfs.io/ipfs/QmY6gTtbXRkH6svwNS4uNv1ytLPZNujfq4Zqae7fC21g21

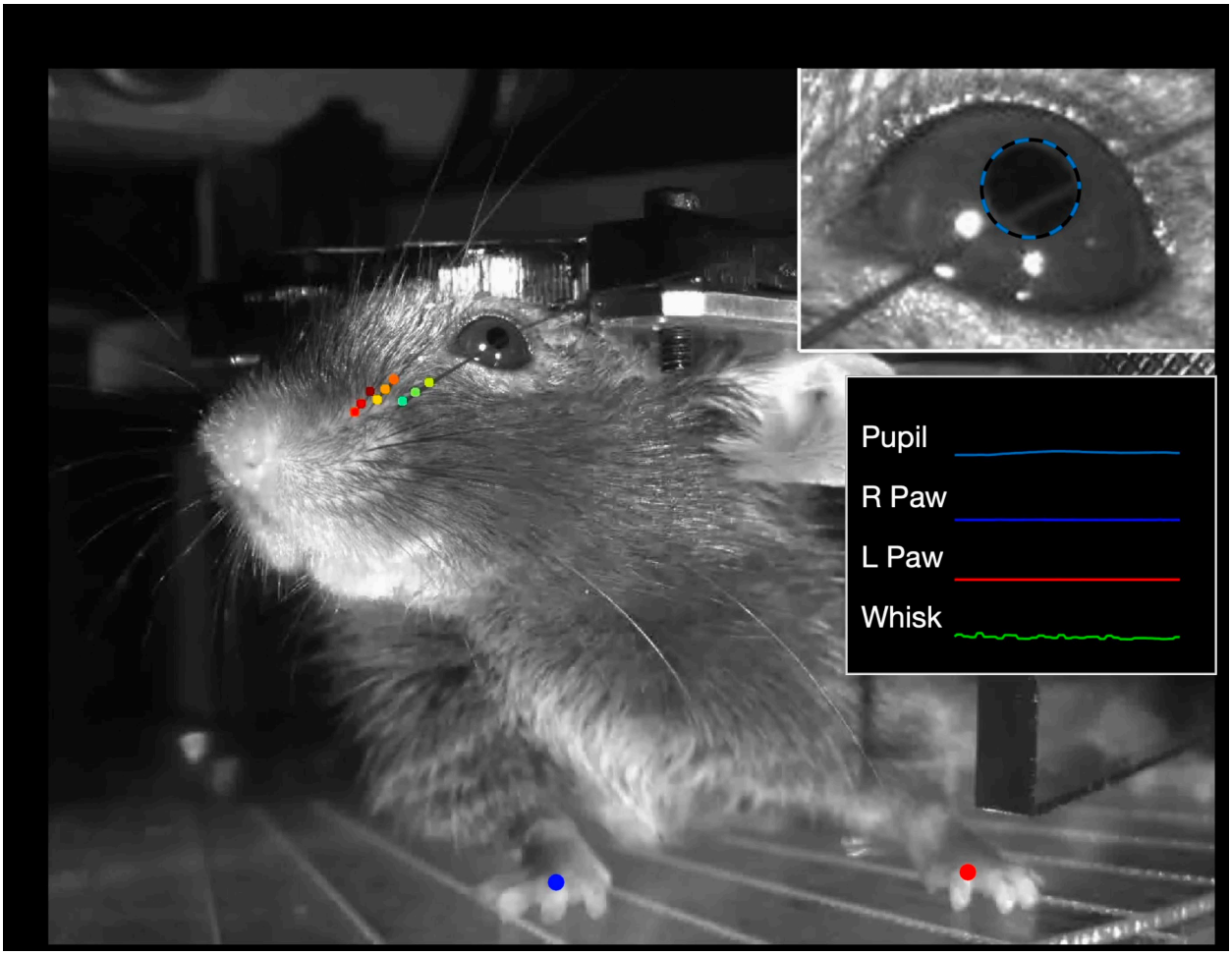

Supplemental Movie 8 – Automated tracking of behavioral movements using DeepLabCut. Colored points indicate individual tracking points on paws and whiskers. The inset top right video shows an estimated ellipse over the pupil, while the line traces indicate the pupil size, paw position, and whisking activity.
Video link: https://ipfs.io/ipfs/QmYU62HQSNcKB616NUSafDuxZdY1a4vH6awCcqYY8nyzuR